DISSERTATION

submitted to the

Combined Faculties for the Natural Sciences and for Mathematics,

Ruperto Carola University of Heidelberg

for the degree of

Doctor of Natural Sciences

put forward by

Dipl.-Phys. Benjamin Titze,

born in Göttingen, Germany

Oral examination on 24 July 2013

Techniques to prevent sample surface charging and reduce beam damage effects for SBEM imaging

Referees: Prof. Dr. Winfried Denk
Prof. Dr. Rasmus Schröder

ABSTRACT

Sample surface charging and electron beam damage are common problems in scanning electron microscopy. In the case of serial block-face electron microscopy (SBEM), sample charging prevents or restricts stack acquisition of non-conducting samples in high vacuum; beam damage imposes a lower limit on the cutting thickness (z-resolution). In this dissertation, I present three approaches that aim to overcome these limitations. To solve the charging problem, I implemented and evaluated two charge elimination techniques for SBEM: surface charge neutralization with an ion gun and automated in-chamber specimen coating with an electron beam evaporator. The ion gun method provides only partial charge neutralization in many cases, although high positive ion current densities are achieved. The automated in-chamber coating method, on the other hand, provides reliable charge elimination in all cases and allows the acquisition of SBEM stacks of non-conducting samples in high vacuum. Thin metallic films provide charge elimination for large sample surfaces and high beam currents, and reduce the signal-to-noise ratio less than the widely-used low-vacuum method. To reduce the effects of beam damage – with the aim of allowing thin cutting at higher electron doses – I have explored imaging and cutting at low temperatures (~100 K) using a closed-loop cooling system and a custom-built cryo-microtome. Further experiments will be necessary to quantify potential improvements of 'Cryo-SBEM' over room-temperature SBEM operation.

KURZFASSUNG

Aufladung von Probenoberflächen und elektronenstrahlinduzierte Probenschäden sind verbreitete Probleme in der Rasterelektronenmikroskopie. Im Falle der seriellen Block-oberflächen-Elektronenmikroskopie (engl. *Serial Block-Face Electron Microscopy*, SBEM) verhindert Oberflächenaufladung die Aufnahme von 3D-Datensätzen nichtleitender Proben im Hochvakuum oder führt zu Einschränkungen der Bildqualität. Strahlenschäden setzen eine untere Grenze für die erreichbare Schnittdicke (z-Auflösung). In dieser Dissertation stelle ich drei Ansätze vor, die zum Ziel haben, diese Einschränkungen zu überwinden. Zur Lösung des Aufladungsproblems habe ich zwei Entladungstechniken für SBEM implementiert und evaluiert: Ladungsneutralisation mit einer Ionenkanone und automatisierte Probenbeschichtung in der SBEM-Vakuumkammer mit einem Elektronenstrahlverdampfer. Durch Einsatz der Ionenkanone wird in vielen Fällen nur eine teilweise Entladung erzielt, obwohl hohe positive Ionenstromdichten erreicht werden. Die automatisierte Beschichtungsmethode hingegen erzielt zuverlässige Entladung in allen Fällen und ermöglicht die Aufnahme von SBEM-Datensätzen nichtleitender Proben im Hochvakuum. Dünne Metallfilme bewirken eine vollständige Entladung großer Probenoberflächen bei hohen Strahlströmen und reduzieren das Signal-zu-Rausch-Verhältnis weniger stark als die weit verbreitete Niedrigvakuum-Methode. Um durch Strahlenschäden hervorgerufene Effekte zu reduzieren – mit dem Ziel, dünnes Schneiden bei höheren Elektronendosen zu ermöglichen – habe ich Bildgebung und Schneiden bei tiefen Temperaturen (~100 K) untersucht. Hierzu wurden ein geschlossener Kühlkreislauf und ein spezialangefertigtes Cryo-Mikrotom verwendet. Weitere Experimente sind nötig, um mögliche Verbesserungen von „Cryo-SBEM" gegenüber SBEM-Nutzung bei Raumtemperatur zu quantifizieren.

Contents

1 Introduction 11

1.1 Overview 13

1.2 Serial block-face electron microscopy 13

1.2.1 Sample charging 15

1.2.2 Beam damage 16

1.3 Sample surface charging and methods to prevent it 17

1.3.1 Sample resistivity and charge balance 20

1.3.2 Low-vacuum method 21

1.3.3 Charge neutralization with an ion gun 22

1.3.4 Conductive coating 23

1.4 Cutting with a diamond knife 24

1.4.1 Parameters affecting cutting 24

1.4.2 Beam damage and the effect of low temperatures 25

2 Charge neutralization with an ion gun 29

2.1 Prior work 30

2.2 Improved setup 32

2.2.1 New microwave generator 33

2.2.2 Anode grid and extractor grid 34

2.2.3 Improved ion optics 35

2.3 Aiming and operating the ion gun 38

2.4 Results 41

2.4.1 Ion current densities 41

2.4.2 Noise from the ion gun 43

2.4.3 Charge neutralization 44

2.5 Discussion 47

2.5.1 Ion energy distribution and positive surface charging 49

2.5.2 Ballistic ion trajectories 50

3 Automated in-chamber specimen coating 53

3.1 Setup 53
3.1.1 In-chamber coating system 53
3.1.2 Control of the coating process 57
3.1.3 Samples and sample holder 59

3.2 Results 60
3.2.1 SNR degradation in low vacuum 60
3.2.2 Initial coating experiments with carbon 61
3.2.3 Chromium, palladium and other coating materials 62
3.2.4 In-chamber coating 64
3.2.5 Effect of coating on SNR 66
3.2.6 Beam deceleration 69
3.2.7 Coating during SBEM stack acquisition 70
3.2.8 Debris and other issues 72

3.3 New evaporator head 74
3.3.1 Simulations and new design 74
3.3.2 Preliminary results 77

3.4 Summary and discussion 78

4 Cryo-SBEM 81

4.1 Effects of beam damage on imaging and cutting 81
4.1.1 Observation of beam damage effects in SEM images 82
4.1.2 Electron-dose limits for consistent SBEM cutting 83

4.2 Cryo-SBEM setup 85
4.2.1 Closed-cycle cooling system 85
4.2.2 Modifications for low-temperature SBEM operation 86

4.3 Results 88
4.3.1 Temperature measurements 88
4.3.2 Low-temperature effects 89
4.3.3 Cutting and imaging at low temperature 91

4.4 Discussion and next steps 93

5 Conclusions and Outlook 95

Appendix A: SNR estimation 99

Appendix B: Biological samples 101

Appendix C: List of acronyms/abbreviations 103

References 105

Acknowledgments 111

The work presented in this dissertation was carried out in the Department of Biomedical Optics at the Max Planck Institute for Medical Research, Heidelberg, Germany, under the supervision of Prof. Dr. Winfried Denk.

I performed all experiments myself, except when noted otherwise, and prepared this dissertation myself. All resources used are specified.

Parts of this dissertation have been published in:

TITZE, B. & DENK, W. (2013). Automated in-chamber specimen coating for serial block-face electron microscopy. *Journal of Microscopy* **250**, 101–110.

Chapters 1 and 3 contain figures and text from this publication.

1 Introduction

When asked to find out how a complicated device works, most people would intuitively proceed to take it apart and have a look at its inner workings. They would try to make sense of how its different parts are connected to each other, hoping to understand how its behavior can be explained. This approach rests on the assumption that function can be inferred from structure, thereby allowing a mechanistic understanding of the device.

A neuroscientist who wishes to follow the same approach is faced with an intimidating endeavor. An average human brain, for example, consists of 80–90 billion neurons (Azevedo et al., 2009) and many trillions of synapses that form connections between those neurons. How can such a complicated object be 'taken apart'; how can its structure be extracted and its function fully understood? Even when looking at only a tiny fraction of a brain – using a light microscope or an electron microscope – the immense difficulties quickly become apparent.

The Spanish neuroanatomist Santiago Ramón y Cajal (1852–1934) was one of the early researchers who investigated the fine details of neural tissue. He used a technique developed by his Italian colleague Camillo Golgi (1843–1926) to sparsely stain neurons to make them visible under a light microscope. Ramón y Cajal was well aware of the daunting task that lay ahead when he wrote in his autobiography that "the supreme cunning of the structure of the gray matter is so intricate that it defies and will continue to defy for many centuries the obstinate curiosity of investigators." (*Recollections of my life*, MIT Press, 1989). The observation that a large number of relatively simple subunits can give rise to complex behavior, intelligence and consciousness is a source of great fascination for many – and perhaps the most important driving force for neuroscience research.

Since Ramón y Cajal's and Golgi's pioneering work on the structure of the nervous system in the late 19th and early 20th century, new and improved staining methods ("the gain in brain is mainly in the stain") and new imaging techniques have allowed researchers to look at brains in much more depth and detail, allowing them to classify different types of neurons, map connections between them, and decipher simple neural circuits.

The invention of the electron microscope in the first half of the 20th century (transmission electron microscope, TEM: Knoll & Ruska, 1932; scanning electron microscope, SEM: Ardenne, 1938) was a major technological breakthrough. Using electrons instead of photons, scientists could image neural tissue at a much higher resolution than before, which opened up new possibilities to map neural circuitry.

In 1972, a team led by Sydney Brenner and John White at the MRC Laboratory of Molecular Biology in Cambridge, England, used transmission electron microscopy to map the complete neural circuitry ('connectome') of the nematode *C. elegans*. The researchers fixed, stained, and embedded the worm, cut it into thousands of sections, imaged each of them, and manually followed the neural processes of all 302 neurons to obtain the worm's full neural wiring diagram. The results were published in 1986, after 14 years of data acquisition and analysis (White et al., 1986).

The past decade has brought important new developments for neural circuit reconstruction. While the attainable resolution has not improved much for electron microscopy of neural tissue, there has been a technological push towards full automation to allow the acquisition of image stacks from large sample volumes. One of the new imaging techniques is serial block-face electron microscopy (SBEM; Denk & Horstmann, 2004), which is the central theme of this dissertation. Other new techniques are FIB-SEM (Heymann et al., 2006; Knott et al., 2008; FIB: focused ion beam) and ATUM-based SEM (Hayworth et al., 2006; ATUM: Automated Tape-collecting Ultramicrotome).

The benefits of automated data acquisition, the availability of faster microscopes (e.g. multibeam SEMs; see Schalek et al., 2012) and new staining methods for whole brains (Mikula et al., 2012) will allow neuroscientists to acquire increasingly large volumetric high-resolution datasets. Reconstructing the circuit diagrams from the data is difficult and time-consuming. Since manual reconstruction ('tracing') of neural circuitry is very slow (contouring: 300 h per mm neurite length;

skeletonization: 6 h per mm; Helmstaedter et al., 2011), automated segmentation and synapse detection will be essential to tackle dense reconstructions of large volumes. Several recent reviews discuss the various obstacles for data acquisition and analysis that need to be overcome (Lichtman & Denk, 2011; Denk et al., 2012; Briggman & Bock, 2012; Helmstaedter & Mitra, 2012).

1.1 Overview

This dissertation focuses on how data acquisition with a serial block-face scanning electron microscope (SBEM; Denk & Horstmann, 2004; Leighton, 1981) could be improved. I have looked at two physical processes that occur during imaging with a scanning electron microscope: sample charging and beam damage. These (unwanted) phenomena impose constraints on signal-to-noise ratio (SNR) and cutting thickness for SBEM acquisition (see sections 1.2.1 and 1.2.2). During my doctoral research, I have pursued several experimental approaches to overcome these limitations.

In this introductory chapter, I will provide (1) a brief introduction to SBEM and the limitations imposed by sample charging and beam damage, (2) an overview about the basics of sample charging and short introductions to different methods to prevent it, and (3) an introduction to cutting with a diamond knife, the influence of beam damage on cutting, and the reason why cooling the sample to cryogenic temperatures may yield improvements.

In the following chapters, I will present the three projects that I have been working on: Charge neutralization with an ion gun (Chapter 2), Automated in-chamber specimen coating (Chapter 3), and Cryo-SBEM (Chapter 4). In the final chapter, I will summarize all results and discuss directions for future work.

1.2 Serial block-face electron microscopy

Serial block-face electron microscopy (SBEM) allows high-resolution volumetric imaging of neural tissue, which is the starting point for mapping neural circuits. After early attempts by Leighton (1981), who constructed a microtome for cutting inside the chamber of a scanning electron microscope, Denk & Horstmann (2004)

achieved full automation and demonstrated the first automatic stack acquisitions of neural tissue. The first published use of SBEM for a large-scale reconstruction project was the mapping of direction-selective circuitry in the retina (Briggman et al., 2011).

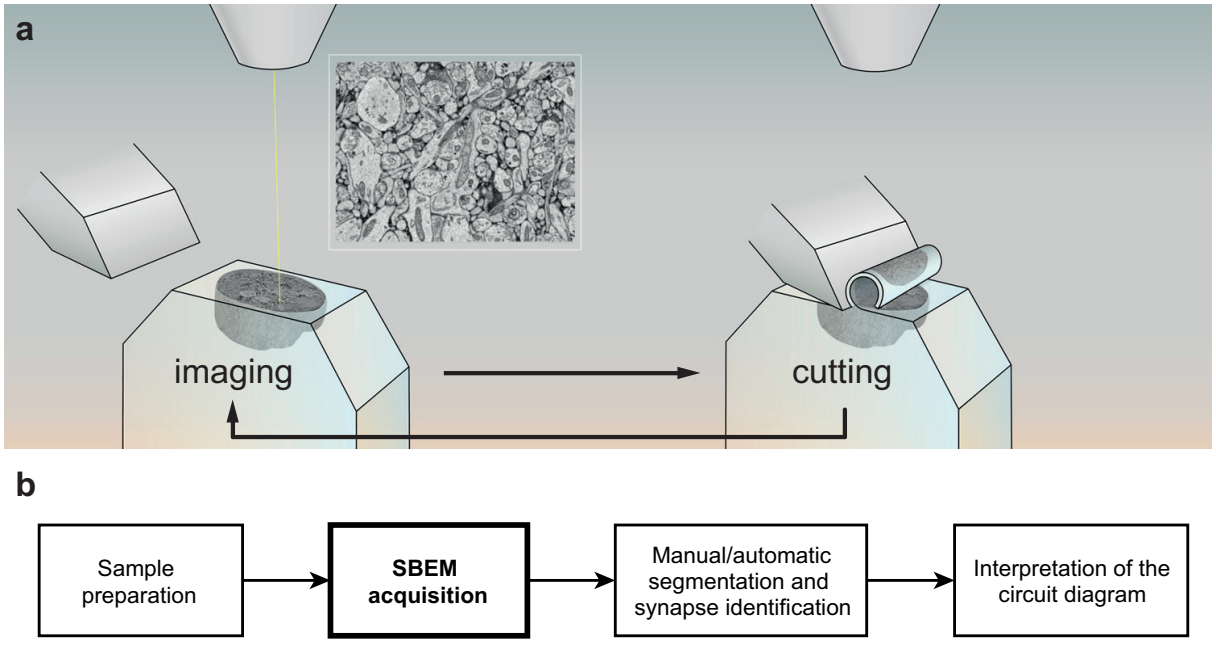

Fig. 1.1: Serial block-face electron microscopy (SBEM). (a) Left: The fresh sample surface is imaged with the SEM. Right: The diamond knife cuts off a thin section, revealing a fresh surface. The vertical knife position is fixed. Before each cut, the sample is moved up by a distance equal to the cutting thickness (= z-resolution). The two steps illustrated can be repeated thousands of times. Artwork by Julia Kuhl. (b) SBEM workflow (explained in the main text).

For SBEM acquisition, the specimen to be imaged is stained en bloc with heavy-metal atoms (yielding a significant contrast enhancement) and embedded in epoxy resin for mechanical stability. A diamond-knife microtome mounted onto the inner side of an SEM door enables automatic cutting inside the vacuum chamber. Each time a thin section is cut off the block, the freshly cut sample surface is imaged with the SEM. The cycle of cutting and imaging is repeated until the desired volume is imaged (Fig. 1.1). The acquisition speed is measured in voxels/s. Using large beam currents (>5 nA), rates of about 10 million voxels/s are currently possible. At such a rate, the acquisition of a cubic millimeter of neural tissue at 25-nm isotropic resolution (6.4×10^{13} voxels) would require 74 days of pure imaging time.

SBEM stacks are used to reconstruct the neural circuits contained in the imaged volumes by following the individual cell bodies, dendrites and axons, and by identifying synapses. This can be done by manually tracing all neural processes, section by section. However, large datasets would take a prohibitively long time to be reconstructed this way. For instance, it would take more than 10,000 person years to complete a manual reconstruction of a single cortical column of a mouse brain (Briggman & Denk, 2006). Therefore, automatic reconstruction will be crucial for large SBEM volumes. Devising algorithms that can solve this task is the foremost challenge – and currently a bottleneck – for the emerging field of 'connectomics'.

There are two types of SBEM. Fresh sample surfaces can be revealed either by a diamond knife that cuts off the imaged surface (diamond-knife SBEM, as described above; abbreviation DiK-SBEM), or by milling with a focused ion beam (Heymann et al., 2006; Knott et al., 2008; Bushby et al., 2011; abbreviated FIB-SBEM or FIB-SEM). This dissertation only deals with diamond-knife SBEM (see section 1.4).

In the following two sections, I will discuss the impact of sample charging and beam damage on SBEM imaging. Of course, both charging and beam damage also occur in classical 'single-image' SEM. In this dissertation, I look at them in the context of SBEM, but most of the results are applicable to SEM as well.

1.2.1 Sample charging

Charging is a constraint for SBEM for two reasons. First, if a non-conducting sample charges up too much, imaging may not be possible at all in high vacuum, or only by accepting image defects. Second, if the low-vacuum method is used to neutralize the surface charge, the SNR is reduced (see section 1.3.2). Ideally, a sample is prepared in a way that intrinsically prevents charging. In cases where this is not possible, the only method available so far to eliminate charging for SBEM imaging has been the low-vacuum method. Section 1.3 provides an overview of charging and of different charge-elimination methods, including the two methods that I have implemented and evaluated for SBEM.

If there is an established method – the low-vacuum method – for charge elimination, why explore alternatives? The reason is that the reduction in SNR caused by the low-vacuum method increases the total acquisition time of a SBEM stack if a certain minimum SNR is maintained. For the acquisition of volumes with very large sample

surface areas (for example, a whole mouse brain), most of the required acquisition time is taken up by imaging, whereas the cutting process only takes about a minute or less for each section. The limiting factor is, therefore, the pixel acquisition rate, which is determined by the dwell time of the electron beam. A shorter dwell time increases acquisition speed, but also reduces signal-to-noise ratio, because fewer electrons are available per pixel.

The goal of the research presented in this dissertation is to allow faster data acquisition rates while maintaining a signal-to-noise ratio that is sufficiently high for data analysis. If a charge elimination method is found that reduces SNR less than the low-vacuum method or not at all, the surplus SNR can be 'spent' by increasing acquisition speed. For very large acquisition projects, improvements in SNR will save many weeks or even months of imaging time.

1.2.2 Beam damage

Another physical phenomenon – beam damage – plays an important role for thin cutting with a diamond knife. Electron-beam-induced damage to the sample negatively affects cutting and thereby limits the z-resolution of SBEM stacks (Helmstaedter et al., 2008; see section 4.1.2).

While the x-y-resolution of SBEM imaging can be very high (several nm), z-resolution in diamond-knife SBEM has been limited to about 25 nm until recently. A lower cutting thickness at an adequate signal-to-noise ratio would further improve z-resolution of SBEM datasets. This would facilitate human and automatic circuit reconstruction, and may even be indispensable to follow very fine neural processes.

Cutting below 25 nm and even below 10 nm appears to be possible, but the electron dose must be significantly reduced to enable consistent cutting (Mancuso, 2012; Sarah Mikula, personal communication), which supports the assumption that beam damage plays a crucial role in imposing limits on minimum cutting thickness. Even at a cutting thickness of 25 nm or larger, if the electron dose is too high, consistent cutting cannot be achieved (see section 4.1.2).

In section 1.4, I will provide a brief introduction to cutting with a diamond knife and explain the motivation for exploring low-temperature imaging and cutting to overcome electron-dose restrictions.

1.3 Sample surface charging and methods to prevent it

The point at which the electron beam impinges upon the sample surface in a scanning electron microscope can be compared to a junction in an electrical circuit (Fig. 1.2). In case of a grounded conducting sample, the following equation holds:

$$I_{\mathrm{P}} = I_{\mathrm{BSE}} + I_{\mathrm{SE}} + I_{\mathrm{GND}}$$

(I_{P}: primary beam current; I_{BSE}: current of backscattered electrons; I_{SE}: current of secondary electrons; I_{GND}: current flowing through the sample to ground)

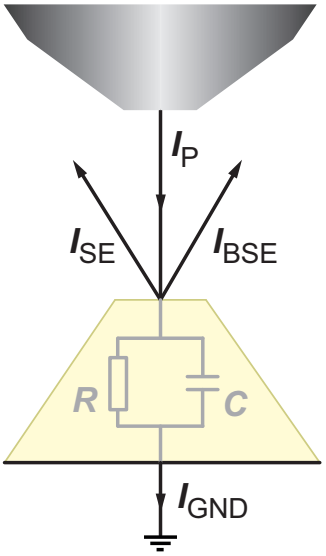

Fig. 1.2: Electron beam impact point as a junction in an electrical circuit. R: bulk resistance of the sample; C: bulk capacitance. Currents are explained in the text on the left.

In case of a grounded but badly conducting sample, where I_{GND} is not large enough to balance the right side with the left side of the equation above, conservation of charge dictates that:

$$\dot{Q} = \dot{Q}_{\mathrm{surface}} + \dot{Q}_{\mathrm{buried}} = I_{\mathrm{P}} - I_{\mathrm{BSE}} - I_{\mathrm{SE}} - I_{\mathrm{GND}}$$

Charge will accumulate on the sample surface (Q_{surface}) and below the surface (Q_{buried}) while the primary beam is scanning the sample. Charge can be 'buried' below the surface, since the beam electrons penetrate deeply into the sample (Kanaya & Okayama, 1972). The charge accumulating on the surface of the sample will yield a surface potential $V_{\mathrm{surface}}(x, y)$ across the imaged region that – if strong enough – negatively affects imaging (see Fig. 1.3 and text below).

If the electron beam continues to be raster-scanned over the sample surface, all currents will reach a steady state at which the accumulation of charge will stop. At this point, in the limit of fast scanning, a stable (but non-uniform, in the general case) surface potential has developed, whose average value can be estimated if the bulk resistance R and I_{GND} are known:

$$\bar{V}_{\mathrm{surface}} = R I_{\mathrm{GND}}$$

If the ground connection is broken (very high resistance to ground), charge accumulation will continue until the surface potential reaches values as high as the

electron beam acceleration potential of the microscope's cathode, which will cause the beam to be reflected.

When scanning has stopped, a non-zero surface potential will decay again because the charge is drained to ground (provided an adequate ground connection exists). The sample's bulk resistance R and its bulk capacitance C together form a simple RC circuit. Using a plate capacitor as a model for a cuboid-shaped sample ($C = \varepsilon_r \varepsilon_0 A/d$; A: sample area; d: sample depth), the time constant for this process is given by:

$$\tau = RC = \rho \frac{d}{A} \varepsilon_r \varepsilon_0 \frac{A}{d} = \rho \varepsilon_r \varepsilon_0$$

For epoxy resin (resistivity of $\rho = 10^{13}$–10^{14} Ωm, $\varepsilon_r = 3.7$; Stöcker, 2000), which is used to embed biological samples for SBEM imaging, this yields a time constant of between about five minutes and one hour.

For the projects presented in this dissertation, I used epoxy-embedded heavy-metal-stained neural tissue, for which the net charge introduced into the sample for the landing energies used for SBEM imaging (1.5–3 keV) is *negative*. The negative charge accumulates locally, as described above, resulting in electric fields inside and outside the sample (Cazaux, 1986).

The outside fields, caused by the surface potential V_{surface} (see above), decelerate the incident electrons, thereby reduce their landing energy, and – because charge accumulation is spatially non-uniform – distort the image and decrease resolution. Secondary and backscattered electrons are accelerated, which changes signal amplitudes, again, in a spatially non-uniform way (Shaffner & Van Veld, 1971; Pawley, 1972). The increase in detector signal caused by acceleration of signal electrons leads to a darkening (black in the case of detector saturation; detector signal is displayed inverted) in the parts of the image that show charged-up areas on the sample surface. This type of artifact was often observed in the case of the samples used for this dissertation (for a detailed discussion, see Fantana, 2006, Chapter 4).

Because of their low kinetic energy (<50 eV), secondary electrons (SE) are much more affected by charging than backscattered electrons (BSE). This can make SE imaging virtually impossible in the presence of even small amounts of charging (see, for example, Goldstein et al., 2003, Chapter 15). A more in-depth discussion of the complex dynamics of charging on the sample surface and below can be found in Cazaux (2004).

Examples of strong charging artifacts (detector saturation, changes in signal intensity, and distortions) in BSE and SE images of non-conducting samples are shown in Fig. 1.3. Note that in this dissertation, the term "non-conducting sample" is loosely used to refer to all samples that show charging artifacts when imaged in the SEM.

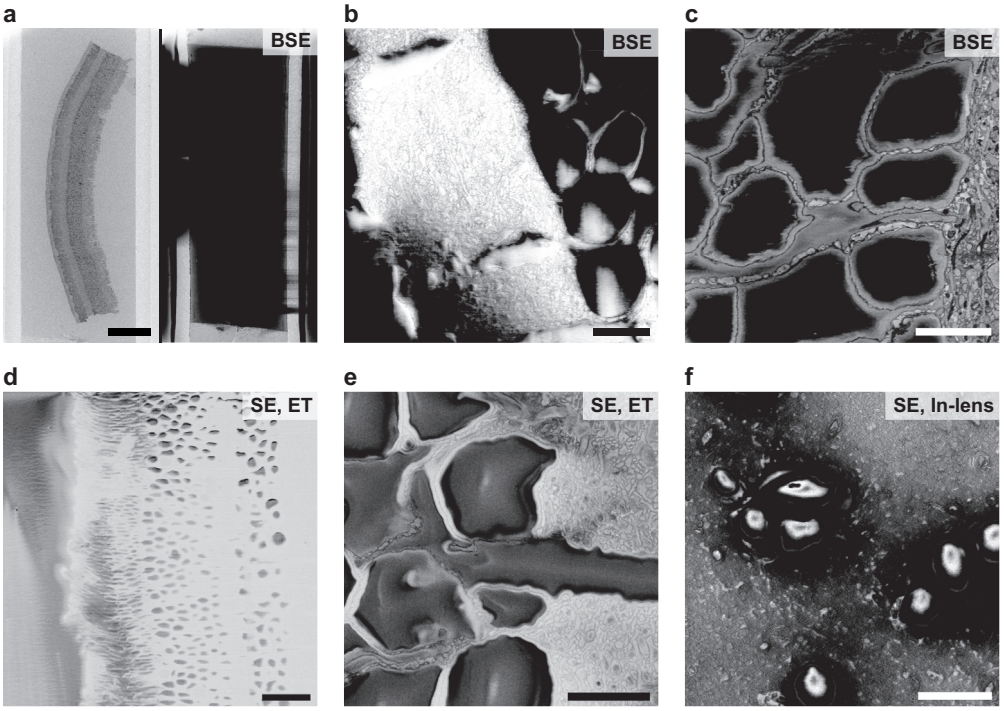

Fig. 1.3: Examples of severe sample charging. Maximum signal is black. (a) Left: Badly-grounded epoxy-embedded rabbit retina sample imaged in low vacuum. Right: When switching to high vacuum, the sample charges up and the detector signal saturates. Scale bar: 100 μm. (b) Same sample, imaged at higher magnification. Charging causes strong distortions. Scale bar: 5 μm. (c) A well-grounded non-conducting retina sample (sides coated with gold). Scale bar: 5 μm. (d) Retina sample, overview image with an Everhart-Thornley (ET) detector. Scare bar: 25 μm. (e) Retina sample at higher magnification. Scare bar: 5 μm. (f) Zebra finch sample, imaged with the in-lens detector of a ZEISS Ultraplus. Scale bar: 10 μm.

In the following sections, I will present several approaches to prevent sample surface charging, all of which were suggested (but not implemented) by Leighton (1981) for his early non-automated SBEM prototype.

1.3.1 Sample resistivity and charge balance

The most obvious approach to prevent charging from the start – or at least reduce it to a minimum – is to increase the conductivity of the sample during its preparation. This can be achieved by increasing the concentration of heavy metals in the sample (Seligman et al., 1966; Malick et al., 1975; Deerinck et al., 2010).

Since the heavy-metal atoms serve as contrast agents, their distribution is necessarily non-uniform and, in particular when only selected structures such as cell surfaces are stained (Briggman et al., 2011), the lower concentration of heavy metal in the regions in between (for example the interiors of somata) no longer provides sufficient conductivity to drain the charge.

For certain landing energies of the primary electron beam, the combined BSE and SE yields ($\eta + \delta$) sum to unity, resulting in a zero rate of net charge introduction to the sample (Joy, 1989; Joy & Joy, 1996):

$$\dot{Q} = I_{\mathrm{P}} - (\eta + \delta) I_{\mathrm{P}} = I_{\mathrm{P}} - (I_{\mathrm{BSE}} + I_{\mathrm{SE}}) = 0$$

Two 'cross-over points' can be observed: When the landing energy is lowered from a high value, the upper cross-over point is reached (at which net charge introduction becomes zero). Lowering the beam energy further results in $\eta + \delta$ increasing above unity, so that net charge introduction becomes positive (more electrons leaving the sample than are supplied by the primary beam) for a certain range of landing energies, until the lower cross-over point is reached (Goldstein et al., 2003, Chapter 3).

The landing energy at which a charge balance is achieved is strongly material-dependent (Reimer, 1998, Chapter 4), which can make this method difficult or impossible to use to eliminate charging in case of heterogeneous samples, such as resin-embedded heavy-metal-stained biological tissue.

1.3.2 Low-vacuum method

If sample conductivity is not sufficient to prevent charging, and imaging at the charge-balance point not possible or not practical, the low-vacuum method can be used to eliminate charging effects (Robinson, 1975; Moncrieff et al., 1978). Positive ions generated as the electron beam passes through a low concentration of gas in the chamber (e.g. water vapor, nitrogen or hydrogen) neutralize the surface charge (Fig. 1.4).

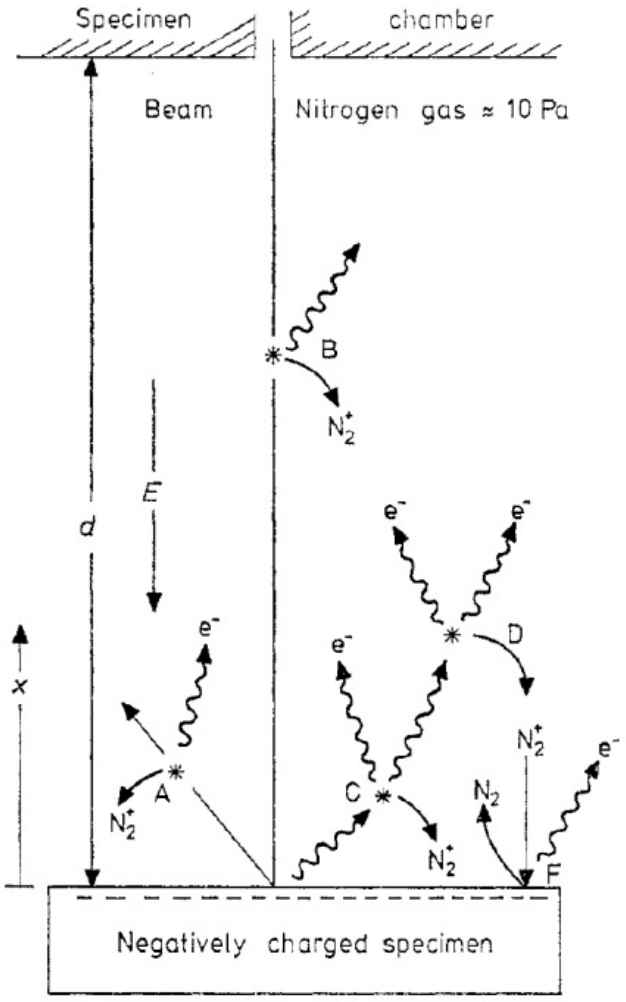

Fig. 1.4: Low-vacuum method. Gas molecules are ionized by beam and signal electrons. The resulting positive ions neutralize the surface charge. A: ionization by backscattered electrons; B: ionization by beam electrons; C: ionization by secondary electrons; D: multiplication of charge by the electric field; F: ion impact releasing low-energy electrons and discharging the surface. Figure from Moncrieff et al., 1978.

Low-vacuum imaging is compatible with a wide range of electron energies and with virtually all types of non-conducting specimens. Its main disadvantage is the reduction of contrast and resolution due to scattering of both primary and signal electrons by the gas molecules (Moncrieff et al., 1979; Mathieu, 1999; Thiel & Toth, 2005), see Fig. 1.5.

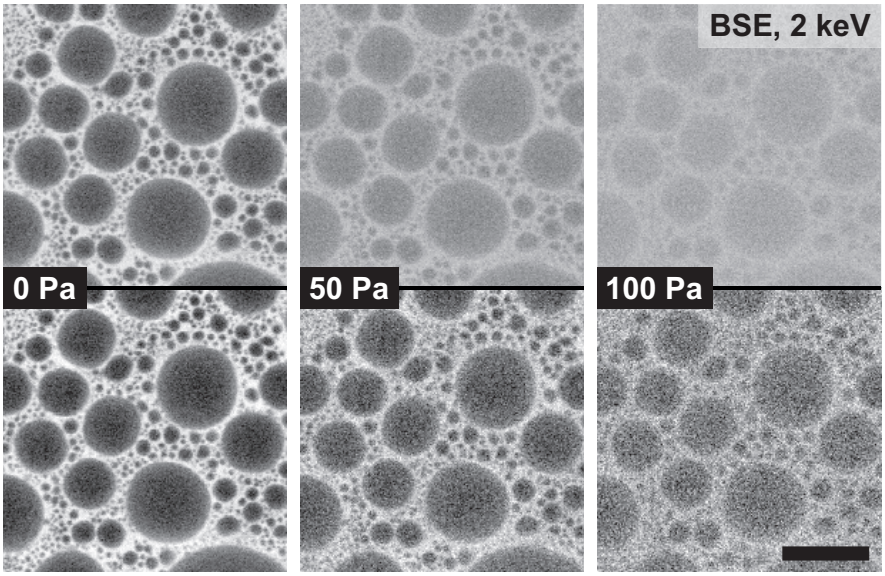

Fig. 1.5: The effect of low-vacuum operation on the signal-to-noise ratio. Images of a conducting sample (tin-on-carbon test sample, Agar Scientific, Essex, UK), taken at different pressures (0, 50 and 100 Pa) of water vapor, 2 keV landing energy, ~80 pA beam current, 5 mm working distance, and 2 μs dwell time. Bottom row: same images after histogram normalization. Scale bar is 1 μm.

1.3.3 Charge neutralization with an ion gun

Instead of using the electron beam itself to generate ions through scattering with gas molecules, the positive ions can be generated inside an ion gun and then be directed onto the sample surface. This approach, pioneered by Crawford (1979), never gained traction, presumably because it was introduced at about the same time as the low-vacuum method, which was much easier to implement. If routine use of charge neutralization with an ion gun were possible, it would be a very attractive method, since it should ideally not reduce image SNR at all.

For my diploma thesis, I began to work on this approach to make it applicable to SBEM. During my doctoral research, I substantially improved the ion gun setup and carried out further charge neutralization experiments. In Chapter 2, I will explain the principles of charge neutralization with an ion gun, summarize the current status of the project, and discuss the remaining discharging difficulties and how they might be overcome.

1.3.4 Conductive coating

The oldest – and for many years only – charge elimination method has been to coat insulating specimens with a conductive film before introducing them into the sample chamber. Deposition by evaporation, sputtering, or plasma coating can produce films that are thin enough (1–10 nm) to allow high-resolution imaging and to preserve even fine topographic detail (Walley et al., 1971; Echlin, 1975; Suzuki, 2002, and many others; overview in Echlin, 2009, Chapter 11). The conductive film allows the surface charge to dissipate and provides a ground-potential surface, so that electric fields outside the sample are eliminated.

The implementation and evaluation of an automated in-chamber coating method for SBEM is the central part of this dissertation, presented in Chapter 3.

1.4 Cutting with a diamond knife

In this dissertation, 'SBEM' always refers to diamond-knife SBEM. For all experiments, I used a miniature diamond knife (1.5 mm width), custom-developed and produced for SBEM cutting by Diatome AG, Biel, Switzerland. The knife is firmly held in place in the SBEM microtome by a custom-made titanium holder.

The cutting plane of the knife is fixed; the sample is moved up and down. The whole microtome can be moved laterally, if tiling is used to image large surfaces. The increment the sample moves up after each image during stack acquisition determines the cutting thickness. Typical cutting thickness values are between 25 and 150 nm; cutting at 25 nm or below is considered 'thin cutting' in the following text.

In this section, I will give a brief overview about diamond-knife cutting and the role that beam damage is thought to play, and explain the motivation for developing a low-temperature SBEM microtome ('Cryo-SBEM'). Cryo-SBEM, the subject of Chapter 4, is the third project I have been working on during my doctoral research.

1.4.1 Parameters affecting cutting

The quality of cutting with a diamond knife is affected by several parameters: the knife forward speed, the clearance angle, the bevel angle, the oscillation frequency, as well as sample properties (such as the type of embedding). See Fig. 1.6 for an illustration.

Cutting with a diamond knife in the SBEM can be considered successful when the freshly cut surface does not show any cutting artifacts – chatter or knife marks – and when the cutting thickness between successive sections remains constant. A common problem is that the cutting thickness oscillates between thin and thick cuts. An extreme case of thickness variations are 'skipped cuts'. Cuts can also be 'wavy' when the cutting thickness is non-uniform over the imaged region. After an extended period of use, the diamond knife becomes dull, so that thin cutting becomes difficult or impossible, in which case the knife must be resharpened (by Diatome or other companies that offer this service).

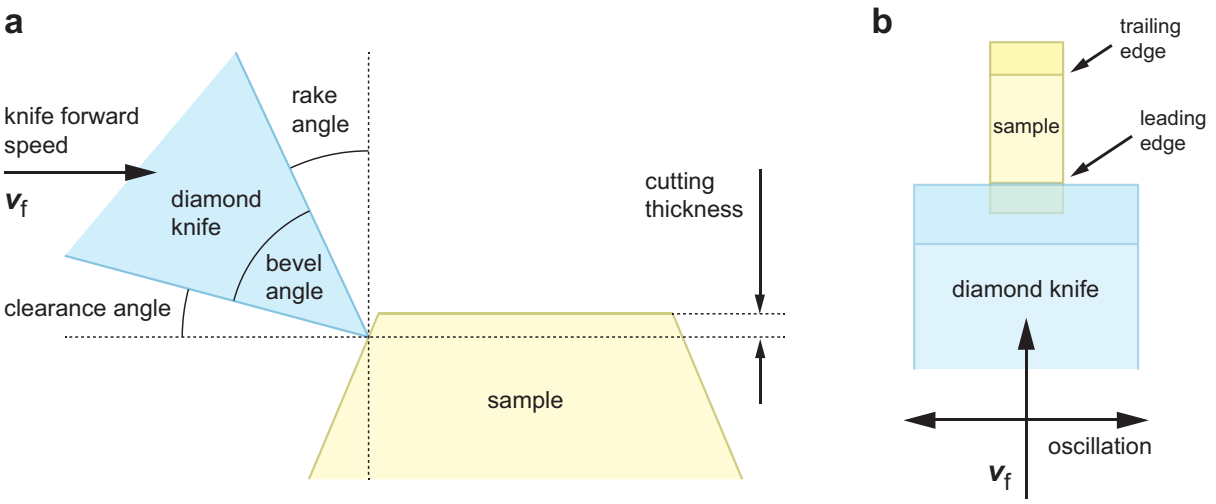

Fig. 1.6: Cutting with a diamond knife. (a) View from the side. The blade of the knife is about to cut into the edge of the sample. (b) View from above. The knife is 1.5 mm wide; the sample was usually trimmed to a width of several hundred microns. For SBEM cutting, typical values for the bevel angle are 45–55°, for the clearance angle 10–15°, and for the knife forward speed <0.2 mm/s.

Cutting can be improved for some samples when the knife is oscillated along the direction of the knife edge (Studer & Gnaegi, 2000). The oscillation is produced by a piezo driven with a sine wave (~30 V peak-to-peak). By trial-and-error experiments, an oscillation frequency of 12 kHz was found to work well for many cases. In some cases, the frequency had to be increased (up to about 20 kHz) to enable good cutting. If oscillation is found to be unnecessary, it should be left off, since the cutting debris accumulating on the knife had a higher likelihood to stay there and not fall off onto the sample when no oscillation was used (personal observation).

1.4.2 Beam damage and the effect of low temperatures

Just as light has a damaging effect in fluorescent imaging (bleaching caused by radiation damage), the electrons of the primary beam that raster-scans the surface in a scanning electron microscope inflict damage upon the sample (Egerton et al., 2004). In the field of electron microscopy, the terms 'beam damage' and 'radiation damage' are used interchangeably; in the following text, I will use 'beam damage' throughout to refer to the damage caused by the microscope's electron beam.

At an accelerating voltage of 2 kV (a typical value for SBEM imaging), each of the beam's electrons will be accelerated to a kinetic energy of 2 keV, or 3.2×10^{-16} J. Most of this energy is deposited inside the sample, causing various types of damage (Fig. 1.7).

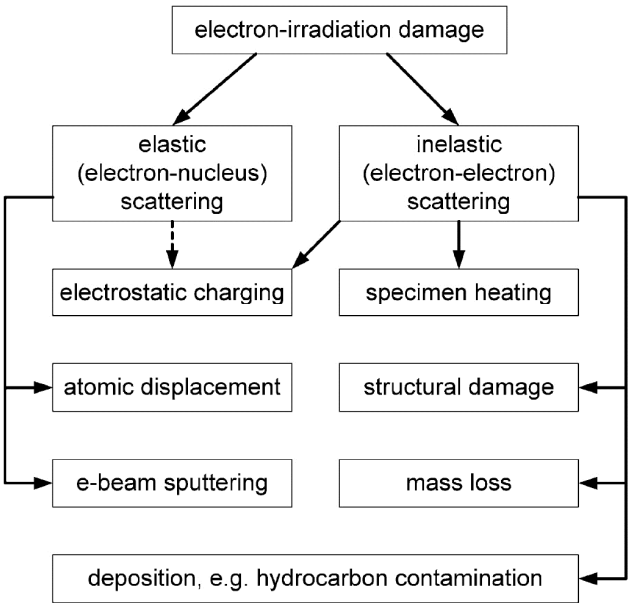

Fig. 1.7: Different types of specimen damage caused by elastic and inelastic electron scattering. Classification from Egerton et al., 2004.

For low kinetic energies – as in the case of SBEM imaging, where landing energies of 3 keV or less are used – the right side (inelastic electron-electron scattering) dominates: Incoming beam electrons interact with the electrons that surround the sample's atomic nuclei, thereby causing heating, structural damage, and mass loss. Damage is worst in organic materials. The incoming electrons break chemical bonds in the sample molecules, which changes their shape and shifts their position. The crystallinity of polymers is destroyed (Grubb, 1974; Egerton et al., 2004).

For TEM imaging, it is known that mass loss, an indicator of beam damage, is significantly reduced at lower temperatures (Lamvik, 1991). The reduction factor for beam damage effects that can be achieved by cryogenic cooling for TEM imaging varies considerably (3–100) with the type of material used (Egerton et al., 1987; Egerton et al., 2004).

How could lower temperatures reduce the effects of beam damage in the case of SBEM? A lower sample temperature does *not* reduce the energy deposited in the sample or the damage caused by the interactions between the primary beam electrons and the sample molecules. However, temperature has a strong effect on the

degree of damage caused by secondary reactions, since all chemical reactions are substantially slowed down at cryogenic temperatures.

When cutting with a diamond knife, structural stability of the sample is essential. This stability is compromised by the structural damage that occurs when too many electrons hit the sample. When damage is sustained from the electron beam, the chemical bonds of resin polymers can break and reform, causing cross-linking and an increase in sample brittleness (Grubb, 1974; Ungar, 1981). This may contribute to the problem of thin cutting at high electron doses. At small cutting thicknesses, the knife presumably just abrades the surface instead of cutting it off. Should too much damage have occurred, layers below the cutting plane may be ripped off when the knife blade moves through the sample, causing non-uniform cutting thickness.

To test whether cryogenic temperatures can reduce such effects of electron beam damage for SBEM imaging, a cryo-microtome was constructed that can be operated at about 100 K (see Chapter 4). Another low-temperature effect not related to beam-damage could be increased rigidity of the sample when cooled down, which may also yield improvements for thin cutting.

2 Charge neutralization with an ion gun

Negative charge building up on the sample surface during SEM imaging can be neutralized with positive ions. The ions can be supplied from low-pressure gas inside the microscope chamber: When passing through the gas, beam and signal electrons scatter with gas molecules and ionize them (low-vacuum method, see section 1.3.2). Another approach is to use an ion gun to generate the ions and focus them onto the sample surface under high-vacuum conditions (Fig. 2.1).

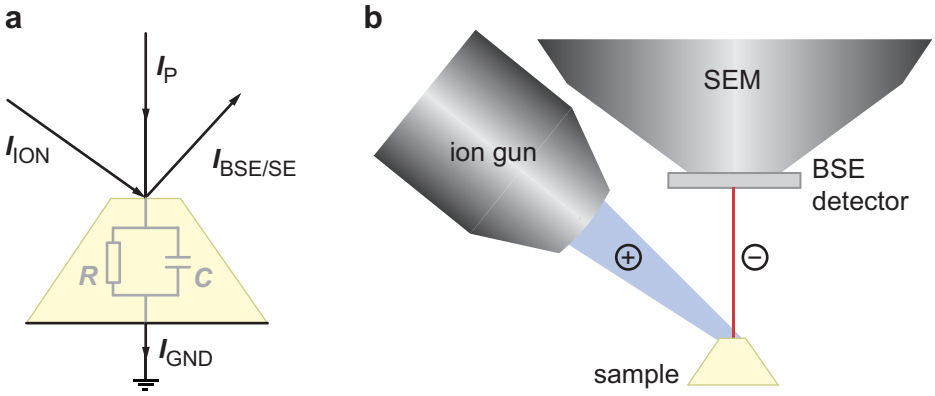

Fig. 2.1: Charge neutralization with an ion gun. (a) The SEM's electron beam transfers negative charge to the sample (I_P). The ion gun directs a positive ion current (I_{ION}) onto the sample to prevent the build-up of negative surface charge. (b) Schematic of experimental setup. Positive low-energy ions are supplied in high vacuum by an ion gun mounted inside the SEM chamber.

The use of an ion gun for charge neutralization was first explored by Charles Crawford, who used lithium ions to reduce charging effects for imaging non-conducting samples (Crawford, 1979). He also developed theoretical models of

insulator charge-up and of charge neutralization with low-energy ions (Crawford, 1980). However, the 'ion gun method' has not been widely adopted by other researchers, possibly because of the popularity of the low-vacuum method introduced at about the same time (Moncrieff et al., 1978, and others). Charge neutralization with an ion gun appears as an attractive alternative, since it permits imaging in high vacuum, thus avoiding the signal degradation that occurs during low-vacuum imaging.

For my diploma thesis (Titze, 2008), I modified a filamentless ion gun for operation inside a scanning electron microscope and carried out initial charge neutralization experiments. In this chapter, I will briefly summarize my previous work and then present further improvements and experiments carried out during my doctoral research.

At this stage, the ion gun setup delivers high ion current densities at low noise levels, but provides only partial charge neutralization when imaging at typical SBEM settings (16.5 nm pixel size, 150 pA beam current, 2.5 keV landing energy in the FEI Quanta). At the end of this chapter I will discuss potential reasons why full charge neutralization is not achieved in many cases.

2.1 Prior work

My diploma project (Titze, 2008) was a renewed attempt to use an ion gun for SBEM charge neutralization, following a similar project by a former diploma student (Fantana, 2006). The ion gun used by Fantana was based on electron-impact ionization (Model 1401, Nonsequitur Technologies, Bend, Oregon, USA): Positive ions were generated by accelerating electrons emitted from a hot tungsten filament against a stream of gas molecules. The filament's lifetime was short (less than 100 hours according to Fantana), so it had to be replaced frequently. During operation, the filament deteriorated, which reduced the magnitude and the stability of the ion current. Since long intervals of continuous and stable ion gun operation are required for the acquisition of large SBEM datasets, a mechanism of ion generation that depends on a hot filament did not appear suitable.

Therefore, a different type of ion gun was chosen for my diploma project – the model 'IonEtch', a microwave-driven filamentless ion gun (Tectra GmbH, Frankfurt am

Main, Germany; see Anton et al., 2000, for a detailed description of a similar prototype). Microwaves are used in the IonEtch to generate and sustain a plasma in a quadrupole magnetic field by exploiting the electron cyclotron resonance effect (Asmussen, 1989). Positive ions are continuously extracted from this plasma with two grids that determine the kinetic energy of the ions and the magnitude of the extracted current. The absence of a filament and of other parts likely to fail over time made this gun a suitable choice for long-term maintenance-free operation.

Initial experiments using the gun as delivered from the manufacturer showed that a large amount of noise was introduced to the BSE detector whenever the gun was operated inside the microscope chamber. The source of the noise was identified to be the magnetron inside the gun that was used to generate the microwaves. Replacing the magnetron with a 2.45-GHz signal generator and a chain of amplifiers reduced the noise to an acceptable level at which BSE imaging became possible while the gun was operating.

Since the IonEtch in its original configuration could produce only a broad ion beam, I developed simple ion optics (einzel lens design) using a charged-particle optics simulation program (SIMION, Scientific Instrument Services, Ringoes, NJ, USA). With the optics attached to the front end of the gun, higher ion current densities could be achieved (up to about 30 nA/mm² versus <2 nA/mm² without the optics, using an anode grid voltage of 40 V and a grounded extractor grid).

The first charge neutralization experiments with heavy-metal-stained epoxy-embedded retina samples showed that full charge neutralization could be achieved for low-magnification overview images (<1000x, >132 nm pixel size, ~150 pA beam current, on the FEI Quanta) in most cases. At higher magnifications, charging artifacts remained when charge neutralization with the ion gun was attempted. In a few cases, full neutralization seemed possible at higher magnifications (6000x, 22 nm pixel size, ~150 pA beam current), but I later discovered during my doctoral research that in many if not all cases the reduction in charging was overestimated, since the BSE detectors used for the experiments had lost sensitivity for low electron energies because of hydrocarbon contamination on the detector surface (see section 2.4.3).

2.2 Improved setup

During my doctoral research I made further improvements to the ion gun setup, which resulted in significantly higher current densities, a further reduction in noise, and better control and reproducibility of operating parameters. The new setup (Fig. 2.2) includes a custom-built microwave generator (section 2.2.1), improved ion optics (section 2.2.3), and new tools for precise aiming of the gun (section 2.3).

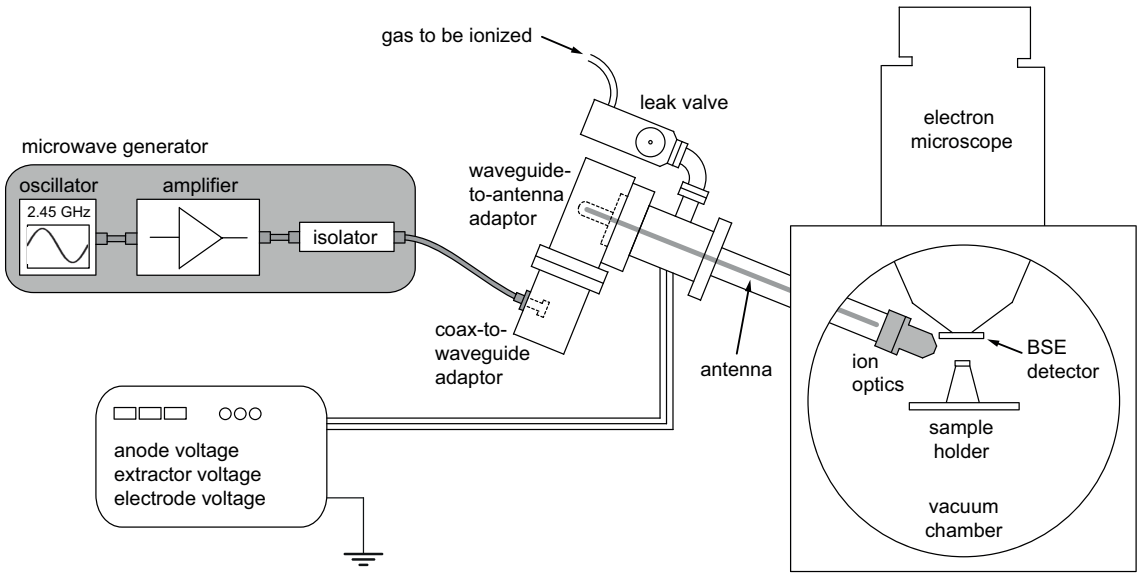

Fig. 2.2: Full ion gun setup. Microwaves are generated, amplified, and passed through an isolator into a waveguide. Via a custom-developed adaptor (Muegge Electronic, Reichelsheim, Germany), the microwaves are coupled to an antenna that transmits them to an alumina cup at the front end of the gun, where the oscillating electric fields sustain a plasma. The microwave generator (gray box) is shown in detail in Fig 2.4, the front part of the gun (gray), where ions are extracted and focused, in Fig. 2.5.

For all charge neutralization experiments, the ion gun (based on the commercial model IonEtch, Tectra GmbH, Frankfurt am Main, Germany) was mounted inside a Quanta FEG 200 scanning electron microscope (FEI Europe, Eindhoven, Netherlands), see Fig. 2.3. BSE imaging was performed with a silicon-diode detector (AXUV, International Radiation

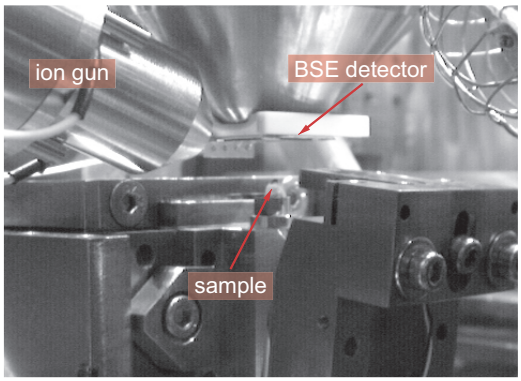

Fig. 2.3: Ion gun mounted inside the SEM vacuum chamber.

Detectors, Torrance, CA, USA; see also Funsten et al., 1997) that was attached to a custom-made plastic holder and fastened below the final lens of the microscope. SE imaging was performed with the built-in Everhart-Thornley detector.

2.2.1 New microwave generator

The initial microwave-generation setup consisted of a signal generator (SMHU 58, Rohde & Schwarz, Munich, Germany), a voltage-variable attenuator (ZX73-2500S+, Mini-Circuits, Brooklyn, NY, USA), a chain of three amplifiers (two pre-amplifiers, one main amplifier), and an isolator (a device that transmits microwaves in one direction only). The signal generator delivered a 2.45-GHz sine wave, which was amplified to a power between 5 and 20 W. The attenuator was used to control the microwave input power to the first pre-amplifier, thereby controlling the final output power. The amplifiers and the isolator were provided for testing purposes by Prof. Dr.-Ing. Georg Böck, TU Berlin.

For the continuation of the project during my doctoral research, the preliminary setup described above was replaced with a compact custom-built microwave generator. The large multi-purpose signal generator was replaced with a small local oscillator unit (KU LO 2450 PLL-297, Kuhne electronic, Berg, Germany; 110-mW 2.45-GHz sine wave output). The voltage-variable attenuator, the amplifier chain, and the isolator were replaced with a single 2.45-GHz power amplifier (AMT GmbH, Berlin, Germany), whose output power (up to 20 W) could be directly controlled with a potentiometer. The oscillator, the amplifier, and their respective power supplies were integrated into a single 19-inch rack module (Fig. 2.4a). An ampere meter was added to measure the amplifier current and display it on the front panel (Fig. 2.4b). This current was used to set the output power (Fig. 2.4c) while operating the ion gun.

The ion gun's plasma was always ignited with a high-voltage discharge. Very briefly, a high voltage of at least 1 kV is applied to the anode grid of the ion gun (the grid in direct contact with the plasma region) to produce a spark that ignites the plasma. This high-voltage discharge can damage the amplifier, because the decaying electric field travels from the plasma cup through the antenna, the waveguide and the coaxial cables to the amplifier output. After ignition, a fraction of the microwave power is continuously back-reflected to the amplifier from the burning plasma. An additional external isolator was used to protect the amplifier from these effects.

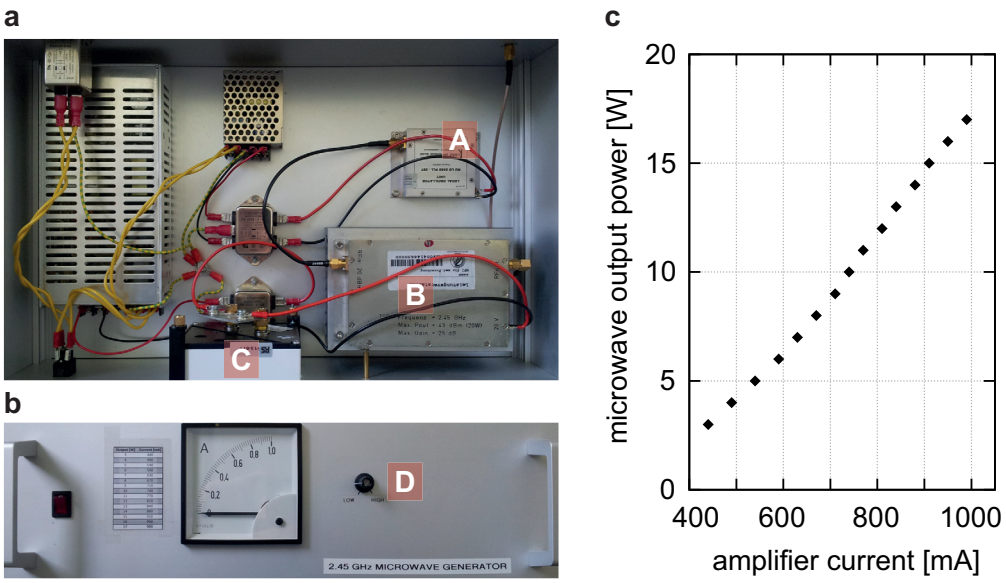

Fig. 2.4: Custom-built microwave generator. (a) Inside view of the device. A: Local oscillator; B: power amplifier with internal isolator; C: ampere meter, used to measure and display the amplifier current. An additional isolator added later to protect the amplifier during plasma ignition is not shown. (b) Front panel of the device. A potentiometer (D) is used to control the amplifier current. (c) Relationship between amplifier current and output power.

2.2.2 Anode grid and extractor grid

Two 'grids' (molybdenum disks with a central hole) provide the electric field to extract positive ions from the plasma (Fig. 2.5a, page 37). The anode grid is in direct contact with the plasma. The anode voltage, set to between 0 and 50 V for most experiments, determines the final kinetic energy of the ions, together with the intrinsic plasma potential (see section 2.5.1). The extractor grid is typically set to high negative voltages (around –1 kV) for applications requiring large currents (up to 10 mA/cm², Anton et al., 2000). In our case, connecting it to negative voltages produced plasma instabilities and noise problems. The grid was therefore permanently connected to ground for all charge neutralization experiments. This also minimized sputter effects on the extractor grid, since the kinetic energies of all ions hitting the grid were low.

The original IonEtch configuration (used during my diploma project) had an anode grid with a 1.5-mm aperture and an extractor grid with a 1.4-mm aperture. To determine the effects of different aperture diameters on ion currents and noise levels, I tested several configurations with custom-made grids (anode aperture diameters:

1.5 mm, 0.8 mm, 0.6 mm, and 0.4 mm; extractor aperture diameters: 1.4 mm and 0.8 mm). For the anode grid, a current maximum was reached for 0.8 mm. Further reductions in diameter to 0.6 mm and 0.4 mm significantly decreased the achievable currents, but also the light pollution inside the chamber (see section 2.4.2). The same observation (less light, less current) was made when a 0.8-mm extractor grid was used instead of a 1.4-mm grid. Overall, the combination of 0.8-mm anode grid and 1.4-mm extractor grid delivered the highest ion current densities (see section 2.4.1) and reduced noise from the plasma light compared to the 1.5-mm anode grid, by about a factor of 4 (as measured using image variance, explained in section 2.4.2).

The reason why an ion current maximum was reached when using the 0.8-mm anode grid can be explained as follows. Reducing the diameter of the aperture makes the area through which ions can escape the plasma and enter the ion optics smaller. Therefore, one would expect the currents to decrease. At the same time, however, the gas flow can be reduced when using a smaller aperture, to sustain a plasma at lower chamber pressures, which increases the current that can be extracted. For a 0.8-mm aperture anode grid, this effect seemed to more than compensate for the reduction in aperture area.

2.2.3 Improved ion optics

By the end of my diploma project, the highest measured ion current was 24 nA per 1-mm Faraday-cup aperture (average ion current density of 31 nA/mm²). During my doctoral research, several modifications of the ion optics that I will present in this section have increased the achievable ion current density more than ten-fold.

First, the local gas pressure inside the ion optics was assumed to be too high and potentially detrimental to the ion beam. Therefore, a new design was tested that contained holes in the metal shell of the optics to reduce the local gas pressure inside. This approach did not yield any noticeable improvements. The design was discarded because it caused more light pollution inside the chamber.

When returning to the original design without the holes and examining its focusing properties, I noticed that the ion current profiles were asymmetric and quite broad, which suggested problems in the ion optical path. When the focusing elements of the electrostatic lens were removed, I measured large ion currents (up to 5 nA per 0.5-mm Faraday-cup aperture, which corresponds to 25 nA/mm²) and a symmetric beam

profile. This unexpected focusing behavior was caused by oxidation and/or contamination of the inner metal surfaces of the ion optics. When ions hit these surfaces and their positive electric charge cannot flow to ground, electric fields begin to build up. This quickly leads to a steady state: The positive fields that are building up cause fewer ions to hit the surface. The overall result is a charging-induced focusing of the ions.

This observation revealed two flaws in the original design: First, the metal parts of the optics were made of aluminium, which oxidizes easily, so that over time the surfaces of the optics would become non-conducting. Second, the aluminium focusing elements inside the optics were held in place by Teflon rings that charge up when being hit by ions, which may also have contributed to the observed focusing problems.

The optics was therefore redesigned: All Teflon spacers were hidden from potential ion bombardment, and all aluminium parts were coated with gold (Weinbrecht & Kücherer, Pforzheim, Germany; see Fig. 2.5c) to prevent oxidation. In addition, before every experiment, all parts were ultrasonically cleaned with acetone to remove any residual contamination. After these steps had been taken, a control experiment showed that no charging-induced focus could be observed.

Another change was made to the ion optical path. SIMION simulations had shown that only those ions that emerge from the extractor aperture within a half-angle of about 10 degrees can be focused well by the ion optics. The other ions do not contribute to the ion current density in the focus and may instead cause other unwanted effects. Therefore, a beam-limiting aperture (baffle) was inserted directly after the extractor grid which cuts off the unwanted fraction of the beam. For the new design, the diameter of the baffle was reduced to match the half-angle obtained from simulations, and the baffle became part of a metal cylinder that was pressed against the extractor grid during assembly of the optics (Fig. 2.5a). This ensured that the baffle would be grounded properly (which was not the case in the previous design) to prevent charge-up caused by ion bombardment.

For the voltages of the anode grid (0–50 V) and the ion-optics electrodes (0–70 V), external power supplies (HAMEG Instruments, Mainhausen, Germany) were used to achieve better stability. The internal power supplies of the IonEtch control unit that were previously used were of low quality and introduced noise.

When the redesigned gold-coated ion optics were carefully aligned after thorough ultrasound-cleaning with acetone, much higher current densities were achieved (>300 nA/mm², an improvement of more than a factor of 10, see section 2.4.1).

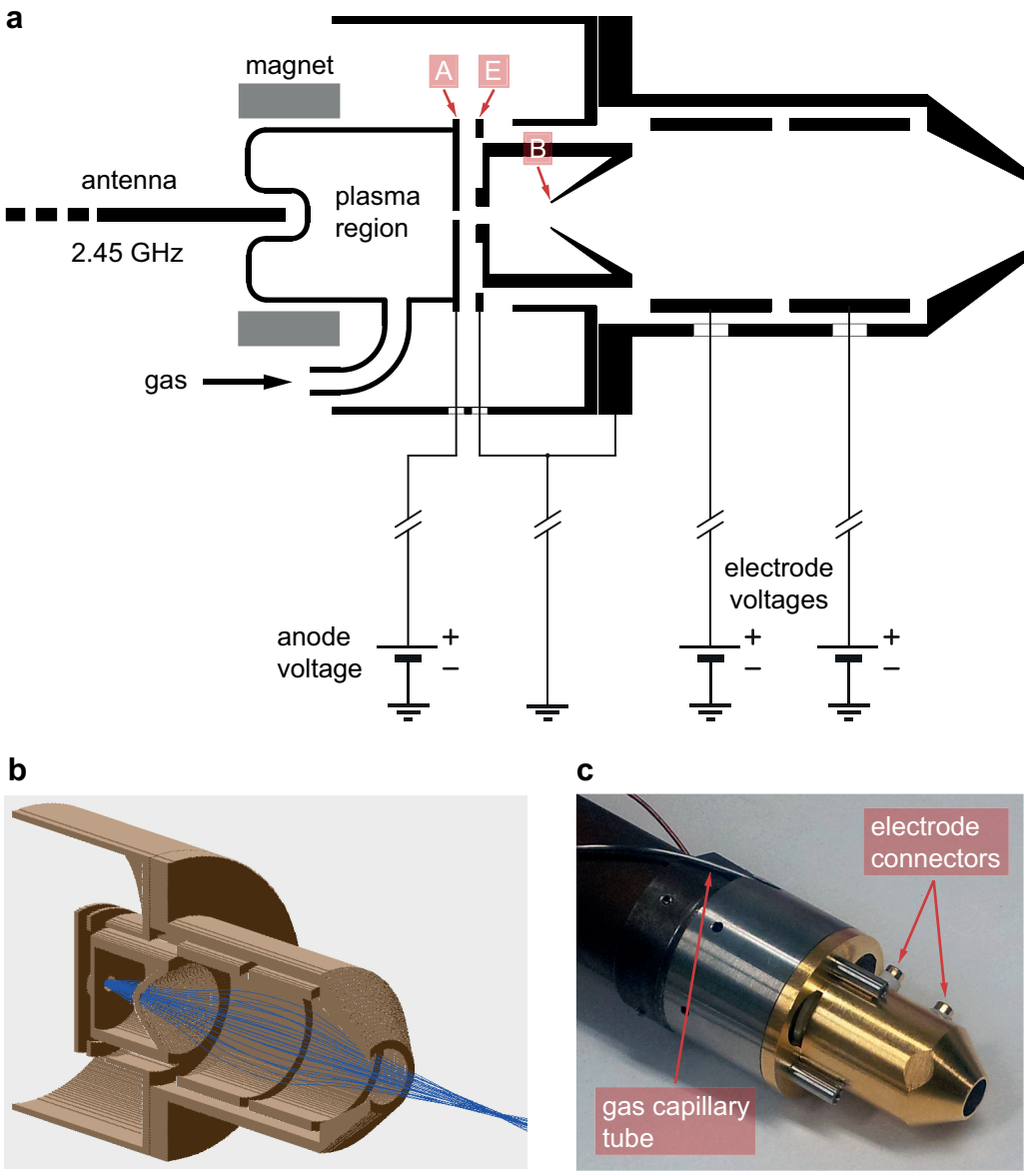

Fig. 2.5: Ion optics. (a) Front part of the ion gun with the custom-developed ion optics attached. Positive ions are generated in the plasma region. The plasma is sustained by microwaves delivered by the IonEtch antenna. Two grids extract the ions from the plasma: the anode grid (A) with direct contact to the plasma region, and the grounded extractor grid (E) next to it. After passing through the beam-limiting aperture (B), the ions enter the focusing field created by two cylindrical electrodes set to positive voltages. (b) SIMION simulation of the ion optical path. (c) Gold-coated ion optics attached to the front part of the ion gun.

2.3 Aiming and operating the ion gun

To direct the highest possible ion current onto the sample for optimal charge neutralization, the ion beam's focus must coincide with the sample surface. The position of the focus can be found by measuring the ion current with a Faraday cup whose surface is oriented towards the gun (Fig. 2.6).

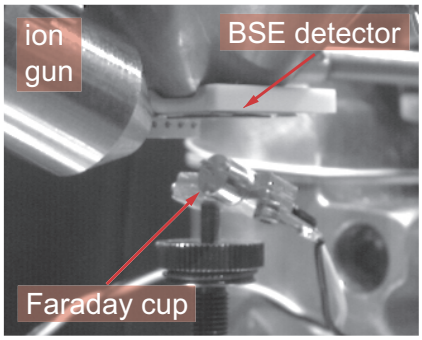

Fig. 2.6: Ion current measurement with a Faraday cup.

The focus of the beam can be moved to the sample position as follows: The Faraday cup aperture is placed directly below the microscope's final lens in the target working distance. While the ion current is being measured, the gun's aim is changed using the bellows assembly through which the gun is mounted until the maximum current is measured (see next page for detailed procedure).

The previous setup had allowed precise positioning by turning two screws of the bellows assembly, but it was not possible to record the screw positions. For the new setup, two high-resolution micrometer screws (New Focus, Newport Spectra-Physics GmbH, Darmstadt, Germany) were used that allowed to read off the screw positions, thus making the aiming reproducible (Fig. 2.7c).

During charge neutralization experiments, the silicon-diode detector used for BSE imaging had a bias voltage of −20 V applied to its p-n junction to reduce noise. This voltage, however, created an electric field that reached out from the detector surface and attracted the ion beam, especially when using low kinetic energies (anode voltage ≤20 V). This effect had to be taken into account when aiming the gun. Another field influencing the beam was created by the bias voltage (typically +300 V) of the ET detector. Even when the BSE imaging mode was used, this bias voltage remained on and had to be manually turned off using the FEI software before charge neutralization experiments.

With the Faraday cup used for all previous measurements (cup diameter: 16 mm; see Titze, 2008, and Fantana, 2006), measuring the ion current at the sample position (typically 6–8 mm working distance for the ion gun experiments) was not possible when the BSE detector was attached, since the Faraday cup would have bumped into

it. I therefore designed a new miniaturized Faraday cup that fit under the detector at short working distances (Fig. 2.6, Fig. 2.7a). In addition, the Faraday cup aperture diameter was reduced to 0.3 mm (previously 0.5 mm and 1.0 mm) to enable more precise measurements.

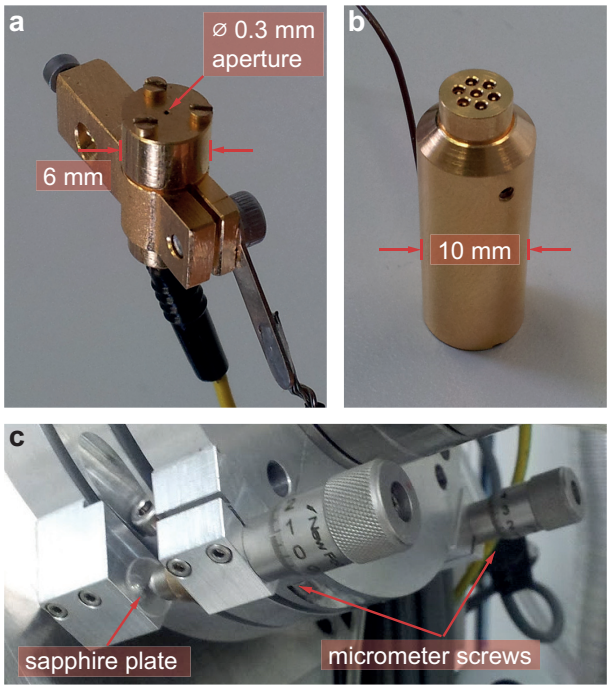

Fig. 2.7: Tools for current measurement and aiming. (a) New custom-built miniature Faraday cup for measurements at small working distances with the BSE detector in place. (b) Custom-made SBEM-compatible holder for aiming the ion gun. (c) Two micrometer screws for precise and reproducible aiming.

The following procedure was used to prepare and carry out charge neutralization experiments:

First, the miniature Faraday cup is attached to the sample holder of the standard FEI microscope door and moved below the microscope objective. Using BSE or SE imaging, the Faraday cup's hole is centered in the microscope's field of view, at an angle of about 25° to the horizontal, the surface containing the hole facing the ion gun. The working distance (from final lens to the hole) is adjusted to match the target working distance for SBEM imaging. This ensures that the Faraday cup hole is positioned exactly as the sample is positioned during SBEM acquisition.

When the microscope chamber has reached high vacuum ($<5 \times 10^{-4}$ Pa), the chamber pressure is recorded, and the ion gun's leak valve is opened to let in the gas to be ionized. I used helium, nitrogen and argon; other gases should also be possible, including reactive gases that could not be used in ions guns with hot filaments. The leak valve is then set to a position for which the chamber pressure reaches a value that allows reliable plasma ignition ($\sim 10^{-2}$ Pa). The microwave generator is switched

on and its output power set to 10–15 W. The anode grid is connected to a high-voltage power supply (>1 kV), and a button briefly depressed to cause a high-voltage discharge that ignites the plasma. A faint glow can be observed inside the chamber (with the built-in CCD camera), which serves as a confirmation that the plasma has been successfully ignited.

The chamber pressure is then reduced to the optimal minimum value by slowly closing the leak valve. If the plasma goes out because the gas pressure has become too low, it must be reignited by repeating the procedure described above. A chamber pressure just above the pressure necessary to sustain a stable plasma yields the highest ion currents (recommended by the manufacturer, confirmed in experiments).

After setting the anode grid voltage to the desired value (typically 20–50 V), the electrode voltage is increased until a positive current can be measured with the Faraday cup. The two electrodes can be set to different voltages; in most cases I set both to the same voltage for ease of optimization of operating parameters, since using the second electrode at a different voltage than the first did not yield much improvement. The aiming direction of the gun is varied with the two micrometer screws (Fig. 2.7c) to maximize the measured current. The electrode voltage is adjusted again to further maximize the current. This cycle of aim adjustment and electrode adjustment is repeated until the current maximum is found.

All settings are recorded: two values for the micrometer screw positions, the anode voltage, the electrode voltage(s), and the chamber pressure while the gun is operating. The difference between the chamber pressure before igniting the plasma and the chamber pressure during gun operation is characteristic for each gas and should be as low as possible. The best operating parameters were determined experimentally; they are presented in section 2.4.1 below.

The FEI door with the Faraday cup is then replaced with the SBEM door containing a sample for charge elimination tests. The chamber is evacuated and after high vacuum conditions have been reached, the plasma is ignited and all parameters previously recorded are reproduced.

To avoid the need to change doors, I designed a SBEM sample holder for aiming the gun (Fig. 2.7b). This holder contains seven metal pins directly below a grounded gold-coated surface with seven holes. Ion current falling onto the pins can be measured from outside the vacuum chamber. The magnitude of this current is not

equal to the full current measured by the Faraday cup, but its maximum still corresponds to the correct aim of the gun. The height of the holder can be adjusted, so that it exactly matches the height of the sample holder. The tip of the central pin will then be at exactly the same position as the sample surface. Maximizing the current falling onto this pin will maximize the current falling onto the sample surface.

2.4 Results

Even though high ion current densities could be achieved with the current setup, complete charge neutralization was restricted to imaging at low magnification (<2000x, pixel size >66 nm, ~150 pA beam current). For typical SBEM imaging parameters on the FEI Quanta (8000x magnification, 16.5 nm pixel size, 100–200 pA beam current, 2–8 μs dwell time, 2–3 keV landing energy), stable imaging of non-conducting samples (even if badly grounded or electrically floating) could always be achieved by using the ion gun. However, charging artifacts remained in cell bodies and blood vessels. In this section, I will summarize the findings, and in the following section, I will discuss conceivable reasons why areas of negative surface charge remain on the sample even as it is being irradiated with positive ions.

2.4.1 Ion current densities

Using the improved ion optics with a 0.8-mm anode grid (set to 40 V for argon or nitrogen and 50 V for helium) and a 1.4-mm extractor grid (grounded), the ion current densities given in Table 2.1 were reached. All currents were measured with a 0.3-mm Faraday-cup aperture positioned in the central region of the focus. The average densities were calculated by dividing the measured current by the aperture area ($A = \pi\ (0.3\ \text{mm})^2/4 = 0.071\ \text{mm}^2$). Since argon plasmas consistently yielded the highest current densities, I used argon for most charge neutralization attempts.

The highest ion current density measured with the current setup was 31.8 nA per 0.3-mm aperture (450 nA/mm² average ion current density), with argon, after careful optimization of all parameters, using the full microwave power available (~20 W), at a very low chamber pressure of 3×10^{-4} Pa (pressure difference only ~2×10^{-4} Pa), anode voltage at 40 V, and electrode voltage at 58 V.

	Helium	Nitrogen	Argon
Ion current density	175 nA/mm²	119 nA/mm²	320 nA/mm²
Pressure difference	~4×10^{-3} Pa	~1.2×10^{-3} Pa	~3×10^{-4} Pa
Anode voltage	50 V	40 V	40 V
Electrode voltage	56 V	49 V	56 V

Table 2.1: Current densities and the operating conditions under which they were measured. Anode grid: 0.8 mm diameter. Extractor grid: 1.4 mm diameter. Microwave power: ~15 W. The pressure differences listed are the differences between the chamber pressure before the ion gun is used and the chamber pressure during gun operation.

Current density profiles were measured for argon and helium (Fig. 2.8). A small asymmetry can be observed, which suggests that further improvements in aligning the ion optics should be possible. A precise alignment was found to be crucial to achieve high current densities. The ion optics are attached to the sputter shield of the IonEtch, which itself must be aligned with the axis of the anode grid and the extractor grid.

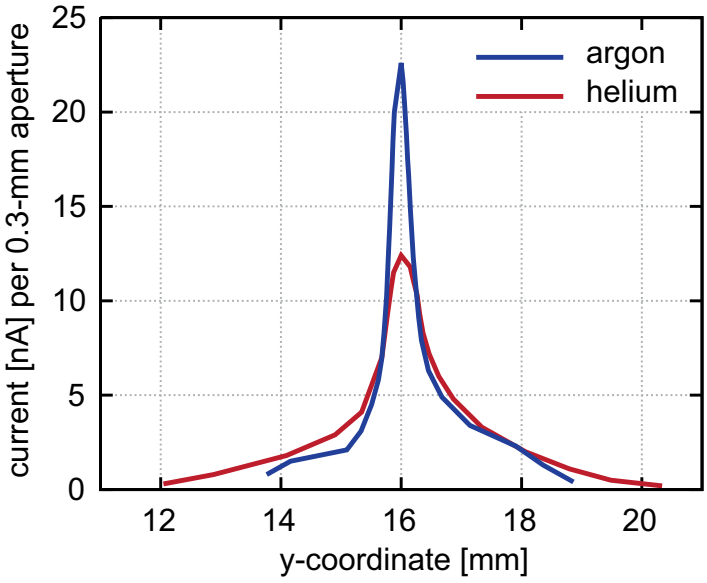

Fig. 2.8: Ion current profiles, measured with a Faraday cup, ⌀ 0.3 mm aperture. Argon beam: anode at 40 V. Helium beam: anode at 50 V. The profile maxima were centered at the 16-mm y-coordinate.

The following observations concerning the ion currents were consistently made in all experiments: (1) The highest ion currents could be extracted from the plasma at the lowest possible chamber pressures and the lowest possible pressure differences. (2) The required electrode voltage for optimal focusing increased as the chamber

pressure was lowered. This is presumably caused by a higher plasma potential at lower pressures that increases the ions' kinetic energy. (3) A higher microwave power yielded higher currents, but also increased the amount of light emitted from the plasma.

2.4.2 Noise from the ion gun

The ion gun's plasma emits light that shines through the anode aperture and the ion optics into the microscope's vacuum chamber, where some of it reaches the BSE detector. The light signal shifts the detector's dark current level (the current observed when the electron beam is switched off). Fluctuations in the amount of light reaching the detector cause additional noise. To quantify the amount of noise from the plasma, I have examined the variance of the dark current, measured with and without the ion gun operating, using the histogram function of ImageJ (image acquisition parameters: 8 μs dwell time, amplifier gain 16, contrast setting in FEI software: 0.5).

Using the 0.8-mm anode grid, which was used for the majority of experiments, the noise caused by the plasma light is very small: When the gun is not running, a typical dark current variance of 4 units² (standard deviation of 2 units) was recorded from the 8-bit gray-value histogram ('units' = gray-value intensity levels). When the plasma is ignited and the gun set to typical operating parameters (as in Table 2.1), the dark current variance increases to about 6–8 units² (standard deviation 2.4–2.8 units), which means that the additional noise variance caused by the light from the plasma is 2–4 units². For a typical SBEM image, taken at the above settings, signal variance is about 625 units² and noise variance 125 units² (for an SNR of 5). The extra noise caused by the light of the plasma is therefore negligible. Smaller anode grid apertures further reduce light exposure, but also reduce the magnitude of the extracted ion current.

Under two circumstances, however, the noise level is significantly higher and visibly reduces the SNR of the images: (1) If the chamber pressure is too low, the plasma becomes unstable, which causes large fluctuations in the light level. (2) Ions from the ion gun may reach the detector and cause additional noise. Since the detector has a negative bias voltage applied to its surface, setting the anode voltage to values of 20 V or below may increase this unwanted effect. Upward deflection of the incoming ions could also be caused by certain field configurations on the sample surface, and may depend on the sample geometry.

2.4.3 Charge neutralization

For all ion-gun charge neutralization experiments, epoxy-embedded retina samples were used (see Appendix B for details), which showed strong charging artifacts in high vacuum. Such samples usually require between 20 and 60 Pa of water vapor to minimize visible charging effects for typical SBEM imaging conditions (see pressure series in section 3.2.1).

Two preparatory steps can be performed to reduce charging effects to a level where reasonable imaging (with remaining charging artifacts) becomes possible in high vacuum: (1) The sides of the sample can be coated with gold to provide better grounding; (2) After embedding the sample in epoxy resin, it can be trimmed to expose the surface of the embedded neural tissue. If the exposed heavy-metal-stained tissue surface is then coated with gold, the bulk resistance to ground is significantly reduced.

In cases where no such steps are performed and an epoxy layer insulates the sample from a ground connection, the charges introduced by the electron beam quickly accumulate until the detector signal saturates and useful imaging is no longer possible.

When imaging such badly-grounded or non-grounded samples while bombarding them with positive ions from the ion gun, charging effects were significantly reduced, so that imaging always became possible (Fig. 2.9a). The positive current from the ion gun had the same effect as a grounding current I_{GND}. The image stabilized and distortions disappeared. However, charging artifacts in cell bodies and blood vessels remained. When imaging at low magnifications (>66 nm pixel size), charge neutralization with the ion gun was achieved in most cases (Fig. 2.9b, c).

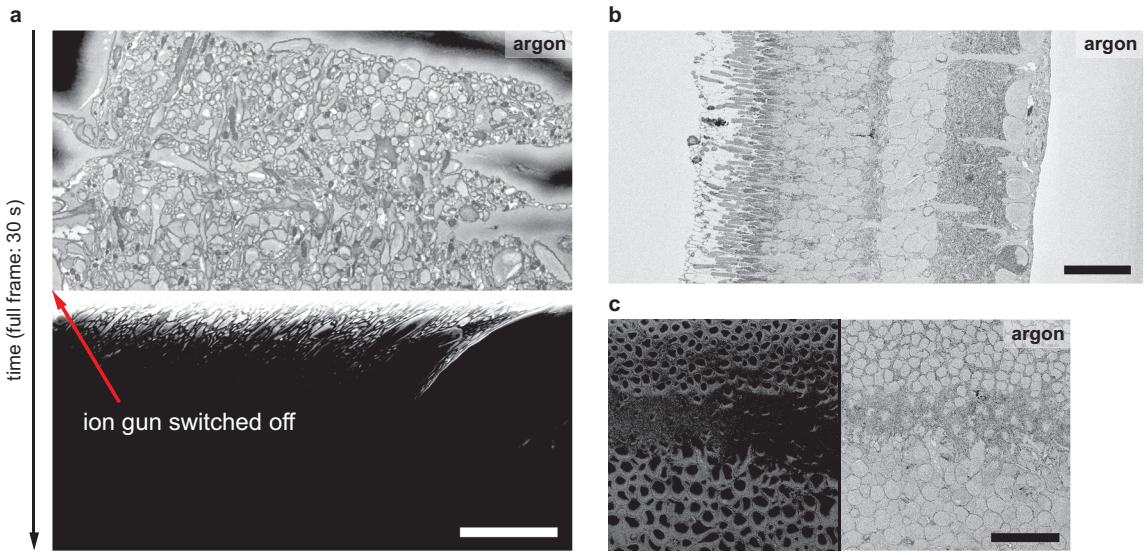

Fig. 2.9: Charge neutralization with the ion gun. BSE contrast used for imaging (~150 pA beam current, 3 keV landing energy). (a) A non-conducting badly-grounded retina sample imaged while the ion gun is operating with argon. As the gun is switched off (red arrow), the sample starts to charge up. Large distortions are visible before the detector signal saturates. Note that the initial decrease in signal (white stripe) is caused by the extinction of the plasma, which removes the plasma-light contribution to the detector signal. Scale bar: 5 μm. (b) Charge neutralization with the ion gun at low magnification. Overview image of a retina sample. Scale bar: 25 um. (c) Left: Ion gun is operating with argon using a 10-V anode voltage. The ion current is not sufficient for neutralization. Right: Ion gun operating at 40-V anode voltage providing sufficient positive current to neutralize the negative surface charge. Scale bar: 25 μm.

Three ion gun operation modes were tested for charge neutralization at typical SBEM imaging conditions (8000x, 16.5 nm pixel size, 150 pA beam current): (1) Adjusting all parameters to achieve maximum ion current densities and aiming the current directly at the sample, as described in section 2.3; (2) Using lower anode voltages (0–30 V) and non-optimal focusing parameters to direct a diffuse beam towards the sample. (3) Focusing the beam at a position over the sample surface (at a larger working distance).

In many cases, there were no clear performance differences between these approaches. Often, a well-focused beam did not offer improvements over a more diffuse one. None of the approaches succeeded in fully removing remaining charging artifacts in cell bodies and blood vessels at typical SBEM imaging parameters (8000x magnification, 16.5 nm pixel size, 150 pA beam current).

Several charge neutralization experiments yielded promising results (Fig. 2.10a): Charging artifacts were significantly reduced, to a similar degree as in low-vacuum neutralization.

However, the apparent reduction in surface charging shown in Fig. 2.10a is overestimated. The images were acquired with a BSE detector that had been in use for over a year. A comparison with a new detector of the same type revealed that the old detector had lost a significant amount of sensitivity (factor of 5 and higher for energies between 1 and 3 keV; almost full loss of sensitivity <1 keV). Charging in the cell bodies therefore appeared greatly reduced or was not detected at all. A detector of the same type with particularly low sensitivity was sent to the manufacturer

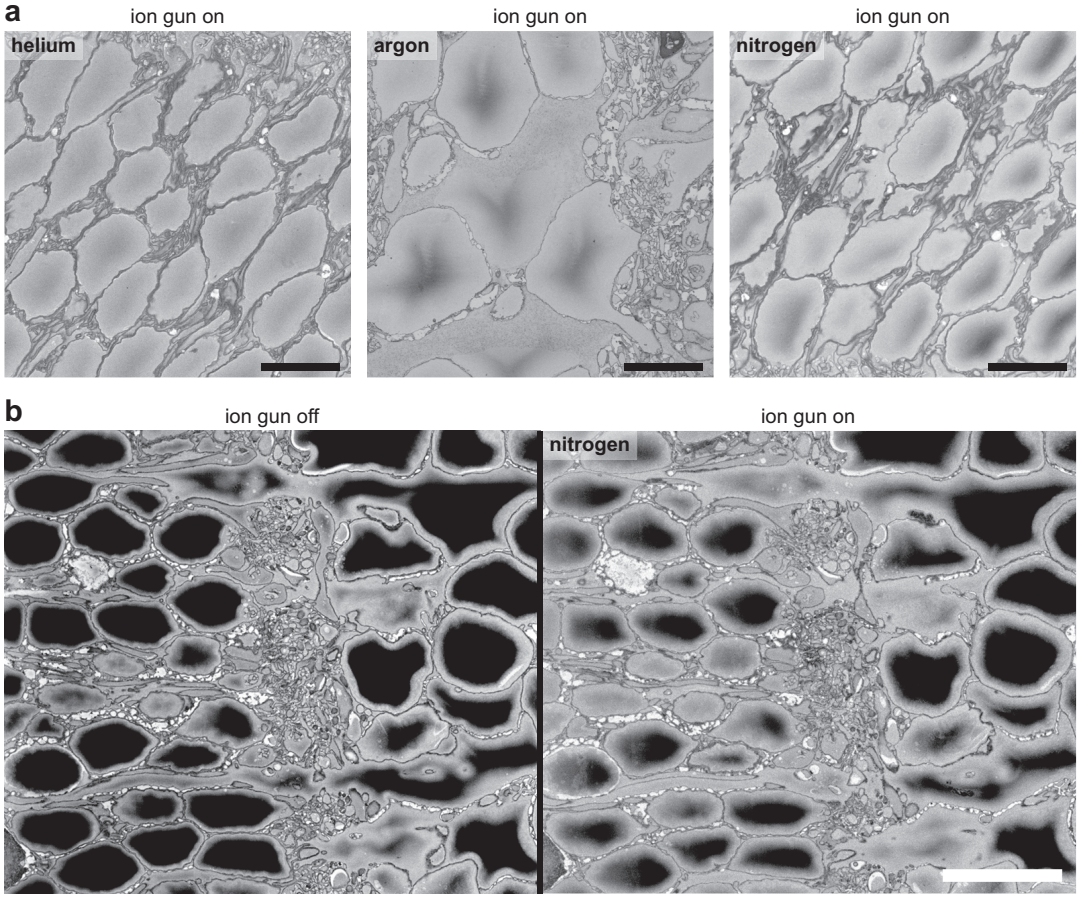

Fig. 2.10: Ion-gun charge neutralization examples for typical SBEM imaging parameters (8000x magnification, 16.5 nm pixel size, ~150 pA beam current, landing energy 3 keV). (a) Neutralization with helium, argon, and nitrogen ions. Images acquired with a well-used BSE detector. Scale bars: 5 µm. (b) Partial charge neutralization. Images acquired with a new high-sensitivity BSE detector. Left: Image acquired without the ion gun operating. Right: Image acquired while the ion gun was operating. Charging in cell bodies is reduced, but not eliminated. Scale bar: 5 µm.

(International Radiation Detectors, Torrance, CA, USA) for analysis. Measurements with an ellipsometer revealed that a 25-nm layer of hydrocarbon contamination had accumulated on the surface.

When using a new detector, the remaining charging in cell bodies always appeared much stronger than in the images in Fig. 2.10a. A typical case of incomplete neutralization is shown in Fig. 2.10b. Charging in the cell bodies is somewhat reduced, but the dark artifacts remain visible. A frequent observation that can also be seen in this image is that neutralization on the left side is a little bit better than on the right side of the image, which is the side from where the ion beam originates. The most likely reason for this effect, which was also observed by Fantana (2006), is discussed in the following section.

BSE imaging was used for almost all charge neutralization experiments. SE imaging was disturbed by stray electrons from the ion gun. Attempts could be made to suppress these stray electrons, but this direction was not pursued at this stage, since complete charge neutralization for BSE imaging has not been achieved yet, which is a prerequisite for SE imaging, since SEs are more strongly affected by surface charging than BSEs.

2.5 Discussion

The improved ion gun setup delivered high ion current densities (>300 nA/mm²) at low noise (2–4 units² additional image variance). While full neutralization could be achieved in most cases for low magnifications (<2000x, >66 nm pixel size), complete charge neutralization was not possible for typical SBEM imaging parameters (8000x, 16.5 nm pixel size, 150 pA). To discuss potential reasons why the ion gun could not neutralize remaining 'islands of negative charge' on the sample surface, we need to look more closely at the dynamics of charging and charge neutralization.

Our goal is complete neutralization of negative charge on the sample surface. In order to reach this situation, the positive current density supplied by the ion gun needs to at least match the average electron current density for a given field of view (FOV). Note that the electron current density used for the comparison is not the beam-current-per-spot-area density, which is many orders of magnitude higher.

For the electron current density $j_e = I_e/A_{\mathrm{FOV}}$ during typical SBEM imaging on the FEI Quanta (current: 150 pA, field of view A_{FOV} = 33.8 µm × 29.2 µm ≈ 1000 µm²), we obtain a value of j_e = 0.15 pA/µm².

For the ion current density, corrected by the factor of 1/sin(25°) = 2.37, because the ions are hitting the surface at an angle of 25°, we find for argon (current density from Table 2.1): j_{ion} = 320 nA/mm²/2.37 = 135 nA/mm² = 0.135 pA/µm².

The electron current density is slightly higher than the ion current density according to this calculation. However, we have overestimated the electron current density, since a certain fraction of the beam's electrons are backscattered and cannot contribute to the surface charge. We have also underestimated the ion current density, since the maximum density in the center of the beam is presumably larger than the average density measured with the 0.3-mm Faraday cup aperture. In addition, negative surface charge should attract the positive ions, further increasing the effective ion current density.

Using the upper estimate for the electron current density and the lower estimate for the ion current density, we find the following factors j_{ion}/j_e for different FOVs:

FOV [µm²]		j_e [pA/µm²]	j_{ion} [pA/µm²]	j_{ion}/j_e
250	(16000x, 8.25 nm)	0.6	0.135	0.23
1000	(8000x, 16.5 nm)	0.15	0.135	0.9
4000	(4000x, 33 nm)	0.038	0.135	3.6
16000	(2000x, 66 nm)	0.0094	0.135	14
64000	(1000x, 132 nm)	0.0023	0.135	59
256000	(500x, 264 nm)	0.00059	0.135	229

Table 2.2: Comparison between ion current density and electron current density for different FOVs. Values in parentheses in the first column are magnification and pixel size for the FEI Quanta at 2048x1768 pixel image resolution.

These comparisons suggest that there should be a comfortable margin in surplus positive current for charge neutralization at a magnification of 4000x (33 nm pixel size). However, the magnification had to be reduced to 2000x and below to achieve complete charge neutralization with the ion gun. At 2000x, the ion current density should exceed the electron current density by at least a factor of 14, according to my

estimates. In the remainder of this chapter, I will present two possible explanations why negatively charged regions on the sample surface persist, even in cases where positive ion current densities far exceeding the electron beam current densities are provided by the ion gun.

2.5.1 Ion energy distribution and positive surface charging

The low-energy ions produced in the plasma cup of the Tectra IonEtch have a rather broad energy spectrum, in contrast to the sharp spectrum of an electron-impact ionization gun (several eV full-width half maximum; see Fantana, 2006). This broad spectrum may have a negative influence on the ion gun's capacity to deliver positive charge to the imaged sample region.

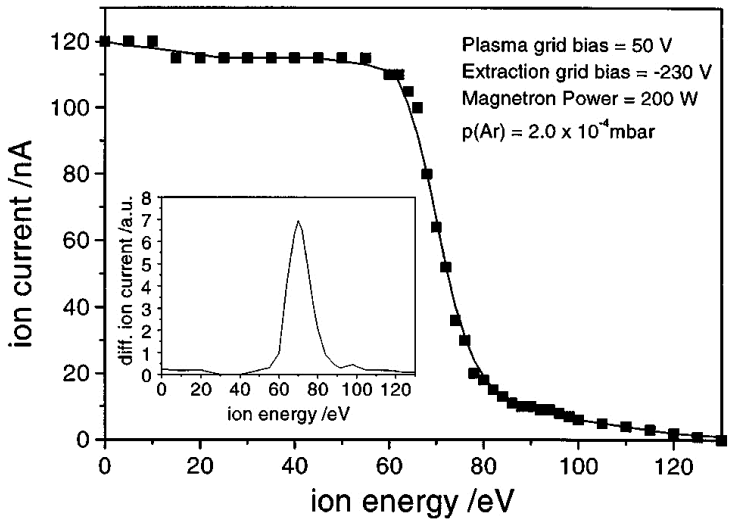

Fig. 2.11: Ion energy spectrum of a microwave-powered electron-cyclotron-resonance source. Full-width half maximum is 17 eV. Figure from Anton et al. (2000).

Let us first consider the idealized case of a perfectly sharp energy spectrum: All ions are generated at a potential of exactly 40 V and reach a kinetic energy of 40 eV when they hit the sample surface (initially at 0 V). Assuming that the surface is an insulator (epoxy resin, for example), the positive charge cannot be drained. The charge accumulates, thereby creating a positive surface potential that decelerates the incoming ions. As the charge-up process continues, the surface potential approaches 40 V. At 40 V, the flow of ions to the sample surface is stopped.

In the case of a broad energy spectrum, the sample surface will charge up to the voltage that corresponds to the maximum kinetic energy present in the spectrum. For an anode voltage of 50 V, the full width half maximum of the energy spectrum of an ion gun prototype similar to the IonEtch was measured to be 17 eV, with the peak of

the spectrum at about 70 eV. A noticeable fraction of the ions had energies of 100 eV and even higher (Fig 2.11).

How could this energy spread be detrimental for charge neutralization? When the anode voltage is set to 40 V, we can expect most ions to be at 60 eV (the 20-eV shift is caused by the plasma potential, see Fig 2.11). However, the ions at the high end of the energy spectrum may charge up the sample surface surrounding the region being imaged to potentials high enough to prevent ions with lower energies from reaching this region and contributing to charge neutralization. Within the region being imaged, the same problem can occur: Positively charged areas may shield negative islands of surface charge from bombardment by positive ions of insufficient kinetic energy. The analogous case for electrons with a broad energy spectrum was reported for an electron gun used for charge neutralization of insulating samples in X-ray photoemission spectroscopy (Larson & Kelly, 1998).

2.5.2 Ballistic ion trajectories

Another reason why charge neutralization remains incomplete could be the nature of ion trajectories. The ions generated in the ion gun have kinetic energies of several tens of electron volts. This may present a problem when the ions do not bombard the surface straight from above, but strike the surface at a low angle (about 25° in our case).

As the ions approach a sample surface with islands of negative charge, they will be attracted by these charges and their trajectories will become curved. Since the ions have low velocities, even small negative fields will have a significant impact on the trajectories. However, this does not ensure that the ions will reach the negative charges that attract them. In general, ballistic trajectories do not intersect with points of attraction, but instead 'overshoot' them. This may explain the observation that charge neutralization is less effective on the side of the sample that is closer to the ion gun.

In low vacuum, the situation is much more favorable for charge neutralization. The gas molecules are at room temperature; their kinetic energy is given by $E = \frac{3}{2}\mathrm{k_B}T = 6.07 \times 10^{-21}$ J $= 0.038$ eV, a small fraction of the kinetic energy of the ions provided by the ion gun. The ions generated in low vacuum experience a downward acceleration

from rest (close to 0 eV), which puts them on trajectories that are more likely to intersect the attracting negative charges on the surface.

How could the ion gun be modified to make full use of the available ion current for charge neutralization? To obtain a sharper energy spectrum, an energy filter could be included in the beam path. As a consequence, more current would need to be extracted from the plasma to compensate for the fraction of the current that is filtered out.

The problem of ballistic trajectories is more fundamental. A much steeper angle of ion bombardment would probably reduce the problem; ideally, the ions would be directed at the sample from above at a 90° angle. While it may be possible to make the angle steeper than the current ~25°, significantly higher values will not be possible because of geometric constraints. Ideally, positive ions at very low kinetic energies (close to 0 eV) should be generated and then directed at the sample surface to mimic the favorable conditions of low-vacuum neutralization. This, however, does not seem feasible with the IonEtch, since the ions are generated at a plasma potential and the extraction from the plasma further increases their kinetic energy.

3 Automated in-chamber specimen coating

A common method to prevent surface charging is to coat the sample with a conductive film before introducing it into the microscope chamber (see section 1.3.4). This, however, is incompatible with SBEM, where imaging and surface removal cycles alternate, with the sample remaining in place (see section 1.2).

In this chapter, I will present the development and evaluation of a new coating method* – automated in-chamber specimen coating – that can be combined with SBEM. Reliable surface charge elimination was achieved in all tested cases (for beam currents as high as 25 nA and sample surfaces as large as 1 cm^2). Thin films of palladium reduced SNR less than low-vacuum conditions (for pressures >20 Pa water vapor). Automated in-chamber coating was used to acquire SBEM stacks with BSE contrast (>1000 successive cut/coat/image cycles), stacks with BSE contrast using beam deceleration, and stacks with SE contrast. A new evaporator head was designed and built, with the aim to protect the filament during evaporation and to make more efficient use of coating material.

3.1 Setup

3.1.1 In-chamber coating system

A miniature electron beam evaporator ("e^--flux", Tectra, Frankfurt am Main, Germany) was mounted inside the vacuum chamber (Fig. 3.1b, inside view; Fig. 3.2, outside view) of either of two SEMs (Quanta FEG 200, FEI Europe, Eindhoven, Netherlands; MERLIN, Carl Zeiss NTS, Oberkochen, Germany).

* The main results presented here were previously published in Titze & Denk (2013). Text and figures from this publication are contained in this chapter.

The angle between the evaporator axis and the horizontal was 20° for the Quanta, and 34° for the MERLIN. The lower angle in the Quanta was chosen so that the coating could be combined with the operation of a silicon-diode detector for BSE imaging (AXUV, International Radiation Detectors, Torrance, CA, USA). SE imaging in the Quanta was performed with the built-in Everhart-Thornley (ET) detector. In the MERLIN, either the ET or the in-lens detector was used for SE imaging.

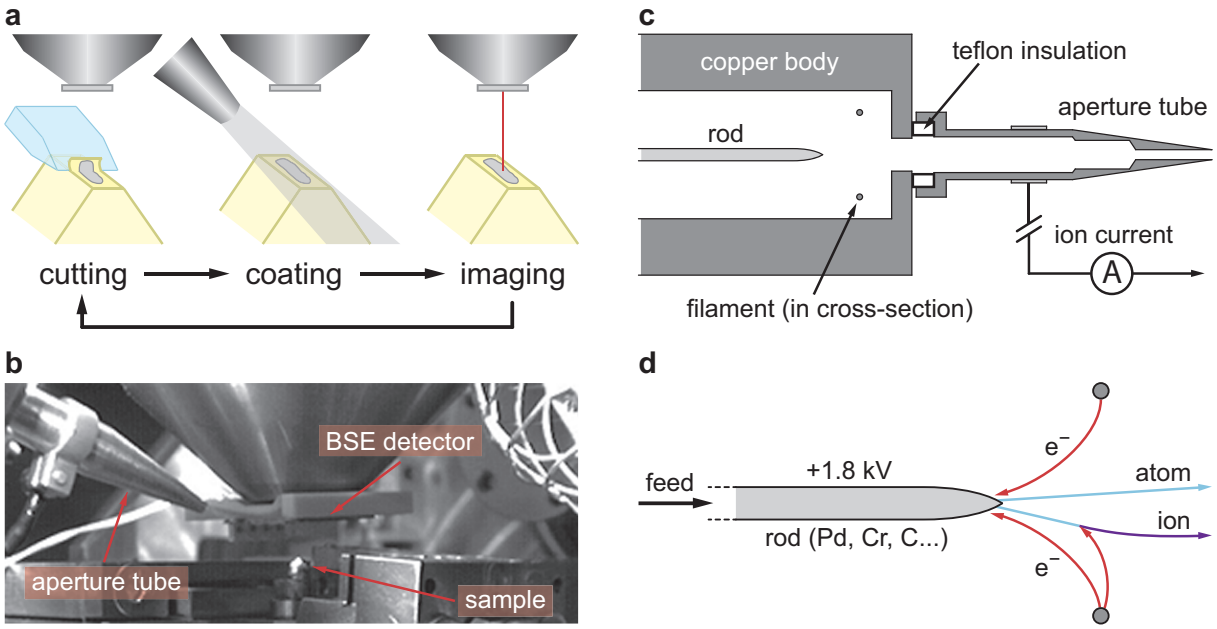

Fig. 3.1: (a) Automated in-chamber specimen coating. Each cycle consists of three steps: (1) A miniature diamond knife (Diatome AG, Biel, Switzerland) cuts off a thin section of the sample to reveal a fresh surface. (2) The sample is coated until the desired coating thickness is reached. (3) The coated surface is imaged with the SEM. (b) The evaporator in operation during a stack acquisition inside the FEI Quanta. The sample is brightly lit by the light emitted from the heated rod. (c) Cross-section through the front part of the evaporator showing rod, filament, and the aperture tube. (d) The evaporation process in detail showing how the rod is bombarded with electrons from the filament, the evaporation of atoms, and the ionization process.

The evaporator was operated in high vacuum (<5 × 10^{-4} Pa) at an accelerating voltage of 1.8 kV. For most experiments involving stack acquisition, chromium (Cr) and palladium (Pd) rods were used as coating material (MaTecK, Jülich, Germany), with purities of 99.95% and 99.9%, respectively. Initial coating tests were performed with carbon, titanium, vanadium, iridium, and platinum (see sections 3.2.2 and 3.2.3).

During the coating cycle, the emission current, which – together with the accelerating voltage – determines the heating power and hence the temperature of the rod end from which the material evaporates, was kept at a preset value (typically 11–13 mA for Cr, and 9–11 mA for Pd) by modulating the amount of thermionic emission from a filament (tungsten wire, ⌀ 0.3 mm, 1.5 circular turns; Goodfellow, Bad Nauheim, Germany) via the filament current (typically between 7 and 8 A). A small fraction of the evaporated atoms is ionized by incoming electrons (Fig. 3.1d), yielding a positive ion current, which was used to track the coating thickness (see section 3.2.4). During operation, the copper body of the evaporator head was continuously water-cooled (Neslab RTE-111 chiller, Thermo Fisher Scientific, Waltham, MA, USA; custom-made interlock with flow sensor BFS 300, Bavaria FluidTec, Maisach, Germany).

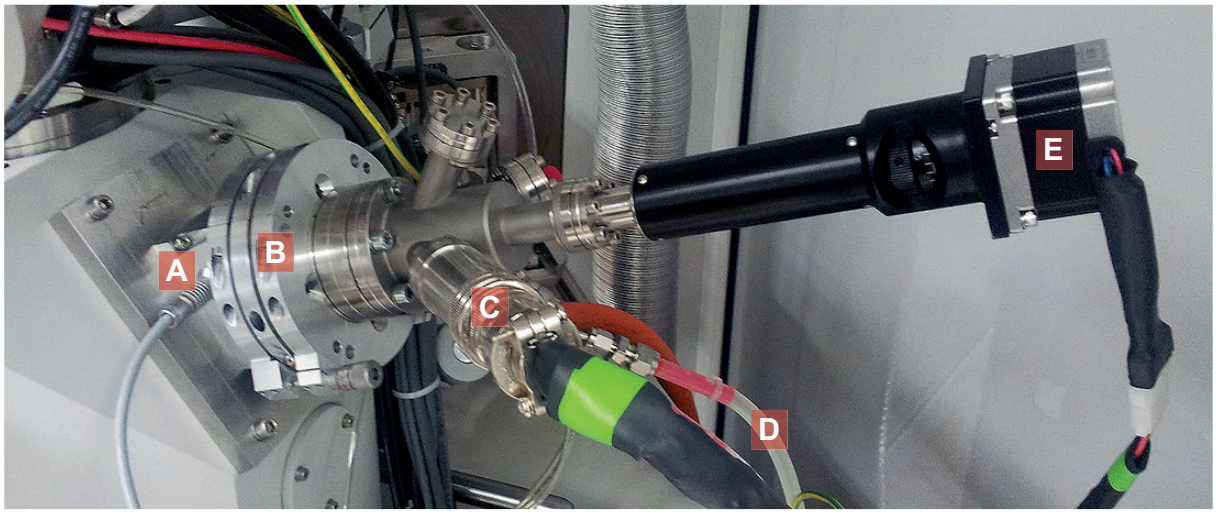

Fig. 3.2: Automated electron-beam evaporator, mounted onto SEM chamber. (A) Vacuum feed-through for ion current measurement, (B) Bellows assembly for aiming the evaporator, (C) Connector for filament voltage and rod high voltage, (D) water cooling lines, (E) Motorized rod feed.

The e^--flux evaporator head was modified as follows. To restrict the area that is coated, a conical aluminium tube with an aperture at its end was attached to the copper plate at the end of the head (Fig. 3.1c). The tube had a circular opening (⌀ 1.5 mm) and a length of 40 mm for the e^--flux setup in the Quanta microscope, where SBEM stacks of small samples were acquired. For the MERLIN, which was used for whole-brain imaging, a cylindrical aluminium tube was used (Fig. 3.3a). Its front part was adjustable along the evaporator axis and had either an elliptical (major axis ⌀ 7.5 mm) or a circular opening (same diameter) about 30 mm from the rod end. This ensured that the entire block-face, but not much more, was coated. To minimize

material deposition onto the vacuum chamber walls by atoms emerging from the rear of the evaporator, a cylindrical cover shield was placed over the evaporator head.

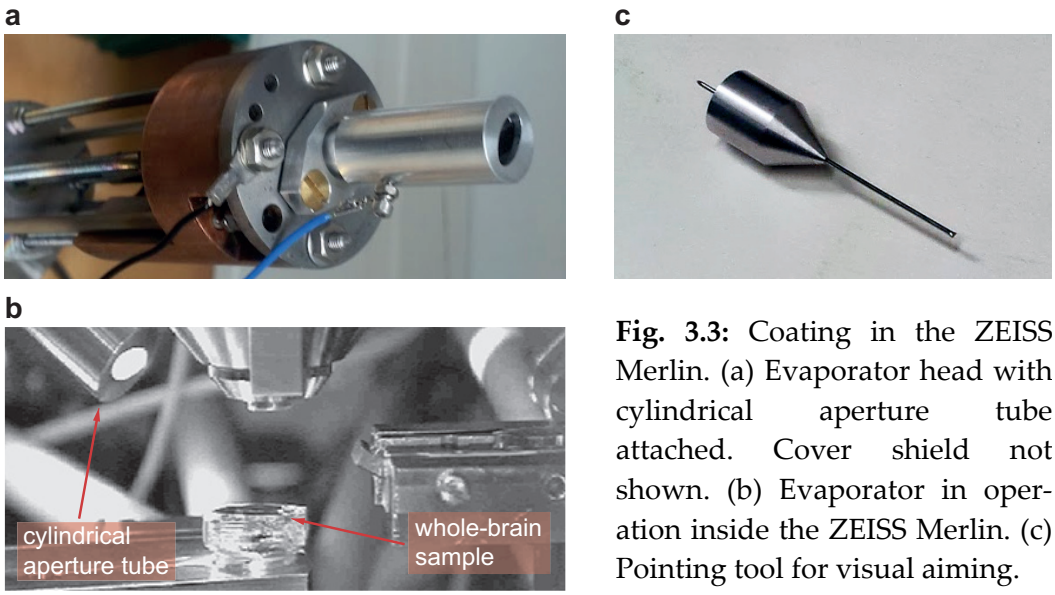

Fig. 3.3: Coating in the ZEISS Merlin. (a) Evaporator head with cylindrical aperture tube attached. Cover shield not shown. (b) Evaporator in operation inside the ZEISS Merlin. (c) Pointing tool for visual aiming.

The aperture tube was electrically insulated from the rest of the head using Teflon gaskets and connected to an ion-current measurement system (Fig. 3.1c). At the Quanta microscope, the evaporator flange was equipped with a bellows assembly (Fig. 3.2) that allowed the coater to be aimed with high resolution using two micrometer screws, even while the system was under vacuum. For the MERLIN, a mounting flange was used that allowed some lateral adjustments of the evaporator position in the plane formed by the evaporator and electron beam axes. The evaporation direction could also be changed over a limited range, and only when the coater was removed from the vacuum chamber, by adjusting two sets of nuts clamping the evaporator head to four threaded rods that connected it to the main flange.

Where the coater was aimed could be determined as follows. Prior to coating, a pointing device was attached to the aperture, which contained an adjustable needle indicating the coating direction (Fig. 3.3c). During coating, the hot end of the rod emits light, part of which emerges from the conical aperture, illuminating the area being coated. This

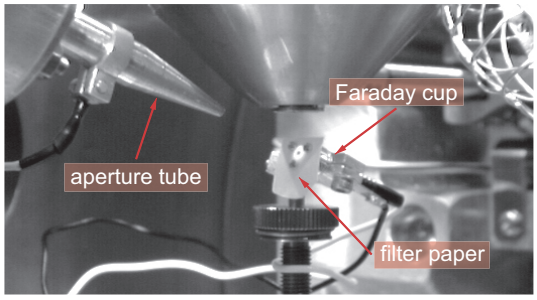

Fig. 3.4: Aiming the coater with a piece of filter paper placed on a miniature Faraday cup whose hole coincides with the target sample position.

can be seen by an in-chamber camera (Fig. 3.1b). An alternative and slightly more cumbersome procedure is to place a piece of filter paper at the sample position, perform a coating cycle, locate the dark spot that indicates where material is deposited, and adjust the aim accordingly (Fig. 3.4).

Each time after reaching high vacuum conditions in the SEM chamber, a standard outgassing procedure was performed before the first coating. After installing a new tungsten filament in the evaporator head, filament conditioning was required. Both procedures are described in the e^--flux operating manual (Tectra GmbH).

3.1.2 Control of the coating process

The positive high voltage of the rod, the emission current, the filament current, and the motorized feed were remote-controlled via an RS-232 serial connection to the modified control unit of the evaporator. The control unit was equipped with a custom-developed circuit board incorporating an ATmega328 microcontroller (ATMEL Corporation, San Jose, CA, USA).

LabVIEW (National Instruments, Austin, TX, USA) was used to provide an interface to set all parameters, monitor emission and ion currents as well as the filament voltage, and to automatically run the evaporation cycle (Fig. 3.5). The ion current was detected, amplified, and filtered by a custom-made electronic circuit. The filament voltage was used as an indicator of filament stability during long-term operation.

Before carrying out a single coating or a series of coating cycles, the rod high voltage was switched on and remained constant throughout. Each coating cycle began by increasing the filament current until the desired emission current was reached (5–10 s). During evaporation, ion and emission currents as well as the filament voltage were continuously monitored (Fig. 3.5a).

The ion current falling on the aperture tube was used to control the amount of material deposited. During each coating cycle the ion current was monitored and the filament current was turned off as soon as the integral over the ion current reached a preset value (Fig. 3.5a). BSE imaging commenced no earlier than 5–10 s after turning off the filament current to prevent the afterglow of the rod from polluting the silicon-diode detector signal.

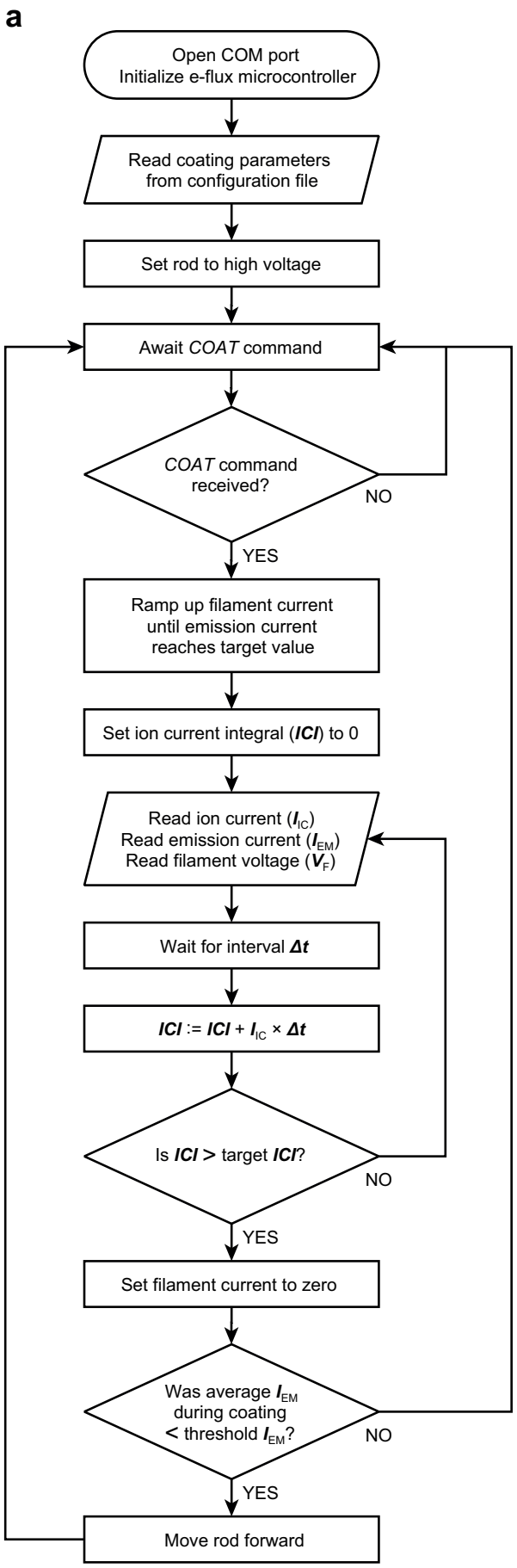

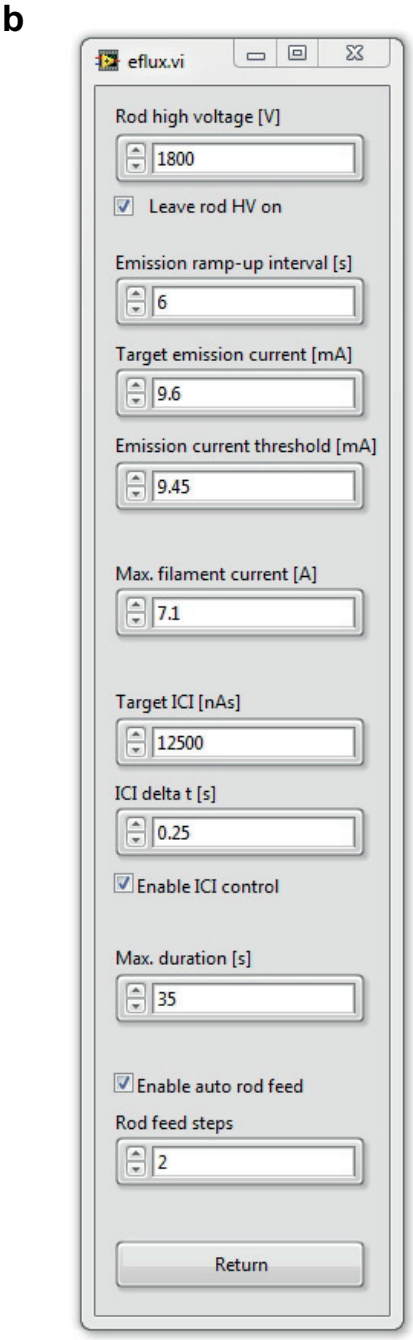

Fig. 3.5: Coating control. (a) Flow chart of the coating process (several minor steps not shown). The "*COAT* command" is sent by the ImageJ script that controls the SBEM acquisition. The LABView program transmits instructions to the microcontroller installed in the e⁻-flux. (b) LABView subpanel for setting coating parameters (typical settings for palladium are shown).

The relation between coating thickness and ion current integral was measured inside the SEM chamber using a quartz-crystal thickness monitor (Leica EM QSG 100, Leica Mikrosysteme, Vienna, Austria). All film-thickness values in this study were calculated by dividing the mass per coated crystal area, which is what is measured, by the bulk density of the material used ('average mass thickness').

The emission current was monitored to control the rod-advance motor. When the tip of the rod recedes as material evaporates, fewer electrons emerging from the filament reach the rod. Initially this is compensated for by an increase in the filament current, which is used to control the emission current, but eventually the filament current reaches a set upper limit and the emission current drops. When the average emission current during the coating cycle falls below a preset threshold (~98%), the rod is moved forward by a predefined distance (typically 120 µm).

All rods (⌀ 2 mm) used for evaporation were cut to lengths between 50 and 60 mm. A motorized linear feed (L-2151-2, 50 mm range; Huntington Mechanical Laboratories, CA, USA,) was used to move the rod forward (Fig. 3.2, page 55).

3.1.3 Samples and sample holder

The samples used for the coating experiments were epoxy-embedded heavy-metal-stained neural tissue (rabbit retina, zebra finch brain, and whole mouse brain; see Appendix B for more information). The sides of all samples were coated with gold (>25 nm film thickness) before introducing them into the SEM chamber, using an evaporation coater (BAL-TEC MED 020, Leica, Wetzlar, Germany). This ensured a stable low-resistance path to ground.

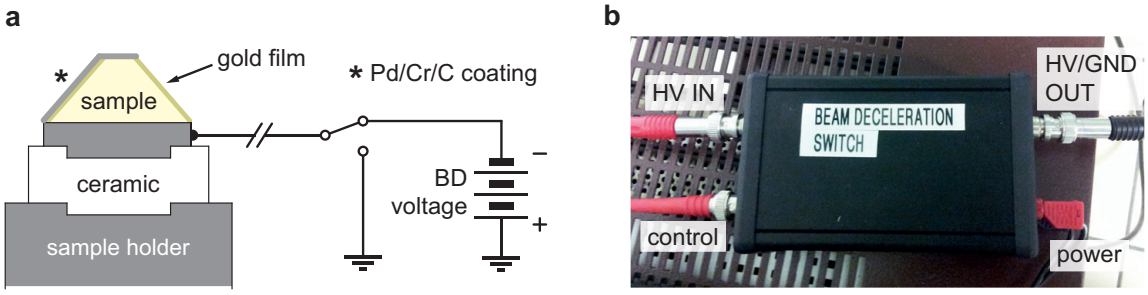

Fig. 3.6: Beam deceleration setup. (a) Sample holder for beam deceleration (BD) imaging mode. (b) Custom-built circuit for automatic switching between BD high voltage and ground, using high-voltage relays (H12–1A83 and H12–1B83, MEDER electronic, Singen, Germany).

For imaging with beam deceleration (see section 3.2.6), the sample was mounted on a custom-built insulating specimen holder (Fig. 3.6a) and connected either to the deceleration voltage (only during imaging) or ground (during coating and cutting) using a computer-controlled custom-made switch box (Fig. 3.6b).

3.2 Results

3.2.1 SNR degradation in low vacuum

For a quantitative comparison between the low-vacuum method and conductive coating, I measured how the SNR depends on the chamber pressure during low-vacuum operation (Fig. 3.7). For a landing energy of 2 keV, the SNR was reduced by more than 70% at a pressure of about 50 Pa, which is the pressure needed in case of the retina sample to sufficiently reduce charging artifacts at a beam current of ~150 pA (typical for imaging on the Quanta, see Fig. 3.8). The pressure needed for charge neutralization depends on several factors (personal observations): landing energy, beam current, pixel dwell time, and on the sample itself – with higher pressures needed for samples with lower intrinsic conductivity. For a given pressure, the SNR falls more steeply for lower landing energies (Fig. 3.7a) and larger working distances (Fig. 3.7b). SNR was estimated using autocorrelation (Thong et al., 2001; see Appendix A).

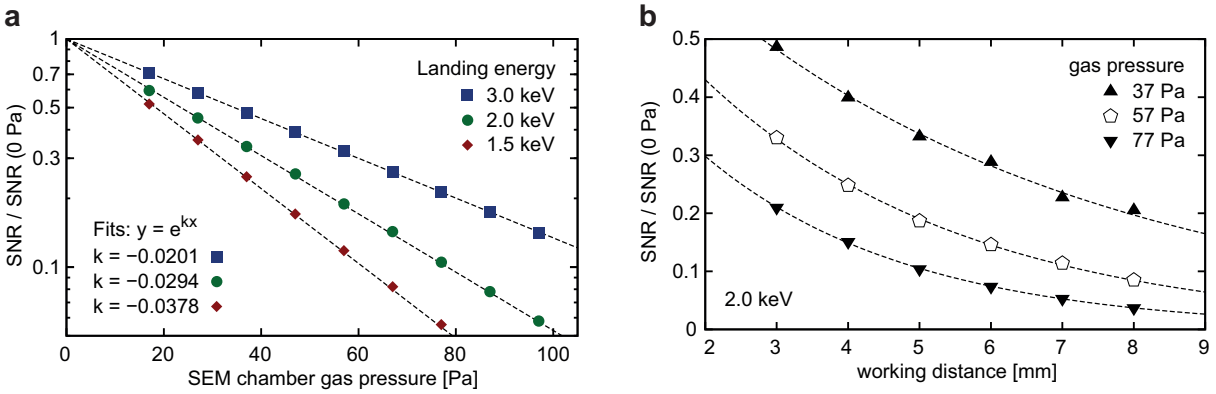

Fig. 3.7: SNR degradation in low vacuum. (a) Relative SNR as a function of chamber pressure (water vapor) for different landing energies at a working distance of 5 mm. Each data point represents the average of three measurements from a silicon square test sample (see Appendix A). (b) SNR relative to that at high vacuum as a function of the working distance. Each data point is a single measurement from the same silicon square sample.

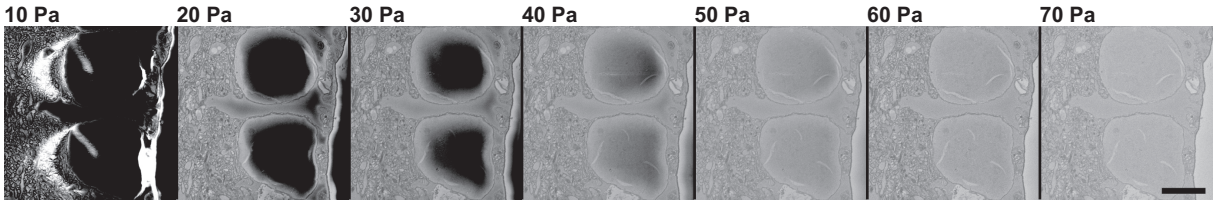

Fig. 3.8: Low-vacuum pressure series. Charging on the surface of a retina sample with low intrinsic conductivity is reduced as the gas pressure (water vapor) is increased. Landing energy: 3 keV, beam current: ~150 pA. Scale bar: 5 µm.

3.2.2 Initial coating experiments with carbon

Based on the fact that carbon forms fine-grained films, has a low atomic number, and can be evaporated from above using evaporation from a rod heated by electron bombardment (Walley et al., 1971), I performed initial experiments with carbon as the coating material (2-mm diameter rods, 99.997% purity; Goodfellow, Bad Nauheim, Germany). I successfully eliminated charging using carbon films several nanometers thick and manually performed in-chamber cut/coat/image cycles (Fig. 3.9), but found that the evaporator's tungsten filament degraded quickly and needed

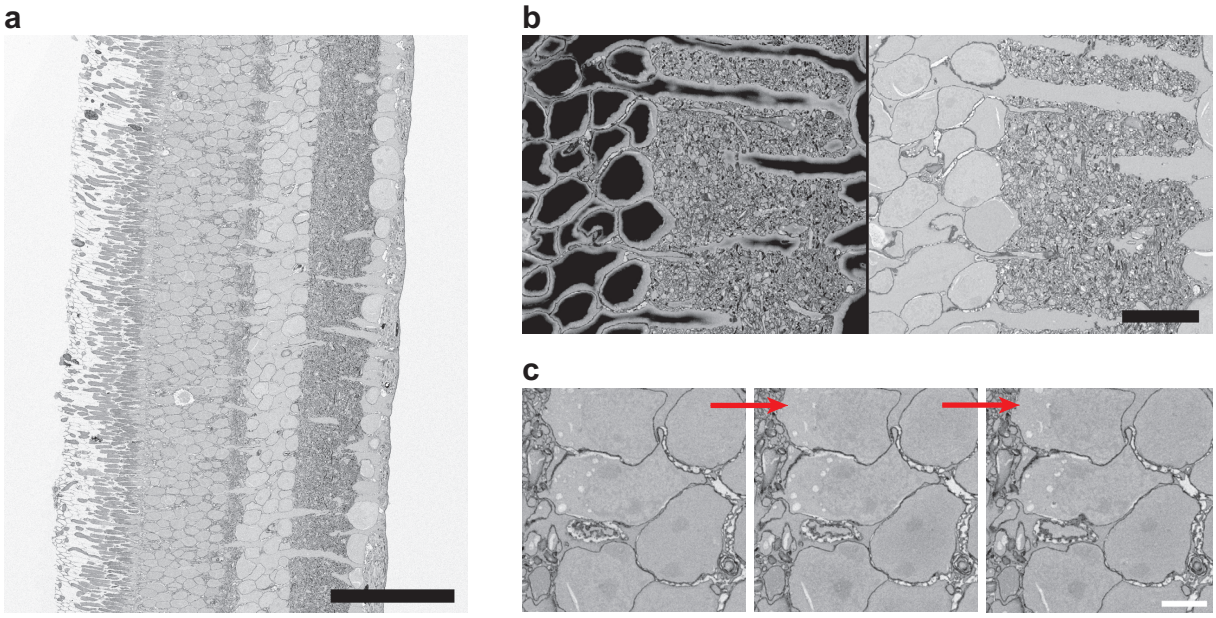

Fig. 3.9: Thin carbon films provide complete charge elimination for non-conducting retina samples at low (a) and high (b) magnification. (c) Successive cut/coat/image cycles with carbon (manual coating). Scale bars: (a) 50 µm, (b) 5 µm, (c) 2.5 µm. Images acquired at 3 keV landing energy and ~150 pA beam current.

to be replaced after fewer than 100 evaporation cycles, presumably because it reacted with evaporated carbon to form tungsten carbide. In addition, frequent high-voltage arcing and severe debris issues due to poor film adhesion inside the evaporator head (flakes of debris causing short-circuits and blocking the aperture tube) prevented reliable operation. Since electronic components in the e^--flux control unit were repeatedly damaged by arcing, a choke (DEODAN El 60/21, 68 μH; Tauscher Transformatorenfabrik, Freyung, Germany) was added to the high-voltage circuit to protect the control unit against current peaks, and a galvanically isolated serial connector (Expert Opto Bridge 0402, Gude Analog- und Digitalsysteme, Cologne, Germany) was used to protect the computer controlling the setup.

3.2.3 Chromium, palladium and other coating materials

While the difficulties with carbon evaporation eventually led to the development of a new evaporator head (see section 3.3), several alternative coating materials were tested for rod evaporation with the standard e^--flux evaporator head.

I found chromium to be more suitable than carbon, because it evaporates at sufficient rates below 1200 °C, much less than temperatures of >2000 °C needed for carbon (Echlin, 2009, Chapter 11), and did not appear to cause filament degradation. Chromium films as thin as ~2 nm were sufficient for complete discharging (Fig. 3.10). However, when cutting SBEM stacks, I also found that the cutting quality gradually became worse. This was likely due to a chemical reaction of the diamond knife with chromium (Zhu et al., 2001), which degraded the cutting edge.

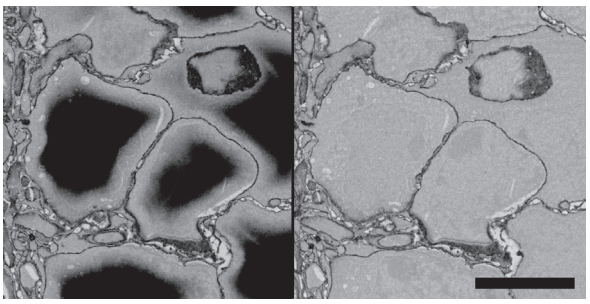

Fig. 3.10: A 2-nm Cr film removes all charging artifacts. Imaging parameters as in Fig. 3.9b. Scale bar: 5 μm.

I then turned to palladium, which has a lower melting point than chromium (Cr: 1907 °C, Pd: 1555 °C; Lide, 2005), and was able to find coating parameters for a temperature that provided a reasonable evaporation rate while avoiding uncontrolled melting of the rod tip. Experiments performed by the knife manufacturer showed that cutting bulk chromium visibly damaged the knife blade

after only a few cuts, whereas no such damage was seen for palladium, even after over 100 cuts (Helmut Gnägi, Diatome AG, personal communication).

Although the advantage of carbon is its lower atomic number, which means less scattering of incident electrons and BSEs, advantages of chromium and palladium compared to carbon are (1) that they can be evaporated at much lower temperatures, requiring only ~10 mA of emission current compared to 65–75 mA for carbon, (2) their higher SE yields, and (3) much higher electrical conductivity (Table 3.1).

I also tested vanadium, titanium, iridium, and platinum (Table 3.1), but couldn't find coating parameters that ensured a reasonable evaporation rate while preserving stability of the rod. In the case of titanium, vanadium, and iridium, the rod tip started to melt as deposition was observed. Continuously growing spheres formed at the tip (Fig. 3.11), which prevented controlled evaporation. In the case of platinum, the molten material quickly dropped off the rod.

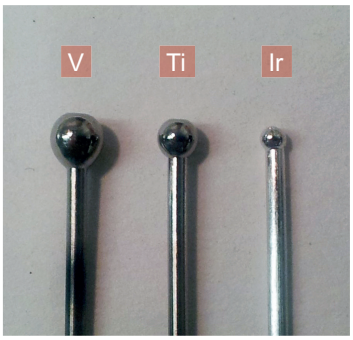

Fig. 3.11: Molten rod ends after evaporation experiments. Vanadium (V), Titanium (Ti), Iridium (Ir).

	Atomic number	Density [g/cm³]	Temp. [°C] at 1.3 Pa VP	Melting point [°C]	Resistivity [Ωm]	SE yield at 2 keV
Carbon (graphite)	6	2.0	2681	4489 (triple point at 10.3 MPa)	10^{-5}–10^{-4}	0.37
Titanium	22	4.5	1546	1670	390×10^{-9}	0.51
Vanadium	23	6.1	1888	1910	197×10^{-9}	n.a.
Chromium	24	7.2	1205	1907	125×10^{-9}	1.01
Palladium	46	12.0	1566	1555	105×10^{-9}	0.94
Iridium	77	22.6	2556	2446	47×10^{-9}	n.a.
Platinum	78	21.5	2090	1768	105×10^{-9}	1.22

Table 3.1: Relevant properties of the coating materials that were tested using electron beam evaporation from a rod. (Lide, 2005; SE yields from Lin & Joy, 2005). The temperature in the third column is given for a vapor pressure of 1.3 Pa (Echlin, 2009, Chapter 11). The resistivity of carbon (bulk resistivity given in table) increases exponentially with decrease in thickness for films <50 nm (Blue & Danielson, 1957; Morgan, 1971).

3.2.4 In-chamber coating

To make quantitive statements about coating thickness for in-chamber coatings, the relationship between the ion current integral (ion current integrated over full coating interval) and the coating thickness was measured (Fig. 3.12). For all coatings, this relationship was used to monitor deposition thickness (in nm) through the measurement of ion current integrals.

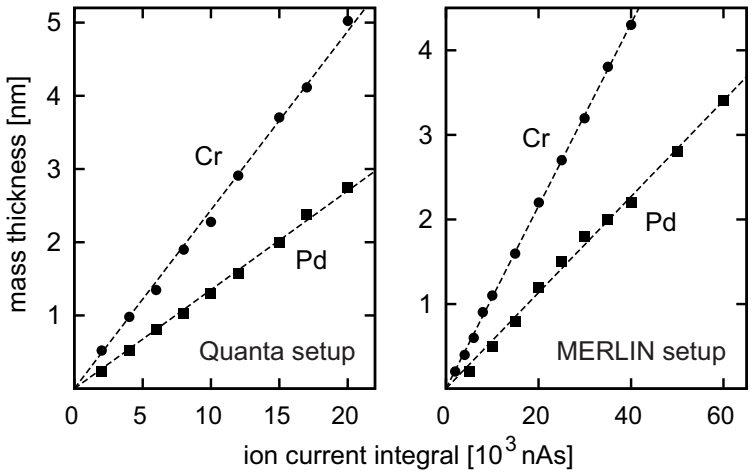

Fig. 3.12: Relationship between ion current integral and coating thickness. Using the conical aperture tube, I measured 0.135 nm coating thickness per 1000 nAs ion current integral for palladium at ~65 mm working distance in the Quanta. The slope for chromium was larger (0.244 nm/1000 nAs), presumably due to a different ionization probability. Right panel: Measurements in the MERLIN microscope with cylindrical aperture tube.

Thin in-chamber coatings reliably eliminated sample charging (Fig. 3.13) while retaining material contrast, which is used to resolve biological structures that are differentially stained with heavy metals. Although 1-nm-thick films usually eliminated visible charging effects during BSE imaging, slightly thicker films (1.5 nm) were needed to eliminate all charging artifacts during SE imaging, which is affected by even miniscule amounts of charging. Neither chromium nor palladium showed any noticeable grain structure at an imaging resolution as low as 5 nm (data not shown). Material contrast was retained to a large degree (see section 3.2.5 for quantification) for both BSE and SE imaging (Fig. 3.13a, b).

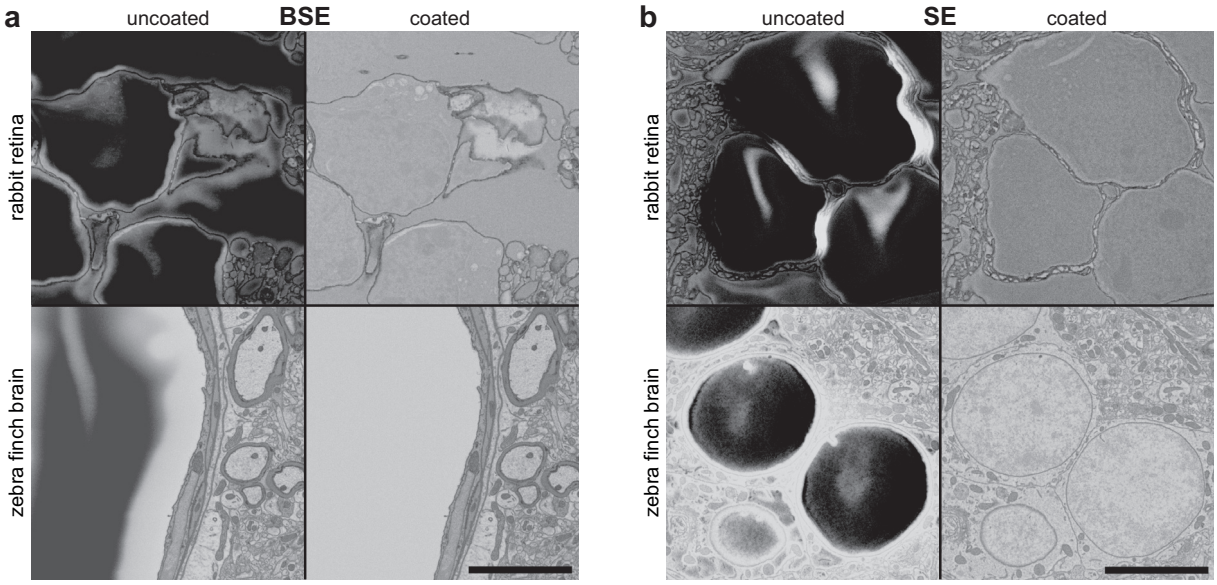

Fig. 3.13: Examples of charge elimination by in-chamber coating. (a) Rabbit retina (top) and zebra finch brain (bottom) imaged using BSE contrast without (left) and with (right) a 1.0–1.5 nm palladium film. Landing energies were 3 keV and beam currents 400 pA (top) and 130 pA (bottom), dwell times 4 μs, working distance 5.6 mm. (b) Same samples using SE contrast. Landing energies were 3 keV (top), 2.5 keV (bottom), beam currents 400 pA (top), 110 pA (bottom), dwell times 4 μs (top), 8 μs (bottom), working distance 5.6 mm. Scale bars are 5 μm.

Since evaporation from the tip of the rod occurs over a wide angular range, the expectation was that it should be possible to coat large areas. This was tested using a whole mouse brain that had been stained with heavy metals, embedded in epoxy resin, and cut to show a smoothed coronal block-face (Mikula et al., 2012). The sample (12 mm × 8 mm in surface area) showed strong charging effects, suggesting a low intrinsic conductivity, which made imaging impossible in high vacuum without a conductive film or at the charge-balance point.

When coated with either chromium or palladium (~2 nm thickness) the sample no longer showed any indication of charging over the entire surface area, even when using beam currents as high as 25 nA. At such currents, imaging was possible with reasonable SNR at pixel rates as high as 20 MHz (Fig. 3.14), the maximum pixel rate available on the MERLIN microscope.

Since the evaporation source is offset to one side (at an angle of 56° from the vertical), different parts of the surface receive different amounts of coating material. As a result, the film thickness is expected to vary by about ±15% from that at the center of

the sample, which should result in only a small variation in contrast at the landing energy of 5 keV used here. Chromium (but not palladium) coatings quickly became non-conductive in air due to oxidation, which prevented subsequent imaging.

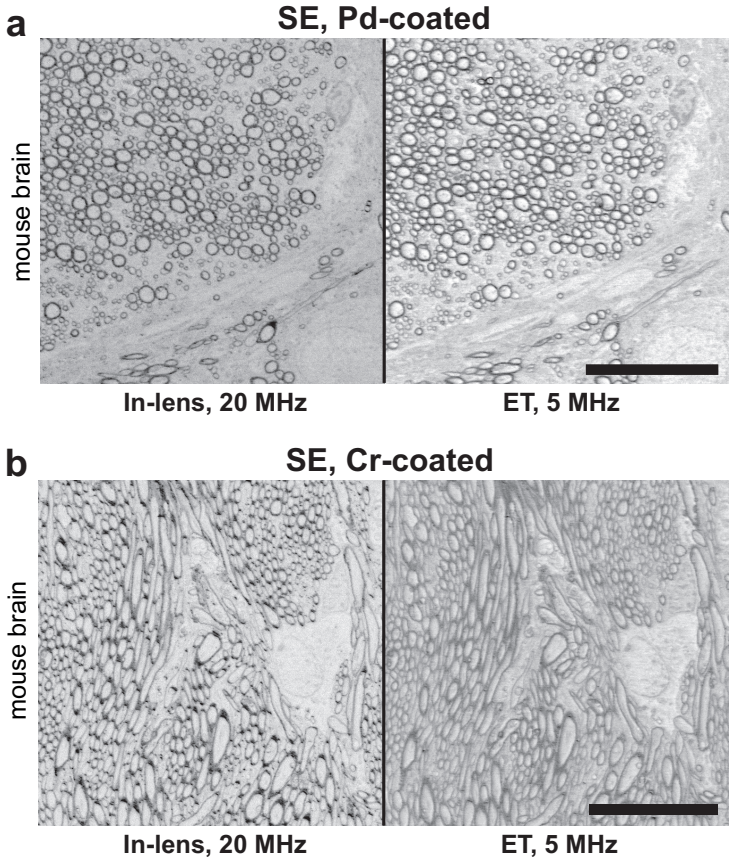

Fig. 3.14: Block-face images of cross section through mouse brain stained as whole. Samples in-chamber coated with ~2 nm palladium (a), and with ~2 nm chromium (b). In-lens SE (left) and Everhart-Thornley SE (right) detector images acquired at pixel acquisition rates of 20 and 5 MHz, respectively, at a landing energy of 5 keV, a beam current of 25 nA, and a working distance of 6.0 mm. Without coating, images could not be acquired in high vacuum due to very strong charging effects (not shown). Scale bars are 20 μm.

3.2.5 Effect of coating on SNR

Having established that the coatings provide reliable surface charge elimination, I quantified how the SNR depends on the coating thickness for BSE and SE imaging (Fig. 3.15). For BSE contrast, the SNR always decreased as the coating thickness increased, though the decrease was slower for higher energies. For landing energies of 3.0, 2.0 and 1.5 keV, the initial slopes were about 15, 25 and 40% per nm, respectively. At the minimum film thickness needed for complete discharging during BSE imaging (~1 nm), SNR was reduced by about 25% for a landing energy of 2 keV (Fig. 3.15b, left panel), which compares favorably with the >70% decrease during low-vacuum operation (Fig. 3.7a) in case of the retina sample for which a gas pressure of 50–60 Pa was required.

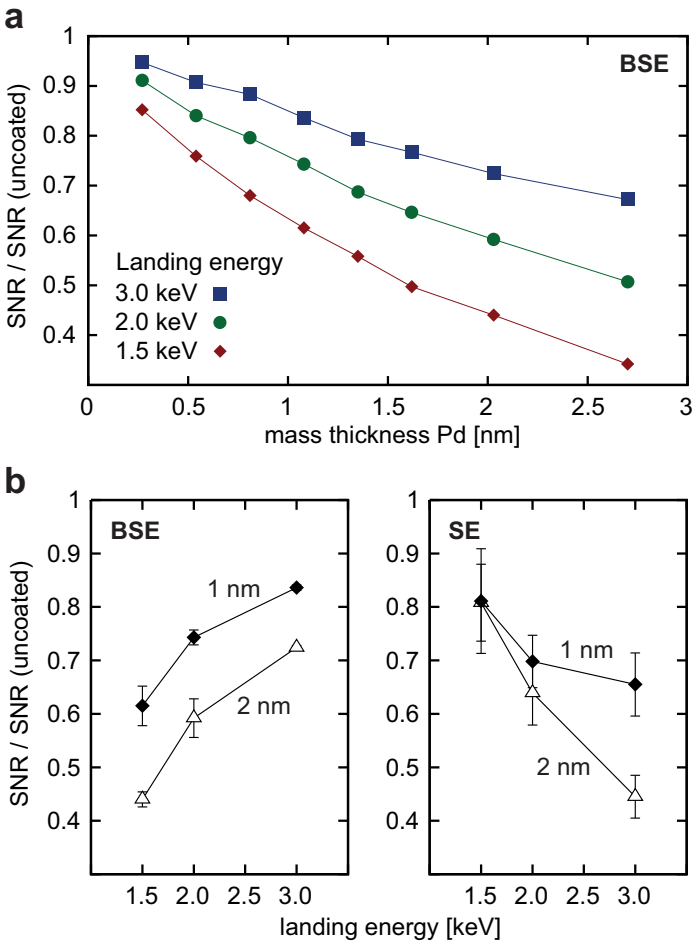

Fig. 3.15: (a) Relative SNR as a function of film thickness for different landing energies. Each data point is an average of three separate measurements from retina neuropil (imaging parameters: 3 keV, 80 pA; 2 keV, 90 pA; 1.5 keV, 140 pA; dwell times 4 µs; working distance 5.5 mm). (b) Relative SNR as a function of landing energy for coating thicknesses of 1 and 2 nm, for BSE (left) and SE (right) contrast. Each data point is an average of three (BSE) or five (SE) measurements (imaging parameters as above, but 8 µs dwell time), error bars show standard deviations. All images were acquired on the FEI Quanta.

For SE imaging, the SNR loss compared to imaging without coating was largest for high landing energies (Fig. 3.15b, right panel), which may be related to the fact that loss of energy caused by the film increases the SE yield for BSEs. This becomes more effective for lower primary energies because there the BSEs lose more energy in the film and the dependence of the SE yield on energy is steeper. This may also explain why at 1.5 keV increasing the coating thickness from 1 nm to 2 nm did not further reduce the SNR for SE imaging.

In-lens (SE) and BSE detection (S11141 photo diode, Hamamatsu Photonics, Hamamatsu, Japan, combined with custom-designed amplifier) were compared in a Zeiss ULTRA PLUS microscope. For fast imaging (10 MHz), I found that the in-lens detector provided a better SNR up to about 1.75 keV beam energy (Fig. 3.16).

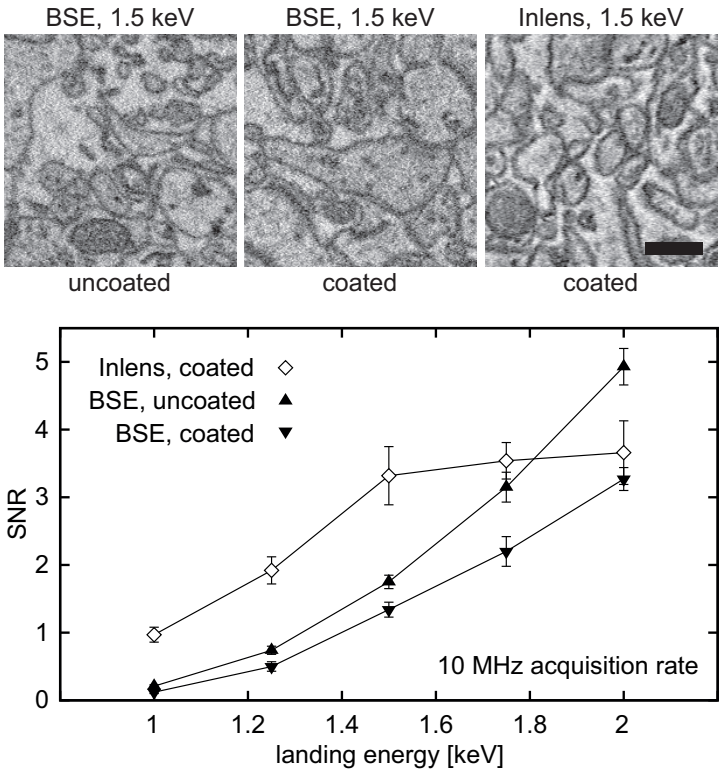

Fig. 3.16: Comparison of SNR for in-lens SE and BSE detection on the Zeiss ULTRA PLUS. Zebra finch brain, beam current ~1 nA, dwell time 100 ns. Each data point is an average of seven measurements from zebra finch neuropil, error bars show standard deviations. Scale bar: 500 nm.

An analysis of the dark current noise of the BSE detector (data not shown) revealed that this was due to the fact that at low electron energies and high scan rates the dark current noise was the dominant noise component for the BSE detector. The observation that the ratio between the SNRs for the coated and uncoated sample is smaller (about 25% at 1.5 keV) under these conditions than when scanning more slowly (close to 50%, Fig. 3.15a) may be explained by a larger relative contribution of shot noise in the slow-scanning case (<1 MHz), which would be increased through coating.

3.2.6 Beam deceleration

Applying a negative potential to the sample reduces the landing energy. This improves the BSE signal via several mechanisms (Paden & Nixon, 1968; Frank & Müllerová, 1999; Phifer et al., 2009): (1) The decelerating field accelerates the BSEs in the direction normal to the surface, thereby focusing them into a smaller solid angle, which means BSEs that otherwise would not strike the detector now contribute to the signal. (2) The BSEs strike the detector at a larger energy leading to a larger amplification in a silicon-junction detector. (3) The lower landing energy results in an increased interaction cross-section.

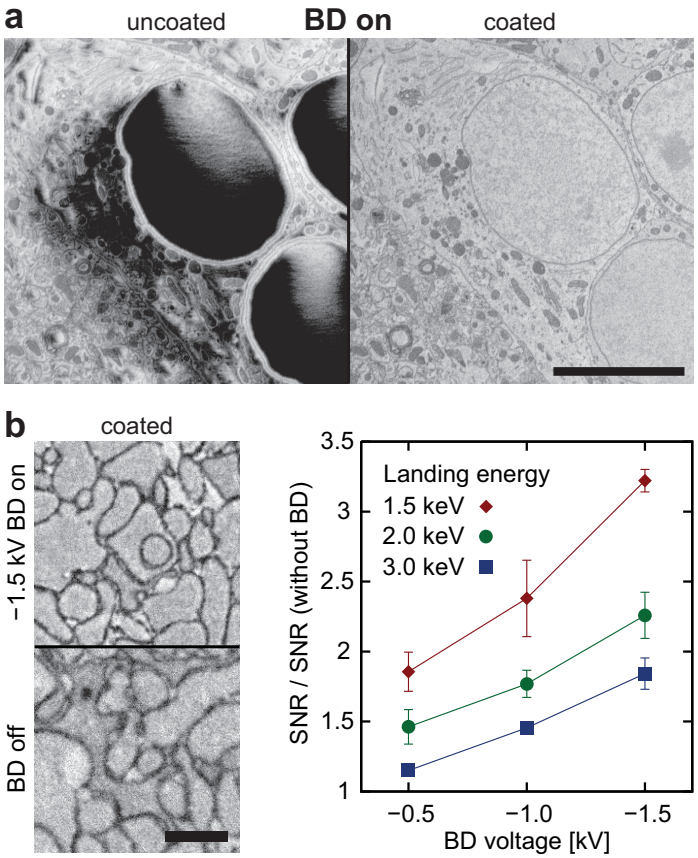

Fig. 3.17: Beam deceleration (BD). (a) Zebra finch sample using BD without (left) and with (right) a ~2 nm palladium film, 1.5 keV landing energy, −1.0 kV beam deceleration, 110 pA beam current, 4 µs dwell time. Scale bar is 5 µm. (b) Coated retina without (bottom) and with (top) −1.5 kV BD, 1.5 keV landing energy, ~120 pA beam current, and 8 µs dwell time. Scale bar is 1 µm. Right panel: SNR relative to that without BD as a function of the deceleration voltage for different landing energies. Each data point is an average of three measurements. Error bars show standard deviations. All images acquired on the FEI Quanta. Scale bars are 5 µm for (a), 500 nm for (b).

The BD method does, however, require that the samples are sufficiently conductive. Many of the epoxy-embedded brain tissue samples that showed no charging-related issues when imaged without BD showed image quality defects, such as local shadowing and uneven signal intensity across the field of view, when BD was applied (Fig. 3.17a, left panel). No such problems occurred when imaging coated specimens with BD (Fig. 3.17a, right panel). Similar to SE imaging, the minimum

coating thickness required for charge neutralization was about 50% larger when a BD voltage was applied to the surface than without BD.

The coatings prevented all charging artifacts during BD imaging, at least for decelerating voltages of up to −1.5 kV, and substantially improved resolution and SNR for a given landing energy (Fig. 3.17b). The improvements were most pronounced for lower landing energies, where BD more than compensated for the decrease in SNR due to coating. Note that part of the gain in SNR is due to better resolution, an effect that is dependent on the microscope: Microscopes that feature an in-column beam acceleration mechanism can preserve focusing quality at lower landing energies (e.g. Zeiss ULTRA PLUS, data not shown). The FEI Quanta lacks such an in-column 'beam-booster', which explains the improvement in resolution when using BD. For a given BD voltage, the beam energy was increased to maintain the same landing energy, resulting in a better focusing quality.

3.2.7 Coating during SBEM stack acquisition

To test whether serial in-chamber specimen coating is reliable, provides consistent contrast over a large number of successive images, and does not interfere with cutting, the coating step and BD functionality (Fig. 3.18b, see also Ohta et al., 2012, for the combination of FIB-SBEM and BD) were integrated into the serial block-face imaging process. Continuous SBEM stacks with automated coating could be acquired with no obvious problems as judged from viewing the reslice (Fig. 3.18a) or inspecting the image sequence (Supporting material, Titze & Denk, 2013). Similar results were obtained using BD or SE contrast (Fig. 3.18b, c). The number of cycles was limited by the displacement range (50 mm) of the automatic rod-advance mechanism.

To estimate the amount of material needed per coating cycle, I assumed that the material is evaporated uniformly in all directions. Although this would appear to underestimate the flux in forward direction, I found that the end of the rod becomes pointed after multiple evaporation cycles, which presumably increases sideways evaporation.

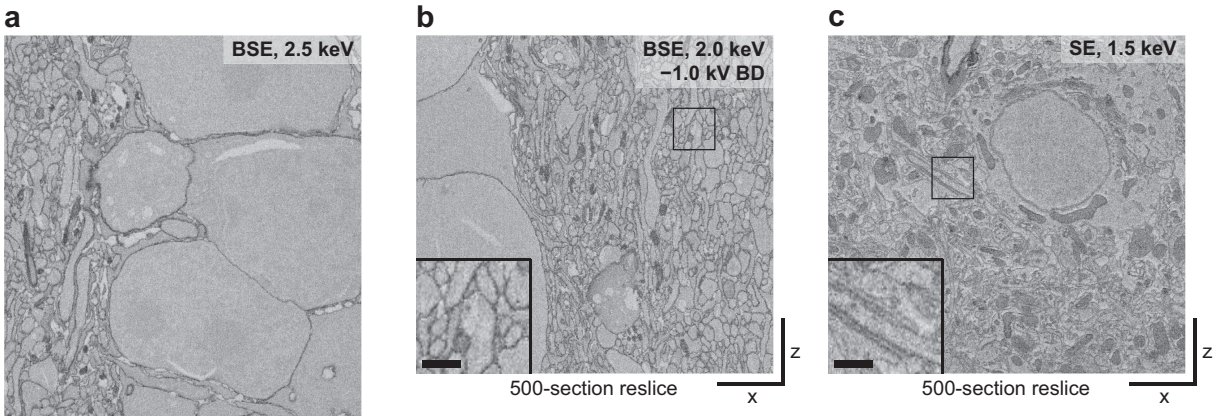

Fig. 3.18: Automated in-chamber coating combined with SBEM. Stacks of rabbit retina using BSE contrast without (a) and with (b) beam deceleration (−1.0 kV), of zebra finch (c) using SE contrast. All stacks acquired on the FEI Quanta using landing energies of 2.5, 2.0 and 1.5 keV (a, b, c), beam currents of 160, 150 and 40 pA (a, b, c), pixel dwell times of 2, 2, and 6 µs (a, b, c), a cutting thickness of 25 nm, and an x-y pixel pitch of 16.5 nm. Scale bars (x-z): 2.5 µm. Scale bars in insets: 500 nm.

The volume of material, V, required for a coating thickness, d, at the sample position can be estimated as the volume of a hollow sphere:

$$V = \frac{4}{3}\pi\left[\left(R + \frac{d}{\sin\alpha}\right)^3 - R^3\right] \approx 4\pi R^2 \frac{d}{\sin\alpha},$$

where α is the angle at which the evaporated atoms strike the sample surface, and R the distance between the tip of the rod and the sample surface. The rod advance per coating cycle is then provided by

$$\Delta = \frac{V}{\pi r^2} = \frac{4dR^2}{r^2 \sin\alpha},$$

which amounts to 74 micrometers for the configuration in the Quanta microscope (R = 65 mm, α = 20°, d = 1.5 nm, and rod radius r = 1 mm). At this rate, a 50-mm-long rod should last for about 675 cycles. Experimentally, I achieved about twice that, which suggests that evaporation is enhanced in the forward direction. Increasing the rod diameter to 3 mm and its length to 100 mm, and reducing the working distance to 46 mm would result in over 10 000 cycles with 1.5 nm film thickness.

About 5 mm of rod length are needed to clamp it, and the last 3–5 mm of the free rod length were found to be unusable, which is presumably due to the combined effect of thermal shunting (see below) and too large a fraction of the heating electrons starting to fall onto the holder instead of the rod.

3.2.8 Debris and other issues

During SBEM stack acquisition with automated coating several issues arise: (1) As the rod shortens, heat is drained more efficiently from the rod, increasing the heating power required to reach a given rate of deposition. (2) Thermal radiation from the tip reaches the sample, possibly heating it. (3) Most of the material evaporated from the tip accumulates on the inside of the evaporator head and needs to be removed after several thousand coatings (Fig. 3.19).

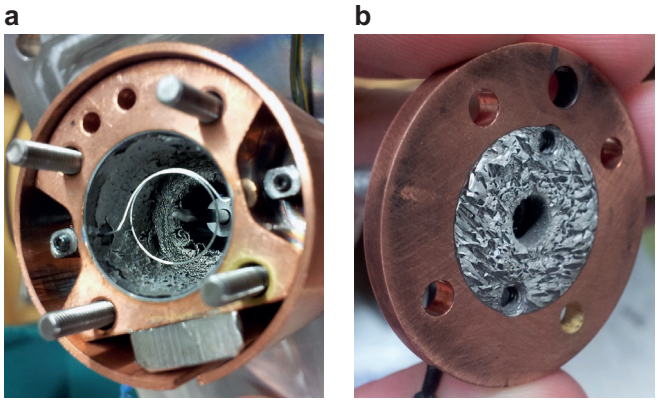

Fig. 3.19: Coating debris (palladium) after more than 1000 coating cycles, inside the evaporator head (a), and on the front plate (b). When cleaning the evaporator head, care has to be taken not to touch the filament, which breaks easily.

The first issue can be dealt with in two ways: Either by accepting that coating intervals become longer as the stack is being acquired, or by adjusting the rod high voltage or the target emission current to increase the heating power, thus keeping coating times constant.

The second issue – thermal radiation – did not appear to cause problems in the case of palladium evaporation. However, if the working distance is decreased to enable more coatings per rod length, as suggested above, the heating power reaching the sample will increase with the inverse square of the distance. An even steeper dependence is to be expected for the evaporation temperature (radiated power $P \propto T^4$) – a disadvantage when using carbon or other coating materials requiring high evaporation temperatures. Should problems caused by thermal radiation be

observed for cutting, one solution may be to prolong the waiting intervals between coating and cutting, which would, however, increase overall SBEM acquisition time.

The third issue – debris – is caused by the fact that only a tiny fraction of the evaporated material is actually deposited onto the sample. The rest is deposited as thick layers onto the inner surfaces of the aperture tube and the evaporator head (Fig. 3.19). In the Quanta setup, the distance between the rod tip and the closest evaporator head surface is only about 1/7 of the distance between the rod tip and the sample surface. Hence, for each nanometer deposited on the sample surface, about 50 nanometers are deposited on the copper surfaces surrounding rod and filament.

Palladium debris appears to stick well to the metal surfaces and its thick layers are fairly rigid. In comparison, thick layers of deposited chromium and carbon are much more brittle and come off as flakes more easily. Whereas chromium has caused several instances of high-voltage arcing and filament short circuits after hundreds of evaporation cycles because chromium flakes touched the filament or the rod, no such problems have been observed for palladium.

3.3 New evaporator head

Filament degradation caused by carbon bombardment (section 3.2.2) and the problem of debris accumulation discussed in section 3.2.8 prompted the development of a new evaporator head. The new design, which I will present in this section, aims to achieve the following: (1) Carbon evaporation over hundreds or potentially thousands of successive coating cycles; (2) More efficient use of coating material (less debris per coating); (3) Easier cleaning of the evaporator head.

3.3.1 Simulations and new design

In the original e^--flux evaporator head, the rod tip is in line of sight of the filament from where electrons are emitted. Since evaporation from the rod tip occurs in all directions, the filament is bombarded with evaporated atoms during every coating cycle. Hence, a new design appeared suitable in which the electrons emitted from the filament follow curved trajectories around a physical barrier that protects the filament from bombardment with coating material.

I simulated different designs incorporating deflection grids and electrodes, with the ion optics simulation program SIMION (Scientific Instrument Services, Ringoes, NJ, USA). Small deflection voltages (<50 V) appeared sufficient to deflect the electrons towards the rod. This, however, did not take into account space-charge effects, which could not be simulated with SIMION. I therefore used the software CPO (Charge Particle Optics Ltd., Manchester, UK; Read & Bowring, 2011) that allowed to adequately model thermionic emission and space-charge effects (Read & Bowring, 2004). A design that seemed to fulfill the requirements (filament not in line of sight; achievable emission currents high enough for carbon evaporation, >65 mA) is shown in Fig. 3.20b.

The simulation of the new design predicted that the emitted electrons would be directed onto a smaller area on the rod surface, compared to the original e^--flux design (Fig. 3.20a). This may be an advantage for two reasons: (1) Sideways evaporation may be reduced and forward evaporation increased, which would lead to a more efficient use of coating material; (2) A higher electron flux density at the tip of the rod may reduce the emission current required to achieve a given evaporation temperature.

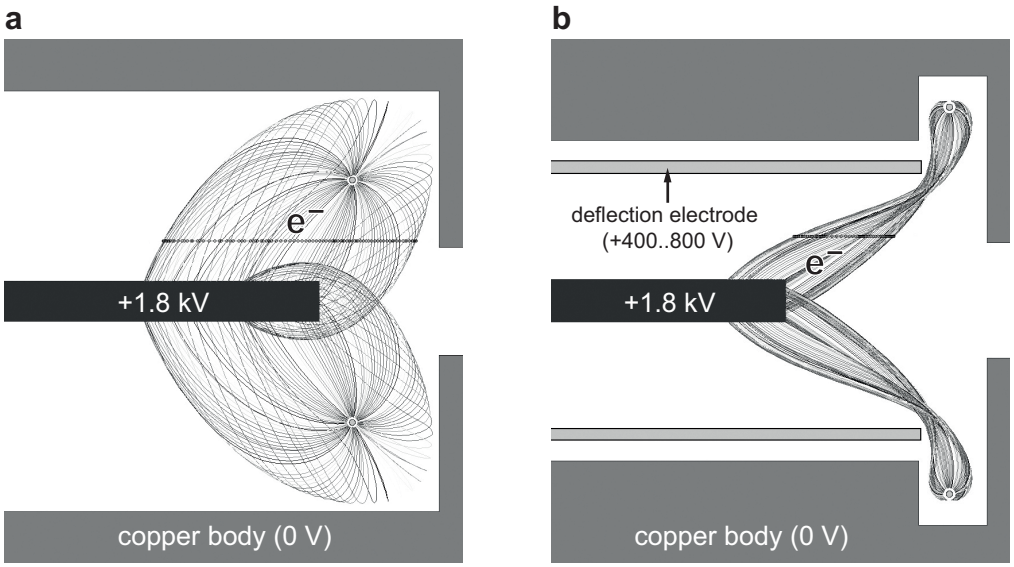

Fig. 3.20: Old (a) and new (b) evaporator head design in cross-section (radially symmetric), simulated with the CPO software. (a) Line-of-sight evaporation. (b) New design. A cylindrical deflection electrode (set to 600 V in the simulation shown) is positioned around the rod. Electrons emitted from the filament are first attracted by the electric field of the deflection electrode, then also by the field of the rod. The filament is hidden from bombardment by evaporated atoms.

A new evaporator head, based on the design shown in Fig. 3.20b, was built in-house (Fig. 3.21). The deflection cylinder was initially made of stainless steel. During the first evaporation tests, electrons emitted from the filament hit the rim of the cylinder, which heated up and began to deform. The material was therefore changed to molybdenum and the cylinder was produced by a contract manufacturer (Length: 47.5 mm; inner diameter 12 mm; PLM GmbH & Co. KG, Neuhausen, Germany).

To insulate the molybdenum cylinder (set to several hundreds of volts during operation) from the outer copper walls (grounded), a ceramic tube (Al_2O_3; length: 30 mm, inner diameter 13 mm, outer diameter 15 mm; Ceratec GmbH, Kreuztal-Kredenbach, Germany) was inserted between the electrode and the copper body (Fig. 3.21a).

The molybdenum cylinder was connected to a high voltage power supply through a high-vacuum feedthrough. To ensure a reproducible position of the cylinder (which CPO simulations showed to be crucial), the pin that connected the cylinder to the high voltage also served to fix its position (Fig. 3.21a). A total of 10 holes along the circumference of the cylinder allowed adjustment of its position along the evaporator axis in 0.1-mm steps.

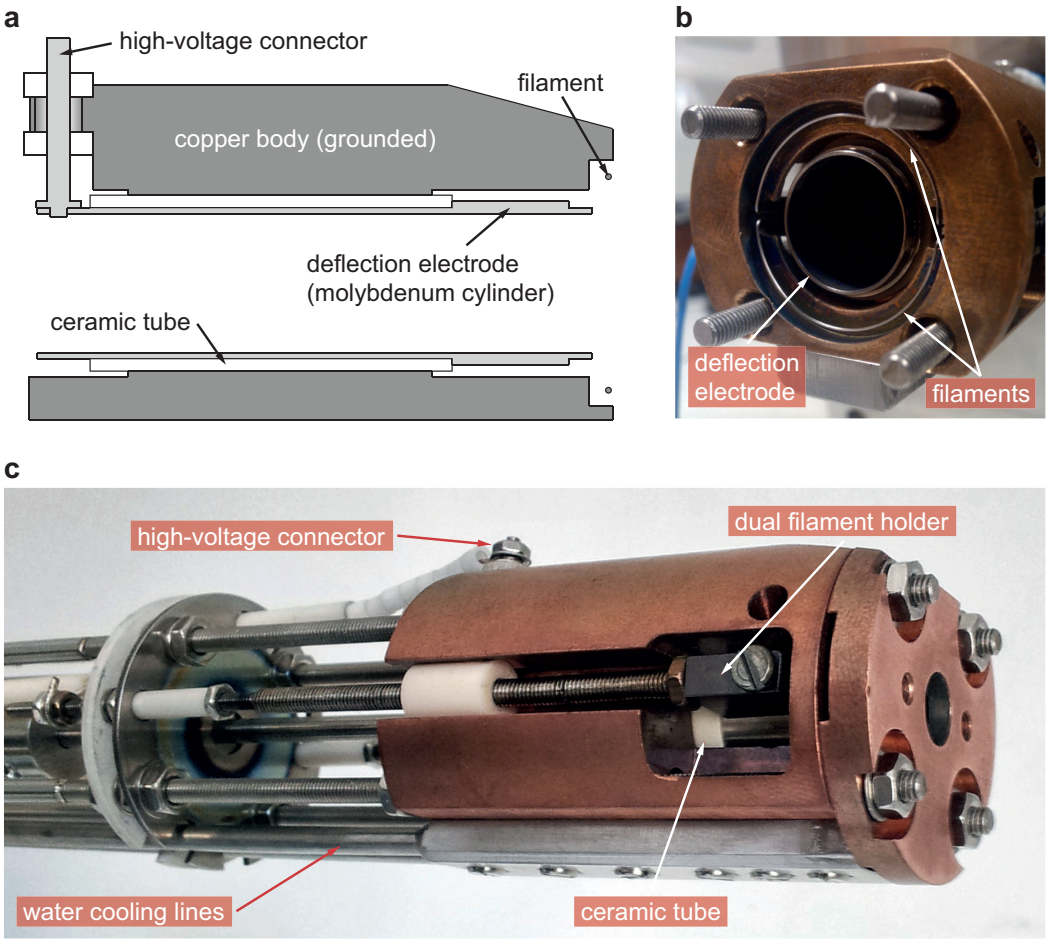

Fig. 3.21: New evaporator head. (a) Cross-section. (b) Front view, front plate detached, showing the two filaments. (c) Full view (aperture tube detached).

Since the new design, as simulated with CPO, required the filament to be precisely positioned and radially symmetric, new filament holders had to be developed. Instead of holding one filament (1.5 turns) as in the original e^--flux head, the new holders hold two filaments (½ turn each, identical shape, ⌀ 17 mm), as shown in Fig. 3.21b. This new configuration ensures that all electrons are emitted from the same

plane. A small tool was designed to bend the filaments (tungsten wire, ⌀ 0.3 mm; Goodfellow, Bad Nauheim, Germany) into reproducible half-circle shapes. The filaments were connected in parallel, which required a new power supply that could deliver twice the current (EA-PS 816-20R, EA Elektro-Automatik, Viersen, Germany).

Initial testing of the new evaporator head with carbon, chromium and palladium was carried out in the external vacuum chamber of a BAL-TEC MED 020 coater (Leica, Wetzlar, Germany) using a custom-made flange to mount the e^--flux.

3.3.2 Preliminary results

When both filaments were heated with 7–8 A each, and the rod set to a high voltage of 1.8 kV or higher, no emission current was detected while the deflection voltage was kept at zero, suggesting that line of sight is effectively blocked between the rod and the filaments. Since the evaporated atoms travel in straight lines, the filament should therefore be protected from bombardment.

As the deflection voltage was increased to about 100 V, a small emission current was measured (<10 mA). The deflection voltage was further increased until a maximum emission current was reached (~70–80 mA for carbon evaporation, at a filament current of 8 A; rod high voltage: 1.8 kV, deflection voltage: 700 V). A fraction of the emitted electrons (up to ~30% of the total emission current) did not reach the rod, but instead hit the deflection electrode, thereby heating it.

For a given filament current, the magnitudes of the emission current reaching the rod and of the emission current lost through the deflection electrode depend on the positions of the filaments, of the rod tip, and of the deflection electrode. An optimization of these positions will be required to maximize the current reaching the rod and minimize the current falling onto the deflection electrode.

Both palladium and chromium were evaporated successfully with the new evaporator head. Carbon evaporation was also possible (deposition confirmed with a quartz crystal thickness measurement), but there were two problems that prevented long coating series with carbon: (1) High-voltage arcing occurred again, as in the original e^--flux evaporator head. (2) The deflection electrode is heated during evaporation by electron bombardment (up to 30 mA × 700 V = 21 W). A heat sink attached to the deflection electrode may be required for heat dissipation.

Whether the new design can improve evaporation efficiency will be determined by comparing long coating series. A comparison of 1000 successive 1-nm coatings using the original e^--flux evaporator head with 1000 successive 1-nm coatings using the new evaporator head will show whether the new design can provide more coatings per rod length.

3.4 Summary and discussion

Automated in-chamber specimen coating provides reliable charge elimination for SBEM imaging. Compared with the widely used low-vacuum method, a ~1–2 nm film of palladium leads to a better SNR for BSE imaging in high vacuum under typical imaging conditions (2 keV, 150 pA). In-chamber coating also permits SE imaging of non-conductive samples with both ET and in-lens detectors, as well as the application of beam deceleration to such samples. The coatings completely and reliably remove any charging artifacts – for single images as well as SBEM image stacks. Coating the specimens inside the chamber can be advantageous for taking images of a single surface, for example when oxidation of deposited films needs to be prevented.

Once a specimen is coated with a conductive material at sufficient thickness (~1.5–2 nm for palladium and chromium), very high primary beam currents (>20 nA) can be used without charging effects, which is important for large-scale image acquisition projects, where fast pixel rates are required. In-chamber conductive coating may also be essential for the combination of multibeam SEM (Schalek et al., 2012), which is based on SE contrast, with SBEM.

One drawback of charge elimination via thin conductive coatings is that both beam and signal electrons have to traverse the deposited film, which reduces SNR by generating BSEs in the film that carry no information about the sample and reducing the number and energy of electrons that do carry information about the sample. The reduction in energy reduces the number of electrons generated in the detector diode, thereby depressing contrast, especially at low landing energies. Since the use of beam deceleration increases the energy of all BSEs before they reach the detector, the loss of SNR due to coating can be compensated. When using SE contrast, the fact that the SE yield increases as the electron energy falls favors lower landing energies.

Although lighter metals with a lower nuclear charge would presumably reduce SNR less, the current setup is limited to materials that can be evaporated at a sufficiently high rate before they melt in an uncontrollable fashion (which rules out aluminium, gold, platinum and others) and to those that do not react with the diamond knife (which rules out iron, cobalt, nickel, titanium and others). Using FIB-SBEM would remove the second restriction. A different evaporator design or the use of (ion beam) sputtering would remove the first restriction, in which case light metals (for BSE imaging) and other suitable metals with high SE yields (for SE imaging) might be used.

In addition to SBEM imaging of neural tissue, which has been the focus so far, the use of automated in-chamber specimen coating could also be extended to other applications, for example 3-D material analysis of non-conducting specimens. Since the use of carbon coating is recommended for X-ray microanalysis (Echlin, 2009, Ch. 11), automated in-chamber carbon coating using the new evaporator head could be of interest for a potential combination of X-ray microanalysis with SBEM.

The most severe current limitation of automated in-chamber specimen coating is the number of coating cycles (<1500) that can be performed before the rod is used up. In section 3.2.7, a few approaches were suggested (thicker rod, longer feed, and shorter working distance) that would allow 10,000 cycles under the assumption that the amount of debris inside the evaporator head does not prevent reliable operation. If higher efficiency can be achieved with the new evaporator head (section 3.3), less volume may be required per coating cycle, alleviating the debris problem.

Another issue that deserves a closer look is the required time for a single coating. The total acquisition time of a SBEM stack is mainly determined by the cutting time, the imaging time, and the overhead for tiling (stage movements). For single-tile stacks, the imaging time is usually very short (<10 s for typical stack acquisitions on the FEI Quanta). Assuming a cutting time of 40–60 s, the coating time (typically 20–40 s for palladium) will make up a sizeable fraction of the total acquisition time. For very large surfaces, however, where the imaging time dominates the total acquisition time and additional time is required for tiling, coating will be more time-effective, as the time per coating is independent of the size of the area being coated.

A reduction in coating time could be achieved as follows. (1) Higher emission currents could be used to obtain higher deposition rates. In the case of palladium, however, the room for improvement is limited, as the rod tip will begin to melt at

higher temperatures. (2) The acquisition script could be improved. Currently, the script used for SBEM acquisition with automated coating initiates the coating step directly after the cut cycle is finished. However, when the filament current is ramped up at the beginning of the coating cycle, it takes up to 10 seconds until evaporation begins. This ramp-up could already be performed during the last 10 seconds of the cutting cycle. (3) Use of a shutter would further reduce coating time. The shutter would not be opened until the maximum deposition rate is reached, as determined by measuring the ion current. Coating would then begin at the full deposition rate directly after the knife is moved away from the sample. In addition, closing the shutter after the desired coating thickness has been reached may also prevent the afterglow of the rod from affecting the BSE signal, thus allowing BSE imaging to commence earlier.

4 Cryo-SBEM

For consistent cutting in diamond-knife SBEM, the amount of electron irradiation must not exceed certain thresholds for a given cutting thickness (see section 4.1.2 below; for other parameters that affect cutting see section 1.4.1). Since lowering the sample temperature is known to reduce the effects of beam damage in TEM imaging (section 1.4.2), cryo-operation appears to be worthwhile exploring for SBEM as well: In addition to possibly making the sample more rigid, which is known to improve cutting from the use of harder embedding materials, cryogenic temperatures may reduce the effects of electron beam damage, thus enabling thin cutting at higher electron doses than those achievable at room temperature.

In this chapter, I will describe the work that has been carried out so far to allow SBEM operation at ~100 K (–173 °C). The entire setup – consisting of a closed-cycle cooling system, a SBEM microtome with custom-developed cryo-holders for the knife and the sample, and the SEM itself – is referred to as 'Cryo-SBEM' in the following text. I will present observations made during low-temperature SBEM operation, discuss remaining problems with the current setup, and outline the next steps for experimental quantification of potential improvements.

4.1 Effects of beam damage on imaging and cutting

The electron beam in an SEM inflicts structural damage on the specimen being imaged (Egerton et al., 2004, see section 1.4.2). In the following, I will briefly describe how the effects of such damage can be observed directly in SEM images and indirectly in the case of SBEM imaging, and how the effects can be quantified.

4.1.1 Observation of beam damage effects in SEM images

The effects of electron beam damage can be seen directly in SEM images: When a certain region on the sample surface is imaged repeatedly, contrast is increased at first, and then substantially reduced if irradiation continues (Fig. 4.1d). The initial increase is presumably caused by removal of epoxy resin while the stained tissue remains mostly intact; the subsequent decrease is presumably caused by structural damage of both the epoxy resin and the stained tissue. Such changes in contrast are

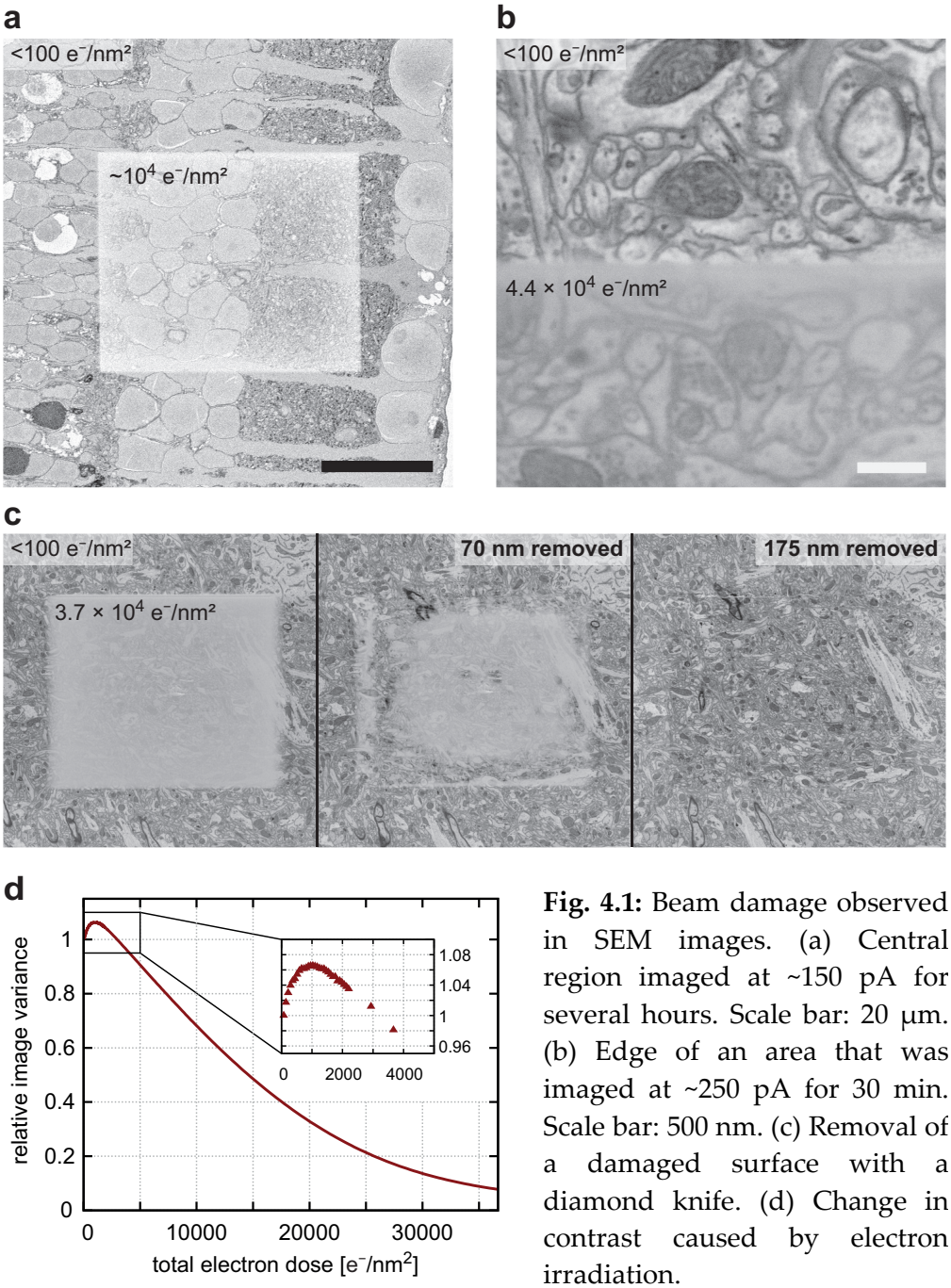

Fig. 4.1: Beam damage observed in SEM images. (a) Central region imaged at ~150 pA for several hours. Scale bar: 20 µm. (b) Edge of an area that was imaged at ~250 pA for 30 min. Scale bar: 500 nm. (c) Removal of a damaged surface with a diamond knife. (d) Change in contrast caused by electron irradiation.

encountered during regular imaging when a region has been imaged multiple times (for example during focusing) and the magnification setting is switched to a lower value (Fig. 4.1a). At higher magnification, a loss of image detail in heavily irradiated regions can also be observed (Fig. 4.1b).

After the region shown in Fig. 4.1c had been irradiated for an extended period of time (total dose of >30000 e^-/nm^2) and appeared 'bleached', several cuts with a diamond knife were needed until the visible damage was removed. A further removal of several hundreds of nanometers in cutting thickness was necessary until all cutting artifacts on the irradiated region subsided (data not shown).

During the acquisition of SBEM stacks, sample surfaces are usually imaged only once before they are removed with the diamond knife. Typical pixel dwell times are between 2 and 8 µs on the FEI Quanta (typical beam currents up to 300 pA) and 100–500 ns on the ZEISS Ultaplus (currents up to several nA), which yields electron doses well below 100 e^-/nm^2 for pixel sizes of 10–20 nm. Under such imaging conditions, effects of beam damage are usually not visible in the images (see the electron-dose values in Fig. 4.1d for comparison). However, the structural damage inflicted by the electron beam can be observed indirectly: When the electron dose becomes too high, consistent cutting is no longer possible (see next section).

4.1.2 Electron-dose limits for consistent SBEM cutting

To compare the effects of beam damage on cutting under different imaging conditions, we need a parameter that corresponds to the amount of damage caused by the electron beam. If the landing energy of the electron beam is kept constant for comparison purposes, the electron dose (units: number of electrons per nm^2) is a suitable choice:

$$D_\mathrm{e} = \frac{(I_\mathrm{P}/\mathrm{e})\tau_\mathrm{D}}{A_{xy}}$$

(I_P: primary electron beam current; e: electron charge; τ_D: pixel dwell time; A_{xy}: sample surface area corresponding to one pixel in the SEM image.)

Multiplying the electron dose D_e with the kinetic energy of one beam electron (eV_e) provides an upper limit for the amount of energy that the beam can transfer to the sample, per square nanometer sample surface:

$$D_E = \frac{I_P V_e \tau_D}{A_{xy}}$$

To determine the electron-dose limits for SBEM imaging in the case of an epoxy-embedded retina sample (see Appendix B for details), I compared 40-nm and 25-nm cutting under high vacuum conditions at 3.0 keV and 2.5 keV landing energy, respectively.

For a cutting thickness of 40 nm, I found that an electron dose as high as 28 e^-/nm^2 (D_E = 84 keV/nm²) was tolerable for consistent cutting (300 pA beam current, 4 µs dwell time, 16.5 nm pixel size, 3 keV landing energy).

For a cutting thickness of 25 nm, consistent cutting was only possible for a much lower electron dose of D_e = 7.3 e^-/nm^2 (D_E = 18 keV/nm²), 160 pA beam current, 2 µs dwell time, 16.5 nm pixel size, 2.5 keV landing energy). When increasing the dose to about 10–12 e^-/nm^2, the cutting thickness became non-uniform; at 15 e^-/nm^2, cuts were always skipped. Changes in electron dose often translated into changes in cutting behavior within a few cutting cycles.

D_e = 10 e^-/nm^2 was the electron dose used in Briggman et al. (2011) to acquire a large SBEM dataset (350 × 300 × 60 µm³) of a similar type of retina sample at 23 nm cutting thickness. However, low vacuum conditions (50 Pa water vapor) were used in that case, which presumably reduced the effective electron dose.

Until recently, a diamond-knife cutting thickness of about 20–25 nm was considered the lower limit for SBEM imaging. Recent experiments have shown that cutting thicknesses of 15 nm and below are possible if the landing energy and the electron dose are reduced, and if more beam-damage-resistant epoxy resins are used for embedding (Mancuso, 2012; Sarah Mikula, personal communication).

The challenge now is to enable thin cutting – down to the physical limits for cutting with a diamond knife – for higher electron doses than those achievable so far. Cryo-SBEM is an attempt to overcome the current dose restrictions. If successful, this will allow diamond-knife SBEM to compete with FIB-SBEM for the acquisition of datasets with both high isotropic resolution and high SNR, surpassing it in terms of FOV.

4.2 Cryo-SBEM setup

4.2.1 Closed-cycle cooling system

A closed-cycle cooling system ("Cryotiger", Polycold Systems/Brooks Automation, Petaluma, CA, USA) was used to cool both sample and knife. The system provides continuous cooling without requiring the user to handle any liquid or gas, or to carry out any other maintenance tasks. The Cryotiger's functional principle is similar to that of a refrigerator.

The Cryotiger system consists of a compressor, two gas lines (one supply line and one return line; braided stainless steel to withstand the operating pressure of 14–17 bar), and a cold end with a circular surface where the heat loads are attached (Fig. 4.2). The refrigerant used for the Cryo-SBEM setup was the proprietary gas blend 'PT-13' (Polycold Systems), with which a final cold end temperature of 73 K (–200 °C) was reached.

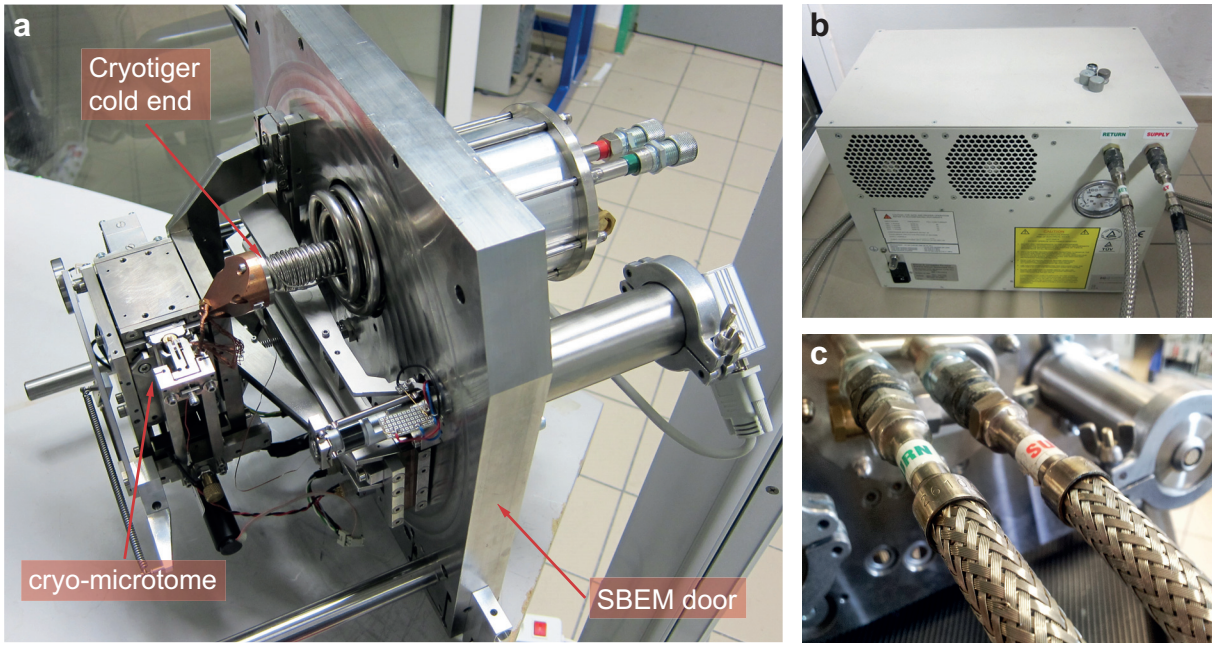

Fig. 4.2: Cryo-SBEM setup. (a) SBEM door with the custom-developed cryo-microtome (built by the mechanical workshop in-house) and the Cryotiger cold end (held in position by a custom-made high-vacuum flange). (b) Cryotiger compressor. (c) High-pressure cooling lines (total length: 10 m), carrying the refrigerant PT-13.

The Cryotiger cold end was integrated into the SBEM door with a custom-built flange (Fig. 4.2a). A large piece of copper (called 'copper cold end' in the following text) was screwed to the Cryotiger cold end to serve as a connection point for the sample holder and the knife holder, and as a buffer against temperature fluctuations. OFHC (Oxygen-Free High Thermal Conductivity) copper braids (Janis Research, Wilmington, MA, USA) were attached to the copper cold end in order to connect it to the two heat loads of the setup – the sample holder and the knife holder. All Cryo-SBEM experiments were carried out in an FEI Quanta FEG 200 SEM.

4.2.2 Modifications for low-temperature SBEM operation

New custom-developed holders for the diamond knife and the sample provided insulation for low-temperature SBEM operation. These 'cryo-holders' were each connected with a copper braid to the copper cold end (Fig. 4.3a). The ends of the braids were soldered into 3-mm-diameter copper cylinders (6 mm length each). To connect the sample holder to the copper braid, the copper cylinder at the end of the braid was inserted into a hole at the side of the sample holder (Fig. 4.3b) and secured with a grub screw. The other three cylinder end pieces were soldered into custom-made copper blocks that were screwed onto the knife holder and the copper cold end, respectively. To maximize thermal conduction between all contact surfaces, silicone-free cryogenic high-vacuum grease (Apiezon N Grease, M&I Materials Limited, Manchester, UK) was used.

The cryo-sample-holder and the cryo-knife-holder were thermally insulated from the rest of the microtome with 2-mm-diameter glass spheres (Fig. 4.3a). The part of the knife holder that clamps the diamond knife is pushed against three glass spheres. The force holding this part in place is exerted by a screw whose head pushes against a small beam that is insulated with two additional glass spheres, giving a total of five contact points with glass-sphere insulation. The sample holder is secured by five glass spheres: one sphere on the side facing the knife arm, four spheres on the opposite side. The position of each of the four spheres on the opposite side can be adjusted with a set screw. The other sphere is held by a larger screw that is used for final positioning and fastening of the sample holder at the desired working distance. The two main screws of the cryo-knife-holder and the cryo-sample-holder each compress a spring that continues to provide a pushing force against the glass spheres when the temperature is lowered and all parts contract (see section 4.3.2).

To measure the temperatures of the copper cold end, the cryo-knife-holder, and the cryo-sample-holder in the vacuum chamber, resistance temperature detectors (RTDs) were used (XP-1K/XP-100 platinum RTDs, Cryogenic Control Systems, Rancho Santa Fe, CA, USA). Each RTD sensor was connected via a 4-lead phosphor-bronze ribbon cable with low thermal conductivity (PW4-36-100, Cryogenic Control Systems) to a LEMO vacuum-feedthrough connector. The temperatures were recorded with a temperature controller (Model 34, Cryogenic Control Systems), using four-terminal sensing.

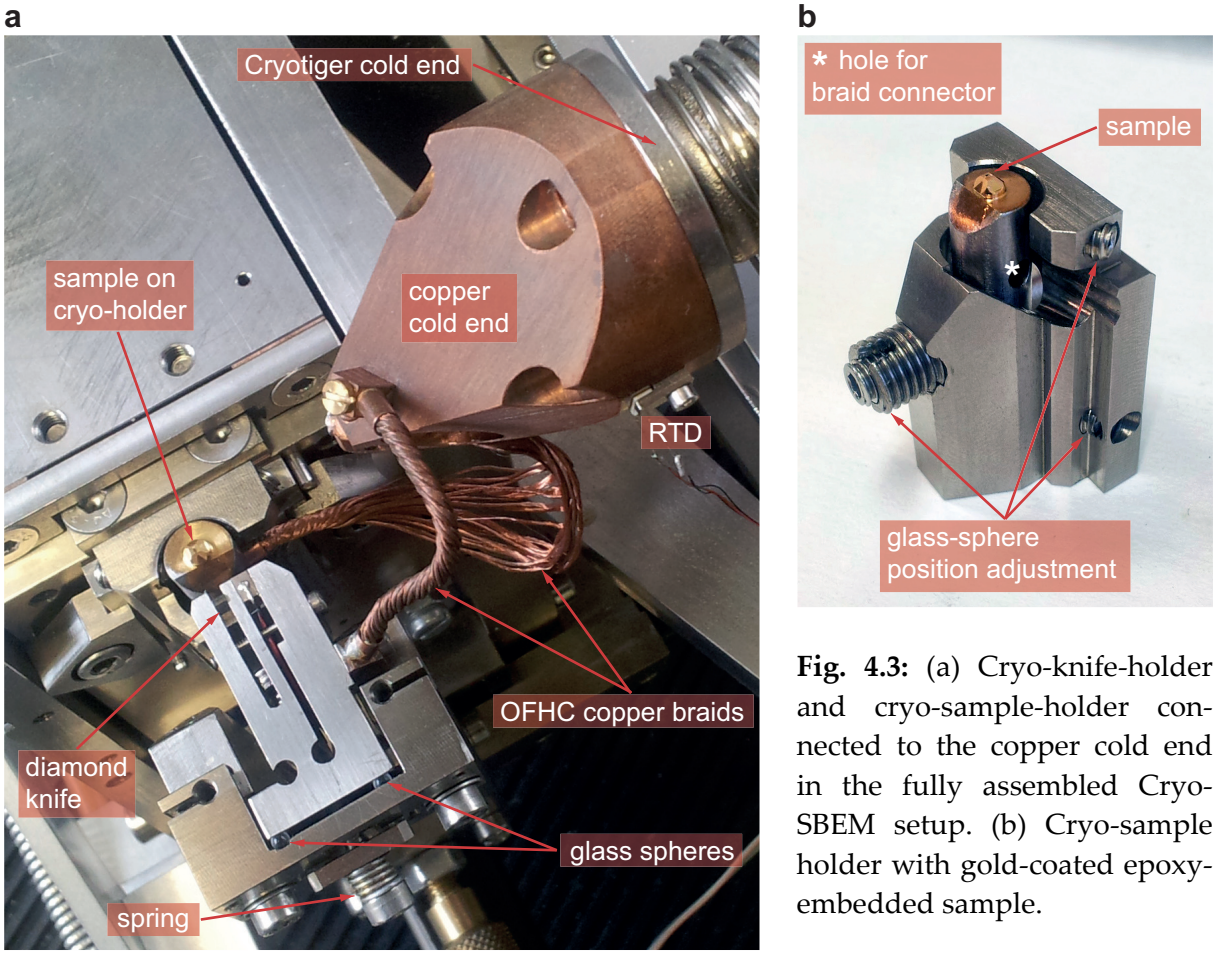

Fig. 4.3: (a) Cryo-knife-holder and cryo-sample-holder connected to the copper cold end in the fully assembled Cryo-SBEM setup. (b) Cryo-sample holder with gold-coated epoxy-embedded sample.

Both the cryo-sample-holder and the cryo-knife-holder were made of titanium. Earlier versions of the sample holder were made of copper and brass, but these materials proved too soft – the glass spheres caused large indentations. In addition to its hardness, another advantage of titanium is its smaller expansion coefficent (titanium: 8.6×10^{-6}/K; copper: 16.5×10^{-6}/K; brass: $18.7–20.3 \times 10^{-6}$/K; Lide, 2005), which shortens the knife approach distance at low temperatures (see section 4.3.2).

Mechanical stability of the cryo-knife-holder and the cryo-sample-holder was verified by cutting tests at room temperature. At low temperatures, full verification of mechanical stability could not be achieved yet (see section 4.3.3). Since knife holder and sample holder contract when cooled down, the forces acting on them to secure their positions may decrease. Hence, stability at low temperatures does not automatically follow from stability at room temperature.

4.3 Results

4.3.1 Temperature measurements

First, I carried out temperature measurements to determine the final temperatures that the sample and the knife can be cooled to with the setup (Fig. 4.4). The copper cold end always reached a final temperature of 73 K, the sample holder reached about 100 K, and the knife holder around 110 K. Final temperatures depended on the thickness (~2 mm for most tests) and the length (35–70 mm) of the copper braids used, and also on the quality of thermal conduction at the contact surfaces.

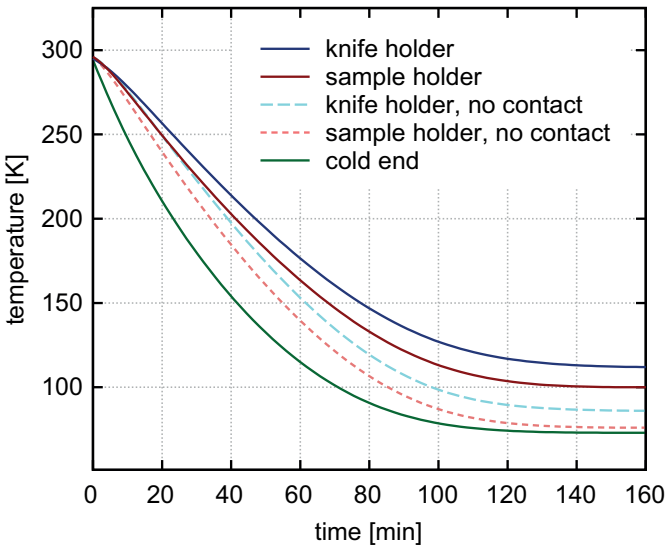

Fig. 4.4: RTD temperature measurements during Cryotiger operation. Compressor was switched on at t = 0 min. Final temperatures were reached after about 2½ h. Final cold end temperature was 73 K. Knife holder and sample holder temperatures were measured when secured inside the microtome (two upper curves, final temperatures: 112 K, 100 K) and when suspended in high vacuum (no microtome contact, final temperatures: 86 K, 76 K).

To determine by how much the final temperatures of the knife holder and the sample holder are reduced through their contact to the microtome via the glass spheres used for insulation, I measured the final temperatures of sample holder and knife holder when they were suspended in high vacuum, with no contact to anything except the

copper braids. In this configuration, the final sample holder temperature was 24 K lower than in the case when it was attached to the microtome; the final knife holder temperature was 26 K lower. The temperature difference is almost identical, which is not surprising, since both sample holder and knife holder are 'heated' by five glass-sphere contact points each.

As shown in the temperature plot above, the final temperature of the knife holder was higher than the final temperature of the sample holder, even though the braid used to connect the sample holder was almost twice as long. Heating caused by radiation from the microtome surfaces and the chamber walls may explain this temperature gap, since the knife holder has a larger surface area.

4.3.2 Low-temperature effects

High vacuum conditions in the FEI Quanta's vacuum chamber were necessary to operate the Cryo-SBEM, since low-vacuum conditions (e.g. nitrogen at 50 Pa, which was tested) prohibited adequate thermal insulation.

When the sample was cooled down in high vacuum to its final temperature of 100–110 K, the first observation was that the sample was covered by a continuously thickening layer of ice. This layer is formed by residual water molecules in the vacuum chamber that freeze when they hit the cold sample surface. (The temperature of the sample surface is too high to freeze nitrogen, oxygen or noble gases.) When cut off by the diamond knife, the layer quickly formed again, reducing image contrast and eventually completely covering the sample (Fig. 4.5).

Assuming that every water molecule striking the cold sample surface contributes to the ice layer and that the gas composition in high vacuum is dominated by water, we can obtain a lower estimate for the time it takes to form a monolayer (derived from the molecular flux density $\frac{1}{4}n\bar{v}$):

$$\Delta t = \frac{4}{n\bar{v}{d_\mathrm{m}}^2}$$

For a molecular density n = 4.1 × 10^{-8} mol/m^3 at a pressure of 10^{-4} Pa and T = 20 °C, average molecule velocity at room temperature $\bar{v}$ = 637 m/s, van-der-Waals diameter d_m = 0.28 nm of water (Franks, 2000), we find Δt = 3.2 s (~18 monolayers/min).

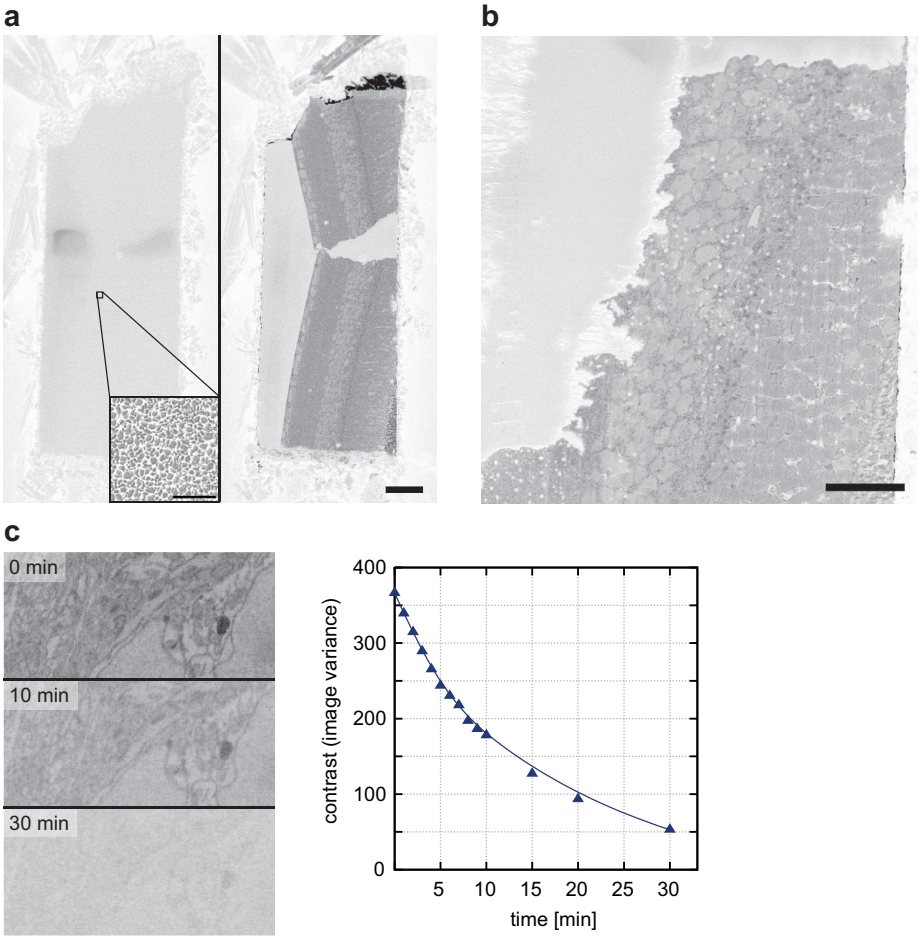

Fig. 4.5: (a) Left: Sample surface completely covered with ice. Scale bar in inset: 5 μm. Right: Sample surface revealed after cut. Scale bar: 50 μm. (b) A thick layer of ice that built up over more than 24 h, partially cut off with the diamond knife. Scale bar: 25 μm. (c) Image contrast is reduced by the ice layer forming on the surface.

When the Cryo-SBEM setup was tested in a different FEI Quanta microscope, the effect was substantially reduced (factor of ~20): about an hour had to pass until a visible reduction in contrast could be observed. It is currently unclear how this different rate can be explained. According to FEI, the high vacuum gas composition in the microscope is dominated by water. In the microscope where the much lower rate of ice layer formation was measured, the cold end and other parts at cryogenic temperatures may have sufficiently reduced the amount of residual water in the chamber, while in the other vacuum chamber this reduction apparently did not occur.

An ice layer building up within minutes would be problematic for imaging large surfaces with tiling, since a substantial loss of contrast would occur before the full

image is acquired. At this stage, the ice-layer build-up does not prevent further experiments with the current setup, since the acquisition of single-tile stacks is possible without noticeable contrast impairment (in both Quanta microscopes).

Another effect caused by the low operating temperature is the shrinking of the knife holder and the sample holder. When cooled down, the sample surface recedes by several tens of microns. When the stack is started at room temperature and the sample surface has been cut with the knife, it is therefore necessary to perform a second approach with the knife when the final temperature has been reached.

The knife position also changes, since the knife holder contracts during cooling. If the knife blade is positioned too close to the leading edge at room temperature, the knife will move over the sample surface during the cool-down process, preventing stack acquisition. It is therefore necessary to position the knife farther away from the leading edge to compensate for this effect.

The diamond knife itself also contracts, which might compromise stability if it had a thermal expansion coefficient larger than the one of the knife holder material. However, the expansion coefficient of diamond is only about 1.0×10^{-6}/K at room temperature and $<0.1 \times 10^{-6}$/K at 100 K (Stoupin & Shvyd'ko, 2011), much smaller than the expansion coefficient of titanium (8.6×10^{-6}/K at room temperature). Therefore, as the temperature is lowered, the knife holder will clamp the diamond knife more tightly.

4.3.3 Cutting and imaging at low temperature

At the beginning of a Cryo-SBEM experiment, the sample surface is carefully moved up towards the cutting plane using a screw for course positioning and the z-motor for the final approach. After the chamber has reached high vacuum, a few test cuts are performed at room temperature to verify that everything is set up correctly. The Cryotiger compressor is started and the cold-end temperature starts to drop until its final temperature of 73 kelvin is reached. Imaging with the SEM shows the sample covered by a layer of ice that has formed during the cool-down process (Fig. 4.5). About 130 cuts of 150 nm thickness are performed (while periodically observing the sample surface with the BSE detector) until the surface is reached and the ice layer is cut off by the knife. No chatter or any other cutting artifacts were observed when cutting fresh surfaces at cryogenic temperatures.

With the copper braid initially used to connect the cryo-sample-holder to the copper cold end (similar to the braid connecting the knife holder shown in Fig. 4.3a), substantial jitter could be seen in the images, most likely caused by vibrations of the copper cold end that were transmitted by the copper braid. This problem was solved by using a much more loosely woven copper braid that was bent in a U shape to minimize the force transmitted to the sample. However, in some cases jitter reappeared several hours after the final cold end temperature had been reached, likely due to ice bridges forming between the copper wires, reducing the compliance.

Initial cutting tests with only the sample being cooled resulted in very irregular cutting, since the knife was "hot" relative to the sample and induced thermal expansion during contact with the sample surface. When both sample and knife were cooled, as in the current setup, the temperature difference was reduced to about 12 K. By varying the thickness and the length of the braids, the final temperatures can be adjusted. By changing the sample holder's copper braid, the temperature difference was reduced to about 6 K. A further reduction appears essential, since consistent cutting could not be achieved yet with the current setup. Another reason why cutting problems persist could be that the forces holding the sample and the knife holder in place become too small as the temperature decreases and both sample and knife contract.

Sample surface charging appeared to become worse at cryogenic temperatures. Charging in cell bodies increased compared to room temperature conditions (Fig. 4.6), and uneven signal intensities were observed at cryogenic temperatures. However, these effects were not observed in all cases. To minimize charging problems, samples with high intrinsic conductivity were used for Cryo-SBEM experiments (see Appendix B). The sides of all samples were coated with gold to ensure a good connection to ground. Grounding of the cryo-sample-holder was provided via the Cryotiger cold end.

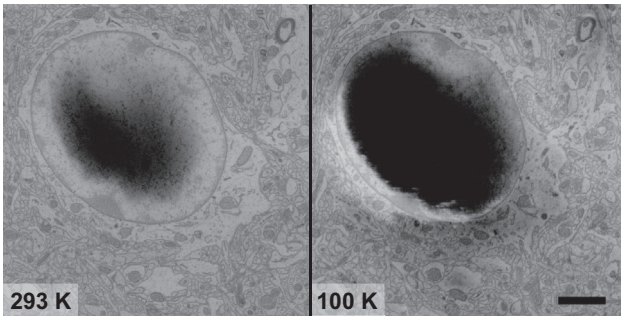

Fig. 4.6: Charging at room temperature (a) and after the sample had been cooled to 100 K (b). Both images acquired in high vacuum at 2 keV landing energy and 100 pA beam current, 8 µs dwell time. Scale bar: 1 µm.

4.4 Discussion and next steps

The most probable obstacle preventing stack acquisition at low temperatures with the current setup appears to be the remaining temperature difference between knife and sample. The foremost aim for the next experiments will therefore be to make this difference as small as possible (<1 K). This could be achieved in two ways: (1) Thickness and length of the copper braids could be adjusted in a series of experiments until the temperature gap is closed. (2) Controlled counter-heating of the sample and/or the knife could be used, for example with nichrome wire heaters. The disadvantage of this approach over using the copper braids is the added complexity and the risk of noise or stability issues.

If a small temperature difference remains, it seems reasonable that the knife should always be colder than the sample: A knife that is warmer than the sample will cause expansion, which pushes sample material against the knife, possibly prolonging expansion; a knife that is colder than the sample would cause contraction of the sample material, which should, in contrast, immediately reduce or prevent further contraction.

If consistent low-temperature cutting is achieved, the following experiment will be carried out. First, 25-nm stacks will be acquired at room temperature using a series of increasing electron doses until a dose is reached where consistent cutting is no longer possible. Using the same sample and the same imaging parameters, the SBEM will then be operated at low temperatures (110 K or lower) and again, stacks will be taken at increasing electron doses. If consistent cutting can be achieved at a higher dose than the maximum dose achievable at room temperature, the proof of principle would be successful. Electron dose thresholds could be established for different landing energies, cutting thicknesses, and types of embedding.

To reduce the amount of residual water in the chamber, there are various approaches that could be explored: better high vacuum flanges that reduce diffusion of water into the chamber, a turbo pump with a higher efficiency for water molecules, 'cryo-blades' (cold surfaces that act as anti-contaminators) around the sample surface, or bake-out solutions.

If sample surface charging turns out to be a general problem for low-temperature operation, charge elimination methods like the ones presented in this dissertation (in-chamber coating or charge neutralization with an ion gun) may need to be combined with Cryo-SBEM.

5 Conclusions and Outlook

Three new approaches to overcome limitations of SBEM imaging were presented in this dissertation:

(1) **Charge neutralization with an ion gun**,

(2) **Automated in-chamber specimen coating**,

two techniques to eliminate surface charging – with the aim to allow SBEM imaging of non-conducting specimens in high vacuum;

(3) **Cryo-SBEM** (low-temperature cutting and imaging),

to reduce the effects of electron beam damage – with the aim to enable thin cutting at electron doses higher than the maximum doses for cutting at room temperature.

Charge neutralization with an ion gun removes all visible charging artifacts for BSE imaging at low magnifications (<2000x, >66 nm pixel size, 150 pA beam current, on an FEI Quanta microscope). However, at higher magnifications (especially ≥8000x, ≤16.5 nm pixel size, typical for SBEM imaging on the FEI Quanta), only partial neutralization is achieved; charging in regions of high sample surface resistivity remains in most cases (cell bodies and blood vessels in case of the samples used for charge neutralization experiments). In the special case of badly-grounded or electrically floating samples, the ion gun provides a ground connection through the vacuum by supplying positive current, thus allowing stable BSE imaging (although charging artifacts remain). The gun's custom-developed ion optics achieve current densities of >300 nA/mm^2 for argon, >150 nA/mm^2 for helium, and >100 nA/mm^2 for nitrogen, which should be sufficient to provide complete charge neutralization at

higher magnifications (>7000, <19 nm pixel size). The broad energy spectrum of the ions and their ballistic trajectories may be the reasons why only partial neutralization is achieved. Noise from the ion gun is negligible for BSE imaging in most cases. SE imaging is disturbed by stray electrons from the ion gun. Attempts to suppress the stray electrons to test charge neutralization for SE imaging were not pursued, since complete charge elimination for BSE imaging is a prerequisite if charge elimination for SE imaging is to be successful.

Automated in-chamber specimen coating with an electron beam evaporator provides reliable surface charge elimination for both BSE and SE imaging in all tested cases, even for electron beam currents as high as 25 nA and surface areas as large as ~1 cm^2. Thin films of palladium (1–2 nm mass thickness) reduce SNR less than the widely-used low-vacuum method (for pressures ≥20 Pa). Coating also enables the use of beam deceleration for non-conducting samples, which substantially improves SNR. SBEM acquisition with automated coating was demonstrated for over 1000 cut/coat/image cycles; stacks using BSE contrast (with and without beam deceleration) and SE contrast were acquired in high vacuum. A new evaporator head was designed to protect the filament from bombardment with evaporated material, and to potentially achieve more efficient material use during coating.

Cryo-SBEM was implemented with a closed-loop cooling system and a custom-developed cryo-microtome. The current setup allows both sample and diamond knife to be cooled down to 100−110 K. Initial experiments have shown that cutting at 110 K causes no cutting artifacts on the sample surface. However, consistent cutting (uniform cutting thickness) at cryogenic temperatures has not been achieved yet, presumably because the temperature difference between the knife and the sample is still too large (>5 K). Another problem with the current setup is residual water in the vacuum chamber that freezes out on the cold sample surface. However, this effect can be neglected for single-tile stack acquisitions, and it appeared much reduced in a different vacuum system that was tested. Yet another problem could be increased surface charging at cryogenic temperatures, which may require charge elimination methods like the ones presented in this dissertation to be combined with Cryo-SBEM.

Among the three methods presented here, automated in-chamber specimen coating has shown the most favorable results so far, which were published in a proof-of-principle article (Titze & Denk, 2013). Future work on the automated coating method could focus on the following aspects: (1) Increasing the maximum number of coating

cycles (up to 10,000 cycles and beyond); (2) Optimizing the coating process to minimize the required time per cycle; (3) Combining the method with multi-beam S(B)EM; (4) Evaluating other coating materials to find the most suitable ones for BSE imaging and SE imaging, respectively; and (5) Extending the method to other types of non-conducting specimens, for which SBEM acquisition may be of interest.

For the new custom-developed evaporator head further testing will be required to establish whether it allows automated carbon evaporation over hundreds of coating cycles (which would be useful, e.g., for a potential combination of X-ray microanalysis with SBEM), and whether the amount of required rod material per coating can be reduced, which would be of interest for all applications using electron beam evaporation.

Automated in-chamber specimen coating appears to be a promising candidate to become a standard feature in electron microscopes, especially if further improvements as described above can be realized. The method is cost-effective: The full in-chamber coating setup can be realized for less than €10 000, a small fraction of the cost of a new electron microscope.

For the ion gun to achieve complete charge neutralization for BSE (and potentially SE) imaging at higher magnifications (≥8000x), the current ion gun setup would probably require further modifications. However, the current level of charge neutralization achieved with the ion gun may be suitable for (1) applications for which low magnifications are sufficient, (2) applications for which remaining charging at higher magnification is acceptable if otherwise useful images are obtained, or (3) in cases where other charge-neutralization methods cannot be used. Until now, charge neutralization with the ion gun has only been tested for epoxy-embedded neural tissue; it may be fruitful to extend experiments to other non-conducting specimens to examine whether partial or full neutralization can be achieved.

The Cryo-SBEM experiments have not yet shown whether a lower operating temperature will allow thin cutting at higher electron doses. The highest priority now is to make the temperature difference between sample and knife as small as possible, either by modifying the braids that connect sample and knife to the cold end or by using controlled counter-heating. The next step will be to acquire stacks at

different electron doses, and compare cryogenic-temperature and room-temperature cutting results.

All three techniques add complexity to the standard SBEM setup, which must be justified by performance improvements. Automated in-chamber coating offers three such improvements for SBEM imaging of non-conducting samples: (1) Less SNR reduction in comparison with the low-vacuum method for BSE imaging, (2) SE imaging in high vacuum, and (3) BSE imaging with beam deceleration. The ion gun method currently offers charge neutralization with restrictions and for BSE imaging only. A definitive evaluation of Cryo-SBEM is not possible yet.

The methods presented in this dissertation compete with chemical approaches to tackle charging and beam damage effects – samples with higher intrinsic conductivity may reduce charging to acceptable levels; more radiation-resistant embedding media may allow higher electron doses for thin cutting. While chemical solutions certainly beat the 'physical' methods presented here in terms of lower complexity and ease of use, the physical methods may triumph in terms of scope, since they should be applicable for a wide range of sample types and imaging parameters.

Appendix A: SNR estimation

Signal-to-noise ratio (SNR) is defined – in a physics or engineering context – as the ratio between signal power (P_S) and noise power (P_N), or as the square of the respective amplitude ratios:

$$\mathrm{SNR} = P_\mathrm{S}/P_\mathrm{N} = (A_\mathrm{S}/A_\mathrm{N})^2$$

In broader terms, it is defined as the ratio between meaningful information and unwanted information.

In the case of electron micrographs, SNR can be determined as follows. If a featureless specimen is imaged, the SNR can be calculated from the histogram of the image by dividing the offset-corrected mean intensity level by the standard deviation (Schatten & Pawley, 2007, Chapter 4). In the (usual) case of images that contain features (useful signal), two images of the same area can be acquired sequentially, which allows the SNR to be calculated using cross-correlation, provided that the images are perfectly aligned (Frank & Al-Ali, 1975). The same approach can also be used for alternate pairs of lines in a single image (Oho et al., 2000; Joy, 2002).

For this dissertation, I employed an alternative method using autocorrelation (Thong et al., 2001) to estimate the signal-to-noise ratios of single images, following the definition $\mathrm{SNR} = \mathrm{Var}\,(I_\mathrm{signal})\,/\mathrm{Var}\,(I_\mathrm{noise})$, where I_signal and I_noise are the image intensities of the signal and the noise, respectively (Fig. A.1). This approach appears suitable for S(B)EM images, since their information content is provided by material contrast, which corresponds to the variance of the histogram.

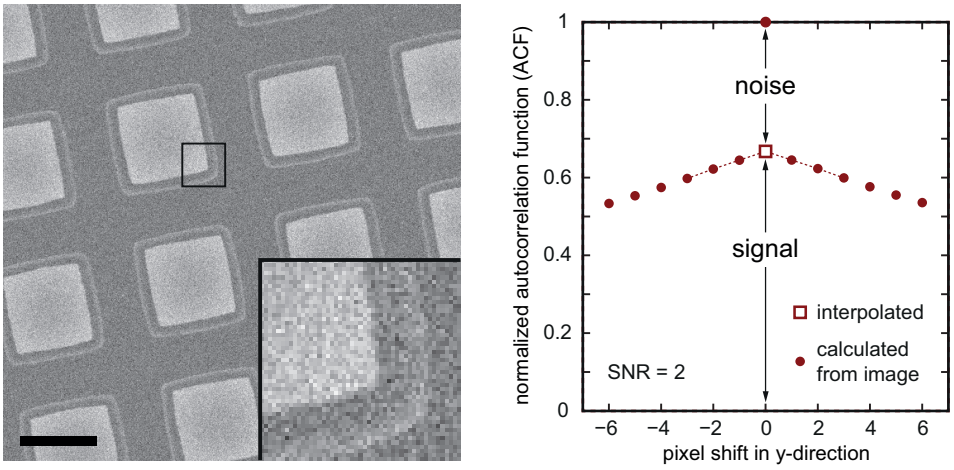

Fig. A.1: SNR estimation using autocorrelation (Thong et al., 2001). Left: Silicon square test sample (FEI Company, part number 4035 272 74851). Scale bar: 25 µm. Right: SNR of the image on the left is estimated by interpolating the noise-free peak of the autocorrelation function (= signal) and dividing it by the noise component at the origin of the ACF. This method is based on the assumption that only the signal is correlated over distances of several pixels, while the noise is uncorrelated from pixel to pixel.

I validated the Thong method by adding artificial noise to noise-free test images and compared actual and computed SNR. For SNRs between 0.1 and 10 the discrepancy was <4%. All SNR computations were performed with a custom-written MATLAB script using the function `normxcorr2()` to compute the normalized autocorrelation function and `spline()` to perform the interpolation (as in Fantana, 2006).

To ensure comparability of SNR for different imaging conditions of neural tissue samples, I used homogenous neuropil subregions to compute SNR. For the quantification of SNR under low-vacuum conditions, I used a silicon square grid sample with a highly regular pattern, for which the estimation of the noise-free signal component in the autocorrelation function could be performed easily (Fig. A.1).

Appendix B: Biological samples

All biological samples used for the projects presented in this dissertation were heavy-metal-stained neural tissue, embedded in epoxy resin. In the following, the preparation protocols are summarized.

Samples used for automated in-chamber specimen coating:

(1) *Rabbit retina*, provided by Kevin Briggman (several samples). Prior to embedding (Epon hard mixture; Hayat, 2000), the retina was placed in a horseradish peroxidase solution, chemically fixed, and subsequently stained with diaminobenzidine, osmium tetroxide, uranyl acetate (Terzakis, 1968), and lead aspartate (Walton, 1979). The samples were trimmed for diamond-knife SBEM (surface area <0.5 mm^2).

(2) *Zebra finch basal ganglia*, provided by Jörgen Kornfeld (one sample). Prior to embedding in Epon (mixture as above), the tissue was aldehyde-fixed under conditions that preserved the extracellular space (Cragg, 1980), and then stained using a rOTO (reduced osmium tetroxide, thiocarbohydrazide, osmium tetroxide) protocol (Seligman et al., 1966, Malick et al., 1975), followed by uranyl acetate and lead aspartate. The sample was trimmed for diamond-knife SBEM (surface area <0.5 mm^2).

(3) *Whole mouse brain*, provided by Shawn Mikula (one sample). The whole brain was stained with a myelin-enhancing osmium tetroxide-based protocol (Mikula et al., 2012) and embedded in Quetol (Kushida, 1974). The sample was trimmed down in the coronal plane to about one half of its length; its surface (8 mm × 12 mm) was smoothed with an ultramicrotome (Reichert Ultracut S, Leica AG, Austria) before each in-chamber coating.

Samples used for ion-gun charge neutralization experiments:

Retina samples, embedded in Epon, prepared with a protocol identical or very similar to the one described above. Three samples were provided by Kevin Briggman, one by Heinz Horstmann. All samples were trimmed for diamond-knife SBEM (surface area <0.5 mm^2).

Samples used for Cryo-SBEM experiments:

(1) *Retina*, provided by Kevin Briggman (protocol similar to protocol for zebra finch sample, described on the previous page).

(2) *Mouse brain*, provided by Sarah Mikula. The brain was aldehyde-fixed without extracellular space preservation and stained using a rOTO protocol, followed by uranyl acetate and lead aspartate, then embedded in Durcupan (Stäubli, 1963).

All samples were trimmed for diamond-knife SBEM (surface area <0.5 mm^2).

Appendix C: List of acronyms/abbreviations

ACL	autocorrelation function
ATUM	automated tape-collecting ultramicrotome
BSE	backscattered electrons
C	carbon
Cr	chromium
ET	Everhart-Thornley (a type of SE detector)
FIB	focused ion beam
FOV	field of view
FWHM	full width at half maximum
GND	ground
ICI	ion current integral
OFHC	oxygen-free high thermal conductivity
Pd	palladium
rOTO	reduced osmium tetroxide, thiocarbohydrazide, osmium tetroxide
RTD	resistance temperature detector
SBEM	serial block-face electron microscope/microscopy
SE	secondary electrons
SEM	scanning electron microscope/microscopy
SNR	signal-to-noise ratio
TEM	transmission electron microscope/microscopy

References

ANTON, R., WIEGNER, T., NAUMANN, W., LIEBMANN, M., KLEIN, C. & BRADLEY, C. (2000). Design and performance of a versatile, cost-effective microwave electron cyclotron resonance plasma source for surface and thin film processing. *Review of Scientific Instruments* **71**, 1177–1180.

ARDENNE, M. (1938). Das Elektronen-Rastermikroskop. Praktische Ausführung. *Z Tech Phys* **19**, 407–416.

ASMUSSEN, J. (1989). Electron cyclotron resonance microwave discharges for etching and thin-film deposition. *Journal of Vacuum Science & Technology A: Vacuum, Surfaces, and Films* **7**, 883.

AZEVEDO, F. A. C., CARVALHO, L. R. B., GRINBERG, L. T., FARFEL, J. M., FERRETTI, R. E. L., LEITE, R. E. P., FILHO, W. J., LENT, R. & HERCULANO-HOUZEL, S. (2009). Equal numbers of neuronal and nonneuronal cells make the human brain an isometrically scaled-up primate brain. *The Journal of Comparative Neurology* **513**, 532–541.

BLUE, M. D. & DANIELSON, G. C. (1957). Electrical Properties of Arc-Evaporated Carbon Films. *Journal of Applied Physics* **28**, 583.

BRIGGMAN, K. L. & BOCK, D. D. (2012). Volume electron microscopy for neuronal circuit reconstruction. *Current Opinion in Neurobiology* **22**, 154–161.

BRIGGMAN, K. L. & DENK, W. (2006). Towards neural circuit reconstruction with volume electron microscopy techniques. *Current Opinion in Neurobiology* **16**, 562–570.

BRIGGMAN, K. L., HELMSTAEDTER, M. & DENK, W. (2011). Wiring specificity in the direction-selectivity circuit of the retina. *Nature* **471**, 183–188.

BUSHBY, A. J., P'NG, K. M. Y., YOUNG, R. D., PINALI, C., KNUPP, C. & QUANTOCK, A. J. (2011). Imaging three-dimensional tissue architectures by focused ion beam scanning electron microscopy. *Nature protocols* **6**, 845–858.

CAZAUX, J. (1986). Some considerations on the electric field induced in insulators by electron bombardment. *Journal of Applied Physics* **59**, 1418.

CAZAUX, J. (2004). Charging in scanning electron microscopy 'from inside and outside'. *Scanning* **26**, 181–203.

CRAGG, B. (1980). Preservation of extracellular space during fixation of the brain for electron microscopy. *Tissue & cell* **12**, 63–72.

CRAWFORD, C. K. (1979). Charge neutralization using very low energy ions. *Scanning Electron Microscopy* **2**, 31–46.

CRAWFORD, C. K. (1980). Ion charge neutralization effects in scanning electron microscopes. *Scanning Electron Microscopy* **4**, 11–25.

DEERINCK, T., BUSHONG, E., LEV-RAM, V., SHU, X., TSIEN, R. & ELLISMAN, M. (2010). Enhancing Serial Block-Face Scanning Electron Microscopy to Enable High Resolution 3-D Nanohistology of Cells and Tissues. *Microscopy and Microanalysis* **16**, 1138–1139.

DENK, W., BRIGGMAN, K. L. & HELMSTAEDTER, M. (2012). Structural neurobiology: missing link to a mechanistic understanding of neural computation. *Nature Reviews Neuroscience*.

DENK, W. & HORSTMANN, H. (2004). Serial Block-Face Scanning Electron Microscopy to Reconstruct Three-Dimensional Tissue Nanostructure. *PLoS Biology* **2**, e329.

ECHLIN, P. (1975). Sputter coating techniques for SEM. *SEM/IITRI 7* 217–224.

ECHLIN, P. (2009). *Handbook of Sample Preparation for Scanning Electron Microscopy and X-Ray Microanalysis*. Springer Science+Business Media.

EGERTON, R. F., CROZIER, P. A. & RICE, P. (1987). Electron energy-loss spectroscopy and chemical change. *Ultramicroscopy* **23**, 305–312.

EGERTON, R. F., LI, P. & MALAC, M. (2004). Radiation damage in the TEM and SEM. *Micron* **35**, 399–409.

FANTANA, H. A. (2006). Entladung nichtleitender Objekte durch niederenergetische Ionen während der Abbildung im Rasterelektronenmikroskop. Diplomarbeit. Universität Heidelberg.

FRANK, J. & AL-ALI, L. (1975). Signal-to-noise ratio of electron micrographs obtained by cross correlation. *Nature* **256**, 376–379.

FRANK, L. & MÜLLEROVÁ, I. (1999). Strategies for low- and very-low-energy SEM. *J Electron Microsc (Tokyo)* **48**, 205–219.

FRANKS, F. (2000). *Water: a matrix of life*. 2nd ed. Cambridge, UK: Royal Society of Chemistry.

FUNSTEN, H. O., SUSZCYNSKY, D. M., RITZAU, S. M. & KORDE, R. (1997). Response of 100% internal quantum efficiency silicon photodiodes to 200 eV-40 keV electrons. *IEEE Transactions on Nuclear Science* **44**, 2561–2565.

GOLDSTEIN, J., NEWBURY, D., JOY, D., LYMAN, C., ECHLIN, P., LIFSHIN, E., SAWYER, L. & MICHAEL, J. (2003). *Scanning Electron Microscopy and X-ray Microanalysis*. 3rd ed. Kluwer Academic/Plenum Publishers, New York.

GRUBB, D. T. (1974). Review: Radiation damage and electron microscopy of organic polymers. *Journal of Materials Science* **9**, 1715–1736.

HAYAT, M. A. (ed.) (2000). *Principles and techniques of electron microscopy: biological applications*. 4th ed. Cambridge, UK ; New York: Cambridge University Press.

HAYWORTH, K., KASTHURI, N., SCHALEK, R. & LICHTMAN, J. (2006). Automating the Collection of Ultrathin Serial Sections for Large Volume TEM Reconstructions. *Microscopy and Microanalysis* **12**, 86.

HELMSTAEDTER, M., BRIGGMAN, K. L. & DENK, W. (2008). 3D structural imaging of the brain with photons and electrons. *Current Opinion in Neurobiology* **18**, 633–641.

HELMSTAEDTER, M., BRIGGMAN, K. L. & DENK, W. (2011). High-accuracy neurite reconstruction for high-throughput neuroanatomy. *Nature Neuroscience* **14**, 1081–1090.

HELMSTAEDTER, M. & MITRA, P. P. (2012). Computational methods and challenges for large-scale circuit mapping. *Current Opinion in Neurobiology* **22**, 162–169.

HEYMANN, J. A. W., HAYLES, M., GESTMANN, I., GIANNUZZI, L. A., LICH, B. & SUBRAMANIAM, S. (2006). Site-specific 3D imaging of cells and tissues with a dual beam microscope. *Journal of Structural Biology* **155**, 63–73.

JOY, D. C. (1989). Control of charging in low-voltage SEM. *Scanning* **11**, 1–4.

JOY, D. C. (2002). SMART - a program to measure SEM resolution and imaging performance. *Journal of Microscopy* **208**, 24–34.

JOY, D. C. & JOY, C. S. (1996). Low voltage scanning electron microscopy. *Micron* **27**, 247–263.

KANAYA, K. & OKAYAMA, S. (1972). Penetration and energy-loss theory of electrons in solid targets. *Journal of Physics D: Applied Physics* **5**, 43–58.

KNOLL, M. & RUSKA, E. (1932). Das Elektronenmikroskop. *Z. Physik* **78**, 318–339.

KNOTT, G., MARCHMAN, H., WALL, D. & LICH, B. (2008). Serial Section Scanning Electron Microscopy of Adult Brain Tissue Using Focused Ion Beam Milling. *Journal of Neuroscience* **28**, 2959–2964.

KUSHIDA, H. (1974). A New Method for Embedding with a Low Viscosity Epoxy Resin 'Quetol 651'. *Journal of Electron Microscopy* **23**, 197.

LAMVIK, M. K. (1991). Radiation damage in dry and frozen hydrated organic material. *Journal of Microscopy* **161**, 171–181.

LARSON, P. E. & KELLY, M. A. (1998). Surface charge neutralization of insulating samples in x-ray photoemission spectroscopy. *Journal of Vacuum Science & Technology A: Vacuum, Surfaces, and Films* **16**, 3483.

LEIGHTON, S. B. (1981). SEM images of block faces, cut by a miniature microtome within the SEM – a technical note. *Scanning Electron Microscopy* **2**, 73–76.

LICHTMAN, J. W. & DENK, W. (2011). The Big and the Small: Challenges of Imaging the Brain's Circuits. *Science* **334**, 618–623.

LIDE, D. R. (2005). *CRC Handbook of Chemistry and Physics 86th ed. 2005-2006*. Boca Raton, FL.; London: CRC.

LIN, Y. & JOY, D. C. (2005). A new examination of secondary electron yield data. *Surface and Interface Analysis* **37**, 895–900.

MALICK, L. E., WILSON, R. B. & STETSON, D. (1975). Modified thiocarbohydrazide procedure for scanning electron microscopy: routine use for normal, pathological, or experimental tissues. *Stain technology* **50**, 265–269.

MANCUSO, J. (2012). Cutting thin while maintaing large volumes at high resolution using serial block face imaging in the SEM. 15th European Microscopy Congress. Manchester, UK.

MATHIEU, C. (1999). The beam-gas and signal-gas interactions in the variable pressure scanning electron microscope. *Scanning Microscopy* **13**, 23–41.

MIKULA, S., BINDING, J. & DENK, W. (2012). Staining and embedding the whole mouse brain for electron microscopy. *Nature Methods*.

MONCRIEFF, D. ., ROBINSON, V. N. E. & HARRIS, L. B. (1978). Charge neutralisation of insulating surfaces in the SEM by gas ionisation. *J Phys D Appl Phys* **11**, 2315–2325.

MONCRIEFF, D. A., BARKER, P. R. & ROBINSON, V. N. E. (1979). Electron scattering by gas in the scanning electron microscope. *Journal of Physics D: Applied Physics* **12**, 481–488.

MORGAN, M. (1971). Electrical conduction in amorphous carbon films. *Thin Solid Films* **7**, 313–323.

OHO, E., ASAI, N. & ITOH, S. (2000). Image quality improvement using helium gas in low voltage variable pressure scanning electron microscopy. *Journal of electron microscopy* **49**, 761–763.

OHTA, K., SADAYAMA, S., TOGO, A., HIGASHI, R., TANOUE, R. & NAKAMURA, K. (2012). Beam deceleration for block-face scanning electron microscopy of embedded biological tissue. *Micron* **43**, 612–620.

PADEN, R. S. & NIXON, W. C. (1968). Retarding field scanning electron microscopy. *Journal of Physics E: Scientific Instruments* **1**, 1073–1080.

PAWLEY, J. B. (1972). Charging artifacts in the scanning electron microscope. *Scanning Electron Microscopy* **1**, 153–160.

PHIFER, D., TUMA, L., VYSTAVEL, T., WANDROL, P. & YOUNG, R. J. (2009). Improving SEM Imaging Performance Using Beam Deceleration. *Microscopy Today* **17**, 40.

RAMÓN Y CAJAL, S. (1989). *Recollections of my life*. 1st MIT Press pbk. ed. Cambridge, Mass: MIT Press.

READ, F. & BOWRING, N. (2004). Simulation of thermionic cathodes. *Nuclear Instruments and Methods in Physics Research Section A: Accelerators, Spectrometers, Detectors and Associated Equipment* **531**, 407–415.

READ, F. H. & BOWRING, N. J. (2011). The CPO programs and the BEM for charged particle optics. *Nuclear Instruments and Methods in Physics Research Section A: Accelerators, Spectrometers, Detectors and Associated Equipment* **645**, 273–277.

REIMER, L. (1998). *Scanning Electron Microscopy: Physics of Image Formation and Microanalysis*. 2nd edition. Springer.

ROBINSON, V. N. E. (1975). The elimination of charging artefacts in the scanning electron microscope. *Journal of Physics E: Scientific Instruments* **8**, 638–640.

SCHALEK, R., WILSON, A., LICHTMAN, J., JOSH, M., KASTHURI, N., BERGER, D., SEUNG, S., ANGER, P., HAYWORTH, K. & ADERHOLD, D. (2012). ATUM-based SEM for High-Speed Large-Volume Biological Reconstructions. *Microscopy and Microanalysis* **18**, 572–573.

SCHATTEN, H. & PAWLEY, J. B. (2007). *Biological low voltage field emission scanning electron microscopy*. New York; London: Springer.

SELIGMAN, A. M., WASSERKRUG, H. L. & HANKER, J. S. (1966). A new staining method (OTO) for enhancing contrast of lipid-containing membranes and droplets in osmium tetroxide-fixed tissue with osmiophilic thiocarbohydrazide (TCH). *J Cell Biol* **30**, 424–432.

SHAFFNER, T. J. & VAN VELD, R. D. (1971). 'Charging' effects in the scanning electron microscope. *Journal of Physics E: Scientific Instruments* **4**, 633–637.

STÄUBLI, W. (1963). A new embedding technique for electron microscopy, combining a water-soluble epoxy resin (Durcupan) with water-insoluble Araldite. *The Journal of Cell Biology* **16**, 197–201.

STÖCKER, H. (2000). *Taschenbuch der Physik*. 4th ed. Verlag Harri Deutsch.

STOUPIN, S. & SHVYD'KO, Y. V. (2011). Ultraprecise studies of the thermal expansion coefficient of diamond using backscattering x-ray diffraction. *Physical Review B* **83**.

STUDER & GNAEGI (2000). Minimal compression of ultrathin sections with use of an oscillating diamond knife. *Journal of Microscopy* **197**, 94–100.

SUZUKI, E. (2002). High-resolution scanning electron microscopy of immunogold-labelled cells by the use of thin plasma coating of osmium. *Journal of Microscopy* **208**, 153–157.

TERZAKIS, J. A. (1968). Uranyl acetate, a stain and a fixative. *Journal of Ultrastructure Research* **22**, 168–184.

THIEL, B. L. & TOTH, M. (2005). Secondary electron contrast in low-vacuum/environmental scanning electron microscopy of dielectrics. *Journal of Applied Physics* **97**, 051101.

THONG, J. T. L., SIM, K. S. & PHANG, J. C. H. (2001). Single-Image Signal-to-Noise Ratio Estimation. *Scanning* **23**, 328–336.

TITZE, B. (2008). A long-life low-noise microwave-driven ion gun for SEM charge neutralization. Diploma thesis. University of Heidelberg.

TITZE, B. & DENK, W. (2013). Automated in-chamber specimen coating for serial block-face electron microscopy. *Journal of Microscopy* **250**, 101–110.

UNGAR, G. (1981). Radiation effects in polyethylene and n-alkanes. *Journal of Materials Science* **16**, 2635–2656.

WALLEY, P. A., WINEBERG, M. & BURDEN, M. S. J. (1971). The use of an electron beam evaporation source for electron microscope sample preparation. *Journal of Physics E: Scientific Instruments* **4**, 501–504.

WALTON, J. (1979). Lead aspartate, an en bloc contrast stain particularly useful for ultrastructural enzymology. *The journal of histochemistry and cytochemistry: official journal of the Histochemistry Society* **27**, 1337–1342.

WHITE, J. G., SOUTHGATE, E., THOMSON, J. N. & BRENNER, S. (1986). The structure of the nervous system of the nematode Caenorhabditis elegans. *Philos Trans R Soc Lond A* **314**, 1–340.

ZHU, Y., WANG, L., YAO, W. & CAO, L. (2001). The interface diffusion and reaction between Cr layer and diamond particle during metallization. *Applied Surface Science* **171**, 143–150.

Acknowledgments

Winfried Denk – thank you for your excellent support, insight and advice during the past years, and your encouragement at times when my level of optimism needed replenishment.

I am grateful to Rasmus Schröder for agreeing to act as second referee, and to Ulrich Schwarz and Ulrich Uwer for agreeing to act as referees for the disputation. I would also like to thank Johann Bollmann and Jochen Reinstein for helpful discussions and advice during my TAC meetings.

Jürgen Tritthardt and the whole team of the electronics workshop have built several components for the ion gun setup and the automated in-chamber coating setup. Thank you for your support with regard to everything electronics-related.

Martin Lukat, Niklas Neef and the whole team of the mechanical workshop – thank you for building various tools and parts, making modifications and repairs, and building the new evaporator head.

I am grateful to Andreas Gati and Thomas Niedermayer from Tectra GmbH for their technical support and advice (IonEtch and e^--flux).

Kevin Briggman, Jörgen Kornfeld, Shawn Mikula, and Sarah Mikula – for providing tissue samples.

Helmut Gnägi (Diatome) – for helpful discussions about diamond knives and cutting issues, and for performing cutting tests with palladium and chromium.

Georg Böck (TU Berlin) – for supplying initial test equipment, and helpful advice concerning the microwave-generation setup.

Michael Müller – for assistance with the SBEM remote-control software.

Christa Hörner-Ehm and Regina Zappe – who have provided great support with various administrative issues.

Sarah Mikula – for a critical reading of the manuscript.

I thank all members of the BMO for a fantastic work environment, especially Jonas Binding, Jörgen Kornfeld, Fabian Svara, Sarah & Shawn Mikula, Chintan Trivedi, Stephanie Preuß, and Kevin Börgens. Thank you for a great time in and outside the lab and many enjoyable Mensa breaks.

I am grateful to the Max Planck Society for funding.

A special 'thank you!' goes to Anikó – for your love, your support, and for lighting up gloomy days, and to my parents, who supported me from the distance.